TECHNISCHE
UNIVERSITÄT
DRESDEN

Leibniz-Institut
für Festkörper- und
Werkstoffforschung
Dresden

Superconductivity and topology in trigonal-$PtBi_2$

Dissertation

zur Erlangung des akademischen Grades
Doctor rerum naturalium
(Dr. rer. nat.)

vorgelegt
der Fakultät Mathematik und Naturwissenschaften
der Technischen Universität Dresden

von

Arthur Veyrat

geboren am 08 Mai 1996 in Toulouse, Frankreich

Die Dissertation wurde in der Zeit
von Oktober 2018 bis Februar 2022
am Leibniz Institut für Festkörper und Werkstoffforschung Dresden angefertigt.

Eingereicht am 10. März 2022
Verteidigt am 09. Mai 2022

1. Gutachter: Prof. Dr. Bernd Büchner

2. Gutachter: Dr. Hélène Bouchiat

Abstract

In recent years, Weyl semi-metals have attracted a lot of interest in topological condensed matter, for instance for their significant potential application in quantum electronics, as the coupling between Weyl semi-metals and superconductivity, either intrinsically in the material or at the interface of a heterostructure, gives rise to a new type of topological superconductivity, which could be used to perform quantum computation operations free from decoherence.

In this thesis, we investigate the low temperature magneto-transport properties of trigonal-$PtBi_2$, a layered material, both in the presence of quantum confinement (exfoliated nano-structures) and in its absence (macro-structures). We report band structure calculations showing that trigonal-$PtBi_2$ is a type-I Weyl semi-metal with multiple bands at the Fermi level. Shubnikov-de-Haas oscillations in macro-structures confirm the contribution to transport of carriers from multiple pockets, and magneto-transport measurements show an unusual angular dependence of the magnetoresistance with the field, which might be a manifestation of the large anisotropy of the topological band. We also report the existence of a large planar Hall effect in nano-structures, which is one of the predicted manifestations of Weyl physics.

At very low temperature, below 1K, trigonal-$PtBi_2$ becomes superconducting. We investigate the superconducting state in both macro- and nano-structures, and find that quantum confinement in nano-structures makes the superconductivity become two-dimensional. This result is confirmed by the characterization of a Berezinskii–Kosterlitz–Thouless (BKT) transition in nano-structures. This transition is very robust, as it occurs in nano-structures five times thicker than what had previously been reported for any BKT transitions in the literature. We also report on the impact of inhomogeneities on the superconducting transition.

Contents

Abstract **3**

Introduction **9**

1 Topological semi-metals and superconductivity **13**

1.1 Topological materials 14

1.1.1 Quantum Hall effect and topological insulators 14

1.1.2 Topological semi-metals 17

1.1.3 Signatures of Weyl topology in transport measurements . . . 19

1.2 Planar Hall effect in Weyl semi-metals 21

1.3 Superconductivity 22

1.3.1 Hallmarks of superconductivity 23

1.3.2 Bardeen–Cooper–Schrieffer theory 24

1.3.3 Ginzburg-Landau theory 24

1.3.4 Superconductivity at reduced dimensions 25

1.3.5 Topological superconductivity and low dimensionality 30

2 Methods **33**

2.1 Low temperature and low noise measurements 34

2.1.1 ^{3}He - ^{4}He dilution refrigerator 34

2.1.2 Low noise electrical measurements technique 36

2.2 Sample fabrication . . . 37
2.2.1 Macro-structure fabrication . . . 38
2.2.2 Mechanical exfoliation . . . 38
2.2.3 Samples studied . . . 44

3 Transport and planar Hall effect in trigonal-PtBi$_2$ 45
3.1 Crystalline configurations . . . 45
3.1.1 Pyrite configuration . . . 45
3.1.2 Trigonal configuration . . . 46
3.2 Band Structure Calculations . . . 46
3.3 Magnetotransport characterization . . . 48
3.3.1 Macro-structures . . . 48
3.3.2 Exfoliated structures . . . 57
3.4 Planar Hall Effect in exfoliated structures . . . 58
3.4.1 In-plane field mappings . . . 58
3.4.2 Data fitting . . . 59
3.4.3 Results . . . 63
3.4.4 Other samples . . . 66
3.4.5 Discussion . . . 67

4 Superconductivity in trigonal-PtBi$_2$ 69
4.1 Critical parameters . . . 69
4.2 Superconductivity in Macro-structures . . . 70
4.2.1 3D superconductivity . . . 71
4.3 Superconductivity in exfoliated structures . . . 74
4.3.1 Characterization of the superconductivity . . . 75
4.3.2 Dimensionality of the superconductivity . . . 79
4.3.3 Berezinskii–Kosterlitz–Thouless transition . . . 84
4.3.4 Inhomogeneous superconducting transitions . . . 89
4.4 Summary and conclusion . . . 99

Conclusion 101

Appendices 104

A Topology and Band structure 105
A.1 Quantum spin Hall effect 105
A.2 Band Structure calculation 107

B Magnetotransport 109
B.1 Magnetoresistance 109
B.2 Schubnikhov-de-Haas Oscillations 110
B.3 Temperature dependence of Shubnikov–de Haas oscillations 111
B.4 Planar Hall effect in S3 113

C Superconductivity 115
C.1 Macro-structures 115
C.1.1 Critical magnetic field 115
C.1.2 Point-Contact Measurements 117
C.2 Nano-structures 119
C.2.1 Dimensionality of the superconductivity 119
C.2.2 Berezinskii–Kosterlitz–Thouless transition 122
C.2.3 Inhomogeneous superconducting transitions 124

Acknowledgments 127

Introduction

The properties of a material can be significantly modified by quantum confinement, which is achieved when one or more of its dimensions are reduced below some relevant length scale. Such low-dimensional systems have attracted great interest in material physics in the past decades for their new and often unique properties, such as the the quantum Hall effect (QHE), a topological phase of matter which cannot be described by the usual theory of electronic band structure, and which was discovered experimentally in two dimensional electron gases (2DEGs) in 1980 [Klitzing et al., 1980]. This field found a new beginning with the discovery of the mechanical exfoliation of graphene [Novoselov et al., 2005], which made possible the study of newly emerging layered materials, and has since developed rapidly. Contrarily to the bulk graphite from which it can be easily exfoliated, graphene is a gapless semiconductor with Dirac-like linear dispersion and massless Fermion quasiparticles around the band touching points, which opened the possibility to study in mesoscopic physics effects which were until then only observable in high energy physics. Graphene also displays many other interesting properties, including an exceptional mechanical strength and a very large thermal conductivity.

In 2005, Kane and Mele predicted the existence of a new topological phase in graphene, provided that a very strong spin-orbit coupling could be induced in the material: the quantum spin Hall effect (QSHE) [Kane and Mele, 2005]. Experimentally, the spin-orbit coupling is expected to be very small in graphene and the QSHE has not been observed in graphene flakes. Nevertheless, the findings of Kane and Mele were extended to the case of HgTe quantum wells [Bernevig et al., 2006], were the QSHE was discovered soon afterwards [Konig et al., 2007]. Subsequent theoretical developments in band structure theory were made by taking into account the effects of the Berry phase and the symmetries of the Hamiltonian on the band structure. In essence, this new topological theory of band structure shows than not all band gaps are equivalent and that they can be sorted into different universal classes based on the symmetries of the Hamiltonian. The most important consequence of this theory is the existence of gapless states at the interface between materials of different universal classes. Since vacuum belongs to the trivial universality class, non-trivial materials therefore support conducting states on their surface (at 3D), edges (at 2D) or extremities (at 1D).

In 2011, a non-trivial 3D topological phase called Weyl semi-metal with a conducting bulk was predicted [Wan et al., 2011; Matsuura et al., 2013]. Most Weyl semimetals are layered materials with strong spin-orbit coupling, including trigonal-$\mathrm{PtBi_2}$ (tr-$\mathrm{PtBi_2}$), as we unveil in this work (see below). In these materials, the bulk bands touch at points called Weyl nodes, which have a defined chirality. These chiral nodes appear in pairs of opposite chirality, and the bands disperse linearly around them, forming topologically protected Weyl cones. One of the most important aspect of this topological band structure is that Weyl nodes act as sources or sinks of Berry curvature, depending on their chirality, which can have a significant impact on experimental properties of the material, including in transport, such as the appearance of a planar Hall effect.

In recent years, the interplay between topology and superconductivity has attracted considerable attention. A distinct kind of superconductivity can emerge in topological materials [Qi and Zhang, 2011], as well as at the interface between a conventional superconductor and a strong topological insulator [Liu et al., 2020]. Such topological superconductors may have unconventional pairing mechanisms, such as Fulde-Ferrell-Larkin-Ovchinnikov phases [Larkin and Ovchinnikov, 1964; Fulde and Ferrell, 1964] where the Cooper pairs have a finite momentum, which results in a non-uniform order parameter with a modulation along the momentum direction. Topological superconductors (TSCs) are also a good medium to study non-Abelian statistics, where quasiparticles are neither fermions nor bosons [Sato and Ando, 2017]. The edge states in TSCs are predicted to host Majorana fermions, which are their own antiparticle, and should allow for topologically-protected operations, free from decoherence, in quantum computation.

Besides the interplay between superconductivity and a possible non-trivial topology, 2D materials are a very interesting platform to study low dimensional superconductivity in general. When superconductivity occurs at two-dimensions, vortices and antivortices are generated by thermal fluctuations, even in the absence of magnetic field. At low temperature, the Berezinskii–Kosterlitz–Thouless (BKT) phase transition occurs and vortices and antivortices couple to one another in pairs, which are spatially pinned. Since vortex centers should host Majorana bound states in topological 2D superconductors [Frolov et al., 2020; Wang et al., 2018], these systems are very interesting to study Majorana modes at zero magnetic field.

The aim of our work is to study tr-$PtBi_2$, a layered van der Waals material with strong spin orbit coupling, through charge transport measurements. Density functional theory (DFT) calculations have shown that tr-$PtBi_2$ has a Weyl semi-metallic band structure, and the material has been shown to become superconducting at low temperature. One possible signature of the Weyl nature of tr-$PtBi_2$ is the appearance of a planar Hall effect in nano-structures, which cannot be attributed to any intrinsic magnetization of the material. The superconductivity becomes two-dimensional in thin nano-structures of tr-$PtBi_2$, with a unusually robust BKT phase transition happening in structures as thick as 60nm, making tr-$PtBi_2$ very interesting to study the robustness of the BKT transition. The combination of topology and robust 2D superconductivity in this material also makes it a promising candidate for studying intrinsic topological superconductivity and Majorana bound states. Thanks to its 2D layered nature, it is also possible to create tr-$PtBi_2$ heterostructures, which opens new possibilities to design complex devices. Such devices could include top and bottom electrostatic gates, to modify the Fermi energy in thin enough samples and study e.g. Josephson junctions, or interfaces between tr-$PtBi_2$ and other materials such as 2D ferromagnets.

This manuscript reports the main findings of our study, and is separated in two parts. The first part comprises the first two chapters and pertains to theoretical and methodological considerations, while the experimental results are presented and discussed in chapters 3 and 4. In the first chapter, we introduce the reader to the physics of topological systems, and especially of topological Weyl semi-metals. We then present the most important feature of superconductivity, before focusing on low dimensional superconductivity which appears in the presence of quantum confinement. In the second chapter, we present important concepts about very low temperature and low noise measurements, and describe the methods used to produce the samples which were studied. In the third chapter, the results of DFT calculation of the band structure are presented, along with a characterization of transport of macroscopic single crystals of tr-$PtBi_2$ in the normal state, followed by a preliminary study of the planar Hall effect in exfoliated nano-structures. In the fourth and final chapter, we studied superconductivity in both macro-structures and nano-structures, where we observed a reduction of the dimensionality of the superconductivity evidenced by a Berezinskii-Kosterlitz-Thouless transition happening at low temperature.

1 | Topological semi-metals and superconductivity

Historically, the study and understanding of phenomena in condensed matter physics has come hand in hand with the classification of the materials in which they appear. The discovery of materials eluding previously established classification is often associated with fundamental or technological breakthroughs. For instance, the electrical conducting properties of materials have been understood through the theory of electronic band structure, which makes it possible to classify materials as either conducting or insulating depending on the position of their Fermi level (respectively in the conduction band or in the band gap). The discovery (and understanding) of materials eluding this simple classification, semiconductors (which have smaller band gaps and can be tuned, e.g. via electrostatic gating, from insulators to conductors), led to the development of transistors in 1947, on which modern electronics is based.

In modern condensed matter physics, the classification is made in terms of phases of matter. These phases have been understood for decades following Lev Landau's approach, which characterizes them in terms of their spontaneously broken underlying symmetries. However, the discovery of the quantum Hall effect (QHE) [Klitzing et al., 1980] has led to the development of a new topological classification based on topological invariant (the Chern number in the case of the QHE) [Kosterlitz and Thouless, 1973; Thouless et al., 1982], in which some properties are protected from small changes of the material parameters. More than two decades later, the discovery of 2D topological insulators (2DTI) [Bernevig et al., 2006; Konig et al., 2007] resulted in the emergence of topological materials as a very active new field of research in condensed matter physics, with potential application in electronics. The discovery of 2DTI was quickly followed by that of many other topological phases, such as 3D topological insulators, as well as Dirac and Weyl semi-metals. In recent years, the combination of topological properties with superconductivity has also attracted growing interest, with the possibility of studying new superconducting pairing mechanisms (unconventional superconductivity), and applications in quantum electronics (topological superconductivity, e.g. Majorana zero modes) [Frolov et al., 2020; Qi and Zhang, 2011].

In this chapter, we will briefly introduce concepts of topology which are useful to understand the context of this study. We will then describe topological semi-metals, the class of topological materials to which trigonal-$PtBi_2$ (tr-$PtBi_2$) belongs, and will discuss some expected experimental signatures of this topology, including the planar Hall effect. In the second section of this chapter, we will introduce the basic concepts of superconductivity, and present the concepts behind the Bardeen–Cooper–Schrieffer (BCS) microscopic theory as well as the phenomenological Ginzburg-Landau (GL) theory. In the latter formalism, we will study the consequences of spatial confinement on the superconductivity (i.e. at lower dimension). We will also discuss briefly the interplay between superconductivity and topology, and some phenomena which may be observed in such a context.

1.1 Topological materials

The most basic electronic state of matter we can consider is the trivial insulating state of a trivial insulator. In the description of band theory, an insulator presents an energy gap separating a fully occupied valence band and a fully empty conduction band with the Fermi energy lying in the gap (see Fig.1.1.b). Such a state can be easily transformed continuously into a semiconducting state by tuning the Hamiltonian of the system, without phase transition: these two states are therefore topologically equivalent. In a similar way, it is possible to show that all trivial insulators (with different number of core bands) as well as the vacuum state (which also possesses an energy gap between an electron (conduction) band and a positron (valence) band, according to Dirac's relativistic quantum theory [Hasan and Kane, 2010]) are equivalent to the same topological phase. However, not all systems with an energy gap in their band structure are topologically equivalent to vacuum, as we will see in the following section.

1.1.1 Quantum Hall effect and topological insulators

The simplest example of a non-topologically trivial insulator, and the first one historically, is the integer quantum Hall effect (QHE) discovered experimentally by K. von Klitzing in 1980 [Klitzing et al., 1980], for which he received the 1985 Nobel Prize in Physics. This effect occurs in a gas of electrons confined to two dimensions

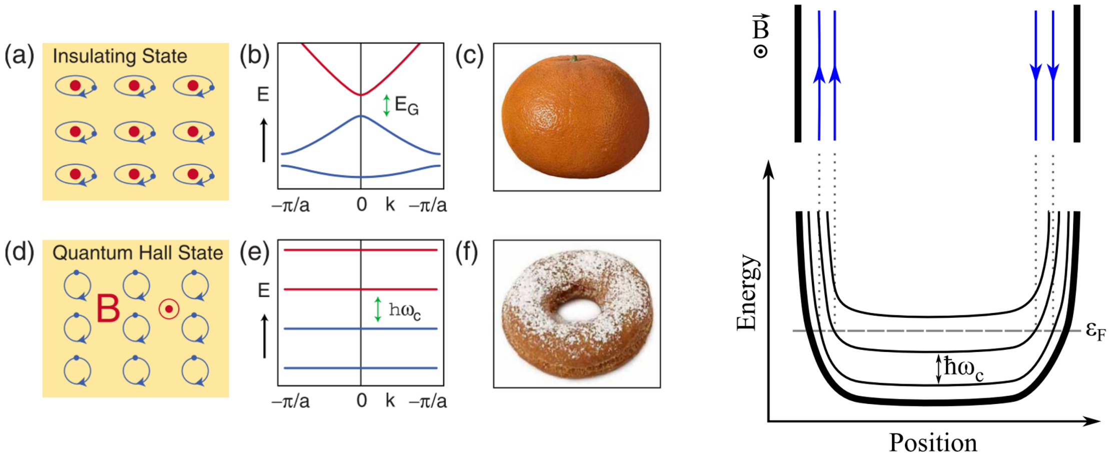

Figure 1.1: Left (a)-(f): Electron motion (a,d) and band structure (b,e) in a trivial insulator and a quantum Hall insulator (respectively top and bottom row). (c,f): representation of two topologically different objects, with genus 0 (c) and 1 (f). Adapted from [Hasan and Kane, 2010]. Right: Bending on the LLs at the edges of a sample, leading to the existence of conducting, chiral edge states. Adapted from [Zimmermann, 2017].

(2D electron gas, or 2DEG), in the presence of a high magnetic field B. In such a system, electrons have a cyclotron motion with frequency $\omega_c = \dfrac{eB}{m^*}$ (with e the electron energy and m^* the effective mass of the electrons), and quantized field-dependent energy levels (Landau Levels, or LLs) with energy $\varepsilon_n = \hbar\omega_c(n + 1/2)$, with $n \in \mathbb{N}$ (see Fig.1.1.e). At temperature T=0, if the Fermi energy lies between the LL N and the LL N+1, an energy gap exists between empty and occupied states, and the system is therefor a bulk insulator. In a finite sample, the LLs are bent upward close to the physical edges by the confinement potential linked to these edges (see Fig.1.1, right). This results in the Fermi level ε_F crossing each filled LL, closing the gap near the edge of the sample and creating one-dimensional chiral edge channels (N in total, one per filled LL), with no back-scattering allowed, leading to a vanishing longitudinal resistance (when ε_F is between two LL) [Klitzing et al., 1980].

The quantized Hall conductivity and the number of edge channels are topologically-protected properties in the system, i.e. they are not affected by smooth transformations of the Hamiltonian, as long as these do not close the energy gap. The topological invariant in this system is called the Chern number, and is equal to the number N of filled LLs [Hasan and Kane, 2010]. A geometrical equivalent to the

Chern number can be found in the genus of a surface (in simple terms, the number of "holes"), as it is impossible to smoothly transform an object into another with a different genus, for instance a sphere with g=0 (Fig.1.1.c) into a torus with g=1 (Fig.1.1.f).

In 2005, a new topological phase, the quantum spin Hall effect (QSHE), was predicted to appear in graphene, provided a strong enough spin-orbit coupling is induced in the graphene sheet [Kane and Mele, 2005]. Contrarily to the QHE, this topological phase does not break time reversal symmetry and has therefore a Chern number equal to zero. It can be seen as the superimposition of two time reversal symmetric QHE states with counter propagating spin-polarized edge channels (see Fig.A.1). This effect was predicted to appear in HgTe quantum wells the next year by Bernevig et al. [2006] and was experimentally confirmed one year later by Konig et al. [2007], establishing the first experimental realization of a 2-dimensional topological insulator.

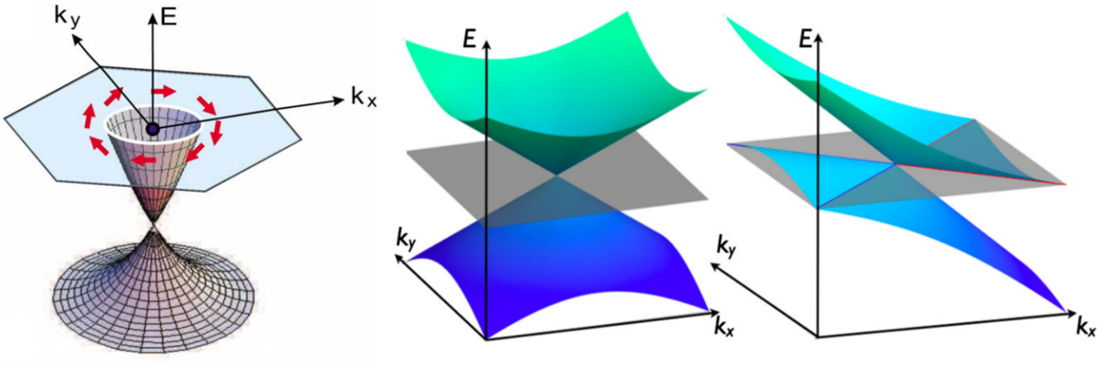

(a)

(b)

Figure 1.2: (a) Dirac cone with spin momentum locking corresponding to a topological surface state. Adapted from [Hasan and Kane, 2010]. (b) Schematic representations of a Weyl cone in a type-I (left) and type-II (right) Weyl semi-metal. Adapted from Armitage et al. [2018].

The important property of topological band theory, which the QHE and the QSHE evidence, is the existence of conducting, gapless states at the interface between topological systems of different topological class, e.g. between a topologically non-trivial phase and trivial vacuum. This is called the bulk-boundary correspondence: the difference in the topological class of two materials ensures the presence of topologically protected "boundary" states at the interface between the two materials.

Following the discovery of the QSHE in 2006, Fu et al. [2007] predicted the existence of topological insulators at 3 dimensions (3DTI). The most usual mechanism inducing a 3DTI state is band inversion, in which strong spin-orbit coupling in the material leads to an inversion of the valence and conduction bands. Hence, the bands must reverse at the interface and the gap has to vanish, creating conducting surface states at the Fermi level in the gap of the bulk bands. In the presence of time reversal symmetry these topological surface states (TSS) show a linear dispersion in every momentum direction, and can be described in real materials (i.e. with disorder) by a Dirac cone with spin-momentum locking (see Fig.1.2a) and a disorder potential. The Dirac Hamiltonian can thus be written as

$$\mathcal{H} = v\mathbf{p} \cdot \sigma + V(\mathbf{r}), \tag{1.1}$$

with v the Fermi velocity, $\mathbf{p}$ the momentum, $\sigma = (\sigma_x, \sigma_y)$ the Pauli matrices and $V(\mathbf{r})$ a potential representing the disorder [Murakami, 2007; Dufouleur et al., 2018].

1.1.2 Topological semi-metals

In the past decade, an important evolution has been the prediction and discovery of new topological phases in semi-metals [Wan et al., 2011; Matsuura et al., 2013]. These topological semi-metals can be separated in two main categories, Weyl and Dirac semi-metals, based on their symmetries. In the years following the 1928 publication of the Dirac equation [Dirac, 1928], which successfully reconciled for the first time quantum mechanics and relativity, several extensions of the theory were

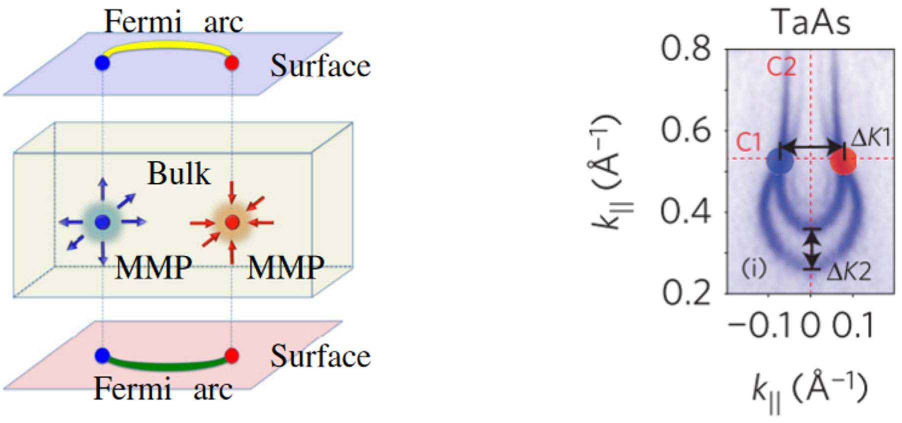

(a) (b)

Figure 1.3: (a) Representation of Fermi arcs connecting the surface projections of Weyl nodes of opposit chirality. Adapted from Lv et al. [2015]. (b) Fermi arcs in TaAs, imaged by ARPES. Adapted from Liu et al. [2016].

introduced, describing different systems. The most well known of these modifications was made by E. Majorana [Majorana and Maiani, 1937] using real numbers, and describes a neutral particle which is its own anti-particle. Prior to Majorana's prediction, H. Weyl made another modification of Dirac's equation for massless particles, the Weyl equations, which solutions are 2 particles with opposite chiralities, or handedness. Such a chiral particle, or Weyl fermion, can be combined with another Weyl fermion of the opposite chirality to form a Dirac fermion. Although Majorana's theory has found large echoes in modern particle physics, no fundamental particle has been identified as a Weyl fermion. In condensed matter systems however, the lowering of the symmetry in crystal lattices (with respect to free space) makes the study of Dirac and Weyl Fermions possible, at experimentally accessible energy scales, and quasiparticles which can be described by the Dirac and Weyl equations have been predicted in newly discovered semi-metallic topological phases [Matsuura et al., 2013; Armitage et al., 2018].

In these new topological phases, called Dirac and Weyl semi-metals, the conduction and valence bands touch at discreet points in the band structure called Dirac of Weyl nodes, with a linear energy dispersion close to these points in all three momenta directions, called Dirac and Weyl cones. Dirac nodes are fourfold degenerate and are not associated with any chirality, while Weyl nodes are twofold degenerate with either a positive or a negative chirality. Since coupling Weyl fermions to an electromagnetic field results in a non-conservation of the electric charge in a single Weyl node which is related to the chirality of the node (an effect known as chiral anomaly) [Adler, 1969; Bell and Jackiw, 1969], the net chirality in the Brillouin zone (BZ) must vanish. Due to this, Weyl nodes always exist as pairs of opposite chiralities in Weyl semi-metals. This also provides a topological protection against gaping Weyl cones since, to destroy a Weyl node without modifying the net chirality in the BZ, it must annihilate with another Weyl node of opposite chirality [Armitage et al., 2018]. Dirac nodes can be seen as the superimposition of two Weyl nodes of opposite chiralities, yielding a fourfold degenerate node without chirality. Dirac nodes are therefore not topologically protected, although they may be protected by space group symmetries of the material.

In a Weyl semi-metal (WSM), either the time reversal symmetry $\mathcal{T}$ or the inversion symmetry $\mathcal{I}$ must be broken, in order to obtain twofold degenerate Weyl nodes. When both $\mathcal{T}$ and $\mathcal{I}$ are present, the nodes are fourfold degenerate, as in the case of Dirac semi-metals (DSM). When time reversal symmetry is broken, the inversion symmetry makes a given Weyl node at momentum $+\mathbf{k}$ correspond to another Weyl node of opposite chirality at momentum $-\mathbf{k}$. This case corresponds to the minimum number of Weyl nodes possible in a WSM (2). If inversion symmetry is broken however, time reversal symmetry will make a Weyl node at $+\mathbf{k}$ correspond to a Weyl node at momentum $-\mathbf{k}$ with the same chirality. Another pair of Weyl nodes with the opposite chirality must therefore exist to make the net chirality vanish, bringing the minimum number of Weyl nodes to 4.

Interestingly, the lower symmetry of crystal lattices allows for a deviation from the Weyl equation in real materials, by tilting the Weyl cones [Armitage et al., 2018]. Small tilts simply induce anisotropies into the band dispersion relation near the Weyl nodes (See Fig.1.2b, left for a Weyl cone without any tilt), and the resulting phase is called "Type-I". When the tilt is large enough however, the system changes drastically as the Fermi surface becomes open, and the electron and hole pockets touch at the Weyl point (see Fig.1.2b, right). This phase is referred to as "Type-II", and some effects which appear in WSM are expected to be modified in this phase, such as the chiral anomaly (when the magnetic field is aligned with the tilt direction) or the anomalous Hall effect.

1.1.3 Signatures of Weyl topology in transport measurements

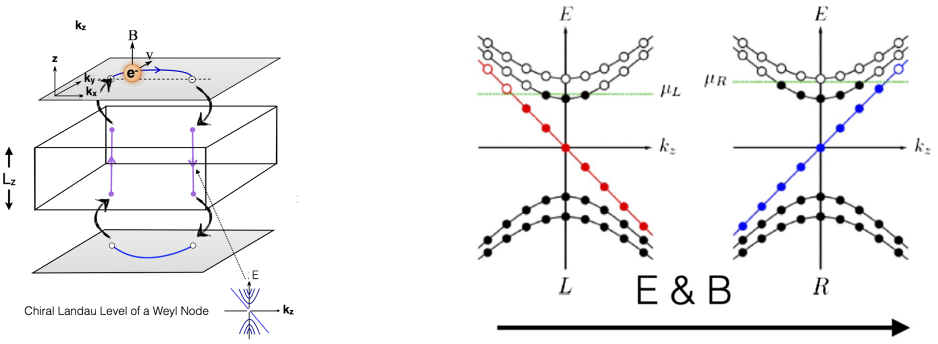

(a) (b)

Figure 1.4: (a) Cyclotron orbit in a hybrid real-momentum space ($\mathbf{k_x}$,$\mathbf{k_y}$,z). Adapted from Potter et al. [2014]. (b) Representation of the band structure of a WSM in a magnetic field, with the two chiral bands represented in red and blue. When an electric field is applied along the magnetic field, a valley imbalance appears between them. Adapted from Armitage et al. [2018]

Fermi Arcs

As written above, one of the common manifestations found in topological phases is the presence of topological surface states (TSS) at the interface with a trivial insulator due to the bulk-boundary correspondence. In WSM, such TSS appear as Fermi arcs, and (at the Weyl node energy) link together the projections of Weyl nodes of opposite chiralities on the surface Brillouin zone (see Fig.1.3a). Fermi arcs have been directly observed through ARPES [Xu et al., 2015; Liu et al., 2016] (see Fig.1.3b), as well as STM measurements [Chang et al., 2016].

Weyl orbits

In transport experiment, Fermi arcs are expected to play a roll in a new type of quantum oscillations. Indeed, when a magnetic field is applied in a direction (z in Fig.1.4a) perpendicular to the direction separating the Weyl node ($\mathbf{k_x}$ in Fig.1.4a), a Lorentz force will act on the surface electrons and make them move along the Fermi arcs. While this would lead to a close path for a conventional Fermi surface, Fermi arcs in a WSM are open and end at the surface projections of the Weyl nodes. When the electrons reach the tip of the arcs, they are then expected to tunnel into the bulk states, where they will be conveyed by the chiral Landau Levels to the opposite surface (see Fig.1.4a). The electrons then proceed to move along the other Fermi arc, and tunnel back into the bulk towards the first Fermi arc. These trajectories, called Weyl orbits, contribute to quantum oscillations and behave like surface states, with a magnetic field dependence only on the vertical component of the field. However, these quantum oscillations also depend on the thickness L_z of the device, since the electrons accumulate a phase $\Phi \propto L_z$ on traversing the bulk [Armitage et al., 2018]. Furthermore in a real material, scattering in the bulk results in an exponential suppression of the amplitude of quantum oscillations which is also thickness dependent.

Chiral anomaly

The most direct consequence of Weyl topology in transport measurements is the chiral anomaly [Nielsen and Ninomiya, 1983] which is, contrarily to the two previous phenomena, a pure bulk effect. If we consider a WSM with one pair of Weyl nodes of opposite chirality, the total charge is conserved due to the vanishing net chirality. However, when applying collinear electric and magnetic fields to the WSM, charges will be pumped from one node towards the other, modifying locally the chemical potential in the vicinity of the Weyl nodes (see Fig.1.4b). A steady state is reached when the chiral pumping is compensated by inter-Weyl node scattering, which gives a chiral current proportional to $\mathbf{E} \cdot \mathbf{B}$. This extra current results in a negative longitudinal magnetoresistance (NLMR) [Son and Spivak, 2013; Burkov, 2015]. It is to be noted however that current jetting can also produce a NMLR [Pippard, 1989]. The NLMR can also be masked in experiments if the material displays a much larger positive orbital magnetoresistance.

1.2 Planar Hall effect in Weyl semi-metals

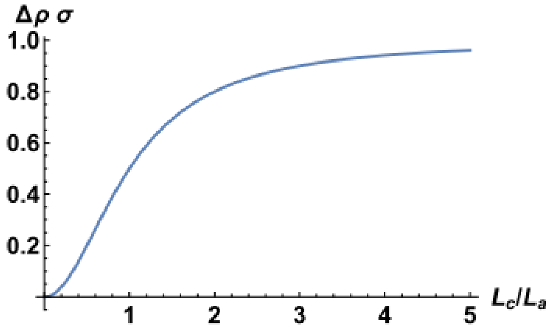

Figure 1.5: Evolution of the amplitude $\Delta\rho$ of the PHE (measured in σ, the Drude conductivity) as a function of $L_c/L_a \propto B$. At low field, $\Delta\rho$ increases quadratically, before saturating at higher fields. Adapted from Burkov [2017]

The appearance of a transverse voltage in a sample when a magnetic field is applied in the sample's plane is called the planar Hall effect (PHE). This transverse voltage is not the result of Lorentz forces acting on the charge carriers, as is the case of the conventional Hall effect, since the magnetic field, the current and the induced transverse voltage are all in the same plane, a configuration in which the conventional Hall effect vanishes.

In the PHE configuration, the transverse voltage is caused by an anisotropy of the in-plane magnetoresistance (MR) $\rho_\perp(B) \neq \rho_{||}(B)$, with $\rho_\perp$ and $\rho_{||}$ the resistivities when the in-plane magnetic field is respectively perpendicular and parallel to the current. It was originally studied in ferromagnetic thin films, in which the magnetization is responsible for the MR anisotropy [Bowen et al., 2005].

Following the discovery of the chiral anomaly in Weyl semi-metals (WSM), Burkov [2017] predicted that a large PHE must develop in these materials as a direct consequence of the chiral anomaly. Indeed the resistivity $\rho_{||}$ (when the magnetic field is along the current) decreases with the field because of the chiral anomaly, while the resistivity $\rho_\perp$ (when field and current are perpendicular) is expected to not be influenced by the magnetic field [Burkov, 2017]. Because of this anisotropy, the longitudinal and transverse resistivities (ρ_{xx} and ρ_{xy}) depend on the angle ϕ between the magnetic field and the current, and can be expressed as

$$\rho_{xx}^{\mathrm{PHE}}(B,\phi) = \rho_\perp - \Delta\rho(B)\, cos^2\,\phi \qquad (1.2)$$
$$\rho_{xy}^{\mathrm{PHE}}(B,\phi) = -\Delta\rho(B)\, cos\,\phi\; sin\,\phi,$$

with $\Delta\rho = \rho_\perp - \rho_{||}$ the amplitude of the PHE. As can be seen from these equations, both the longitudinal and the transverse resistivities are π-periodic signals when rotating the field in the sample's plane, with a $\pi/4$ offset between the two signals, and they share the same amplitude $\Delta\rho$.

In order to characterize the field dependence of $\Delta\rho$, two characteristic lengths can be introduced: the magnetic field related length scale $L_a = D/\Gamma B$, with D the charge diffusion coefficient and Γ a transport coefficient representing the coupling between chiral and electric charges induced by the chiral anomaly, and $L_c = \sqrt{D\tau_c}$, with τ_c the chiral charge relaxation time, which represents the chiral charge diffusion length [Burkov, 2017]. In the low field regime $L_a \gg L_c$, the amplitude of the PHE increases quadratically with the magnetic field, with $\Delta\rho \propto (L_c/L_a)^2 \propto B^2$. When the field becomes larger ($L_a \ll L_c$), the amplitude of the PHE is expected to saturate at the Drude conductivity $\sigma = e^2 g D$, with g the density of states at the Fermi energy. The amplitude of the PHE in this regime is given by $\Delta\rho = 1/\sigma(1 - 2L_a/L)$, with L the sample length [Burkov, 2017].

Later that same year, Nandy et al. [2017] investigated the PHE using a quasiclassical model taking the Berry curvature into account, in the case of both type-I and type-II WSM. They showed that in a type-II WSM, when the current is aligned with the tilting axis of the Weyl cones, the longitudinal and transverse conductivities are no longer π-periodic when rotating the magnetic field, but instead become 2π-periodic. Furthermore, when the magnetic field is along the tilting axis as well, the amplitude of the oscillations increases linearly with the field, contrarily to type-I WSM in which it is always quadratic. This quadratic field dependence is recovered in type-II WSM when the field and the current are orthogonal.

1.3 Superconductivity

In 1911, shortly after he successfully liquefied Helium, Kamerlingh Onnes discovered that the electrical resistance of various metals vanished entirely and suddenly at low enough temperature [Onnes, 1911], a phenomenon now known as superconductivity. In this section, we will recall briefly the main hallmarks of superconductivity, before presenting the two main theories describing conventional superconductivity: the Bardeen–Cooper–Schrieffer (BCS) microscopic theory and the Ginzburg-Landau (GL) phenomenological theory. In that second formalism, we will describe superconductivity at 2-dimensions, which is needed to analyze our experimental results. Finally, we will discuss about the consequences of topology on the superconducting state, and some of its manifestations.

1.3.1 Hallmarks of superconductivity

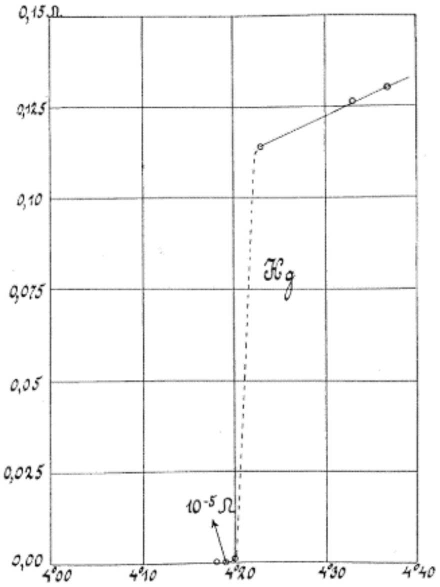

Figure 1.6: Superconducting transition of Mercury, as first reported by Onnes [1911].

One of the most visible consequence of superconductivity is its ability to conduct charges without resistance while the temperature of the material remains lower than a material-dependent critical temperature T_c (see Fig.1.6). This effect was studied extensively, for instance by injecting current in superconducting rings and letting it flow for long periods of time (permanent currents). The time constant describing current decay can be determined by measuring the variations in magnetic field created by the current, using nuclear magnetic resonance, with a lower bound of 10^5 years [Tinkham, 2004]. Another important phenomenon of superconductors, which was discovered in 1933 by Meissner and Ochsenfeld, is the expulsion of magnetic field from superconductors. This phenomenon is known as the Meissner effect, and reflects the fact that superconductors are perfect diamagnets. Initially, attempts to describe this new phase of matter were made using phenomenological equations, such as the London equations [London and London, 1935] which describe the response of superconducting electrons to electric and magnetic fields, to account for the two aforementioned effects.

In the following years, new properties of superconductors were discovered, such as the existence of an energy gap at the Fermi level, which was first observed by specific heat measurements [Corak et al., 1954; Tinkham, 2004].

1.3.2 Bardeen–Cooper–Schrieffer theory

The London model, as well as its non-local generalization by Pippard [1953], were introduced to describe superconductivity phenomenologically. However, at that time, there was no microscopic understanding of the mechanisms leading to superconductivity, and therefore no possibility to calculate phenomenological parameters. In 1957, Bardeen, Cooper and Schrieffer published their Theory of superconductivity [Bardeen et al., 1957], which revolutionized the understanding of this phenomenon. The idea behind this theory is that the Fermi sea is unstable in the presence of attractive electron-electron interactions (no matter how weak they may be), which leads to the binding of electrons into Cooper pairs [Cooper, 1956]. In conventional superconductors, Cooper pairs are formed by electrons of opposite momenta, so that the pairs may have zero total momentum, and opposite spins. At $T = 0$, they extend over a characteristic length ξ_0 called coherence length, and condense into a bound state with energy inferior to the Fermi energy E_F, creating an energy gap in the band structure.

In conventional superconductors, the attractive interaction needed for the electron pairing is usually given by electron-phonon interactions: In a semi-classical picture, the first electron (negatively charged) locally polarizes the medium, by attracting the surrounding nuclei (positively charged) of the lattice, which then attracts the second electron. If this attractive interaction is greater than Coulomb repulsion, the resulting electron-electron interaction is attractive, and superconductivity can happen. It is to be noted however that the BCS pairing mechanism does not specifically require a phonon-mediated attraction, but only an attractive interaction over a range of energy close to E_F. The BCS model is therefore relevant even in the case of superconductors with unconventional pairing mechanisms, for which it however requires some generalization.

1.3.3 Ginzburg-Landau theory

Before the BCS theory was published, another approach to describe superconductors was explored by Landau and Ginzburg [1950] which focuses on superconducting electrons (instead of excitations, as for BCS), describing them with a complex order parameter ψ following Landau's general theory of second order transitions. In the Ginzburg-Landau (GL) approach, the order parameter stands for the local density of superconducting electrons. The GL theory successfully described effects which were beyond the scope of the earlier London equations, such as the spatial variations of the superconducting electron density n_s, as well as identifying two types of superconductors: type I with a first order transition, and type II in which the transition is of second order. In the second case, the superconductor is also expected, above a certain magnetic field, to form vortices of normal phase amid the superconducting phase. The distinction between the two types is made based on the value of the dimensionless Ginzburg-Landau parameter $\kappa = \lambda/\xi$ (with λ the magnetic penetration length and ξ the superconducting coherence length), with $\kappa = 1/\sqrt{2}$ separating type I (inferior) and type II (superior) superconductors.

While the GL is entirely phenomenological, Gor'kov [1959] showed that it could be derived directly from the BCS theory close to T_c. In that context, ψ corresponds to the wavefunction describing the motion of the Cooper pairs' center of mass, and is found to be proportional to the BCS gap parameter Δ. The GL theory is therefore valid, and is also better adapted than the BCS theory in situations involving spatial inhomogeneities as well as for the determination of critical parameters, such as the critical field.

1.3.4 Superconductivity at reduced dimensions

In the context of our study of superconductivity in tr-PtBi$_2$, we are mostly interested in the dependence of observables on accessible parameters (e.g. the angular or temperature dependence of the critical magnetic field), as well as in how these dependences change at reduced dimensionality. We will therefore focus in this section on the observables and parameters to which we have access through transport measurements, such as current, temperature, and magnetic field (and its orientation).

Temperature dependence of the critical field

The easiest parameter we can set in our experiments is the magnetic field, since we can vary it's intensity from much lower to much higher than the critical field, and we can change its orientation in 2D and 3D vector magnets. We also have access to a range of temperatures around the critical temperature, by using a dilution fridge to cool down the sample (see sec.2.1.1). The critical field's temperature dependence is therefore straightforward to measure and gives important information regarding the superconducting state, as shown below.

Considering an infinite sample, it is possible to derive from the GL theory the maximum field H_c at which a superconducting state can nucleate:

$$H_c(T) = \frac{\Phi_0}{2\pi\xi(T)^2}, \tag{1.3}$$

where $\Phi_0 = h/2e$ is the flux quantum (with h the Planck constant, and e the electronic charge), $\xi(T) = \xi_0(1 - T/T_c)^{-1/2}$ is the GL superconducting coherence length (in the plane perpendicular to the magnetic field) and $\xi_0 = \xi(T = 0)$ [Tinkham, 2004]. We can therefore obtain the value of the superconducting coherence length at zero temperature ξ_0 by fitting the temperature dependence of a measured critical field.

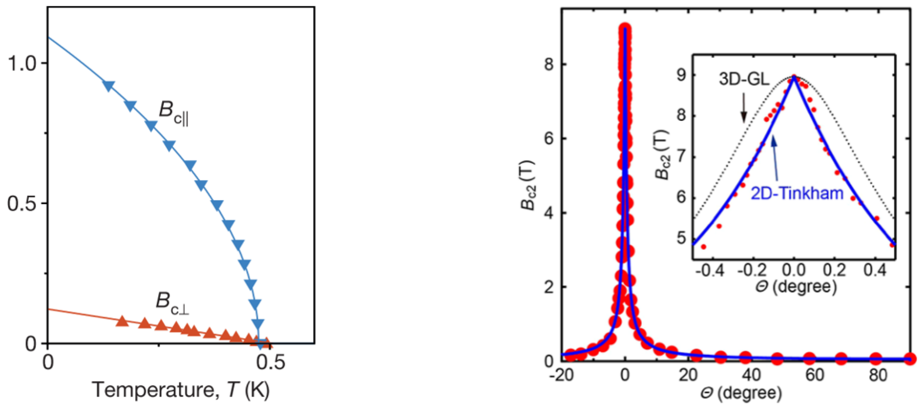

(a) (b)

Figure 1.7: (a) Temperature dependence of the in- and out-of-plane critical magnetic field (in blue and red triangles, respectively) in magic angle bilayer graphene, adapted from Cao et al. [2018]. A clear deviation from linearity can be observed for an in-plane field, as expected for a 2D system. The data was fitted with eq.1.4 and eq.1.5 (blue and red line, respectively). (b) Angular dependence of H_c (refered to as B_{c2}, in red full circles) for a 1T-SnSe$_2$ bilayer, adapted from Zeng et al. [2018]. The inset shows a zoom in on the peak and a comparison of fits using eq.1.6 (3DAGL model, dashed line) and eq.1.6 (2D Tinkham model, blue line).

Eq.1.3 is valid for any direction of the magnetic field as long as we consider a homogeneous bulk sample. If we consider a thin enough superconducting film (i.e. with a thickness d smaller than the out-of-plane coherence length $\xi^{\perp}$) instead, the superconducting state reacts differently to in- and out-of-plane fields, and eq.1.3

becomes

$$H_c^{||}(T) = \frac{\sqrt{12}\,\Phi_0}{2\pi\, d_{\mathrm{SC}}\, \xi^{||}(T)}, \tag{1.4}$$

$$H_c^{\perp}(T) = \frac{\Phi_0}{2\pi\, \xi^{||}(T)^2}, \tag{1.5}$$

with $H_c^{||}$ and $H_c^{\perp}$ the critical field respectively in the in- and out-of-plane directions, $\xi^{||}$ the in-plane coherence length and d_{SC} the thickness of the superconducting state ($d_{\mathrm{SC}} < d$). As expected, the out-of-plane critical field stays the same as in the 3D case (Eq.1.3), with a linear temperature dependence (given by $\xi(T)^2$), since there is no confinement in the film's plane. For an in-plane field however the temperature dependence is significantly modified, with a square root dependence (from $\xi(T)$, see Fig.1.7a). The temperature dependence of the critical field is therefore a useful way of determining if the superconducivity in a sample is confined (2D) or if it behaves as in bulk samples (3D).

Angular dependence of the critical field in thin films

As eq.1.4 and 1.5 show, the critical field is expected to be anisotropic in thin samples due to quantum confinement in the direction perpendicular to the plane. However, even in the absence of quantum confinment (i.e. in the 3D case) it is still possible to observe an anisotropy of the value of the critical field, for instance in the case of finite samples with large aspect ratios. It is therefore interesting to see the impact of quantum confinement on the angular dependence of the critical field in between the two out-of- and in-plane extrema.

Let us consider a sample in the form of a large slab (i.e. very thin compared to its lateral width), but which thickness is still much larger than the superconducting coherence length (3D case). We expect the critical field to reach a minimum $H_c^{\perp}$ for an out-of-plane field, and a maximum $H_c^{||}$ for an in-plane field. In between the two, and in the absence of quantum confinement, the critical field should vary smoothly and is defined intrinsically by the 3D GL anisotropic-mass model (3DAGL) [Tinkham, 2004]:

$$\left(\frac{H_c(\theta)\ cos\ \theta}{H_c^{\perp}}\right)^2 + \left(\frac{H_c(\theta)\ sin\ \theta}{H_c^{||}}\right)^2 = 1, \tag{1.6}$$

with θ the angle between the field and the out-of-plane direction. In the (2D) case of a thin film with quantum confinement in the plane however, the critical field is expected to show a cusp at $\theta = 90°$ (for an in-plane field) [Tinkham, 1963], i.e. a sudden change of sign of its derivative. The full angular dependence is described by the implicit 2D Tinkham model [Tinkham, 2004]:

$$\left|\frac{H_c(\theta)\ cos\ \theta}{H_c^{\perp}}\right| + \left(\frac{H_c(\theta)\ sin\ \theta}{H_c^{||}}\right)^2 = 1. \tag{1.7}$$

Therefore, the temperature and angular dependences of the critical magnetic field make it possible to distinguish easily between a bulk-like, 3-dimensional superconductivity and a quantum-confined, 2-dimensional superconductivity (see Fig.1.7b).

Berezinskii–Kosterlitz–Thouless transition

At three dimensions, long range order can be attained at low enough temperatures, where thermal fluctuations are weak enough to preserve this order. For lower dimensional systems ($d \leq 2$) however, Mermin and Wagner [1966] have shown that no long range order is possible for non-zero temperatures due to the higher impact of thermal fluctuations at these dimensions. In 2-dimensional superconductors, this results in the formation of vortices and antivortices, even in the absence of magnetic field [Tinkham, 2004].

Close to T_c (the GL mean field critical temperature) these vortices are free and, when a transport current is flowing in the film, they become subject to Lorentz forces and drift in opposite directions, which causes flux-flow dissipation and therefore a non-zero resistance. At low (finite) temperature however ($T \ll T_c$), vortices of opposite chiralities are attracted by one another and bind together, forming pinned pairs which are not subject to any net Lorentz force, and therefore the resistance of the thin film vanishes. The temperature above which the vortex pairs begin to unbind is well defined [Kosterlitz and Thouless, 1973], and the related phase transition (from free vortices to pinned vortex pairs) is called the Berezinskii–Kosterlitz–Thouless (BKT) transition [Berezinsky, 1971; Kosterlitz and Thouless, 1972, 1973]. Before being applied to 2D superconductors, it was use to describe 2-dimensional neutral superfluids, for which Kosterlitz and Thouless earned the Noble Prize in Physics in 2016.

The main manifestation of the BKT transition in transport can be seen in the temperature dependence of the current-voltage characteristics $V(I)$. Above the BKT transition temperature T_{BKT}, the unbound vortices give a linear resistance, so that $V \propto I$. Well below T_{BKT}, all vortices should be bound in pairs at $I = 0$, and no resistance is expected. At finite current however, Lorentz forces (caused by the current) exert equal and opposite forces on each vortex of a pair, and start dissociating some of them into free vortices. Right below T_{BKT} the number of free vortices grows as I^2 [Tinkham, 2004], which makes the voltage increase as $V \propto I^3$. This sudden jump in the $V(I)$ at T_{BKT}, from linear to cubic law, is the main hallmark of the BKT transition in the $V(I)$ characteristics. While this transition is robust against disorder, to a certain degree, a broadening of the transition caused by inhomogeneities is expected [Maccari et al., 2017]. This results in a continuous increase of the $V(I)$ power law between T_c and T_{BKT} rather than a sudden jump at T_{BKT} (see Fig.1.8, inset). The transition temperature is defined as the temperature at which the $V(I)$ power law becomes cubic: $V(T_{BKT}) \propto I^3$.

As Halperin and Nelson [1979] have shown (and as was later refined by Benfatto et al. [2009]), the temperature dependence of the resistance of a 2D superconductor is only influenced by the BKT transition close to $T_{BKT} < T_c$. In this regime, we expect $R_{BKT}(T) \propto \exp(-2b/\sqrt{t})$, with the reduced temperature $t = \dfrac{T - T_{BKT}}{T_{BKT}}$, while close to T_c thermal fluctuations dominate and we expect $R_{GL}(T) \sim \xi_0(T - T_c)/T_c$. They introduced an interpolation of the conductivity σ between the GL and BKT regimes, given by

$$\frac{\Delta\sigma}{\sigma_N} = \frac{4}{A^2}\sinh^2\left(2\alpha\sqrt{t_c/t}\right), \tag{1.8}$$

with σ_N the conductivity in the normal state, A a coefficient of order 1, α the vortex-core energy scale and $t_c = \dfrac{T_c - T_{BKT}}{T_{BKT}}$.

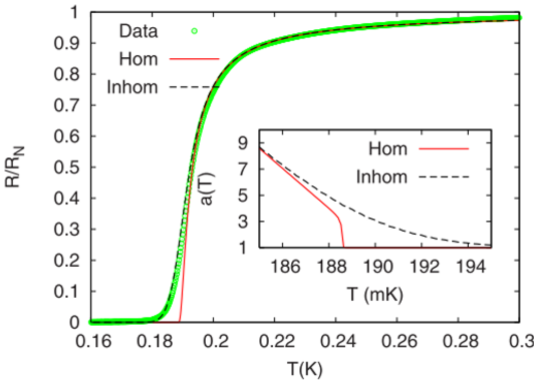

Figure 1.8: Temperature dependence of a 2D superconductor undergoing a BKT transition. The data is fitted with both a homogeneous (Halperin-Nelson) model (red line, eq.1.8) and an inhomogeneous (Benfatto) model (black dashed line, eq.1.9). Inset: Temperature dependence of the V(I) power law exponent $V(T) \propto I^{a(T)}$, for both models. Adapted from Benfatto et al. [2009].

To take into account the influence of inhomogeneities on the transition in real samples, Benfatto et al. [2009] proposed a model with an inhomogeneous superfluid density or, equivalently, a spatial distribution of the T_{BKT} transition temperature. Assuming for simplicity a Gaussian distribution of T_{BKT}, and noting that $R/R_N = 1/(1 + \Delta\sigma/\sigma_N)$ (with R_N the resistance in the normal state), we can express the resistance of a 2D sample as an integral of the local contributions over the distribution of transition temperatures:

$$\frac{R(T)}{R_N} = \frac{1}{\sqrt{2\pi}\delta} \int \mathrm{d}t \, \exp\left(-\frac{(t - T_{BKT})^2}{2\delta^2}\right) \times \left(1 + \frac{4}{A^2}\left[sinh\left(b\sqrt{\frac{t}{T - t}}\right)\right]^2\right)^{-1}, \tag{1.9}$$

with δ the Gaussian spread of T_{BKT} and $b = 2\alpha\sqrt{(T_c - T_{BKT})/T_{BKT}}$. This inhomogeneous model manages to reproduce the "tail" which is sometimes measured in BKT transitions [Reyren et al., 2007], where the resistance doesn't vanish abruptly at T_{BKT} (see Fig.1.8).

1.3.5 Topological superconductivity and low dimensionality

We have discussed so far only about conventional superconductivity. However, when superconductivity occurs in a topological material or at the interface between a trivial superconductor and a material with high spin orbit coupling, it is possible to observe a different kind of superconductivity called topological superconductivity (TSC) [Frolov et al., 2020] and described by non-Abelian statistics, where quasiparticles are neither bosons nor fermions. The most prominent manifestation of TSC is the existence of Majorana bound states (MBS) on the edges of the sample or in vortex cores. Majorana fermions are their own antiparticles, and are sought after in quantum computation to realize topologically protected operations, free from decoherence [Sato and Ando, 2017]. While TSC is usually associated with unconventional non-s-wave superconductivity, a 2D model to realize non-Abelian Majorana zero modes was proposed by Sato [2003] even for s-wave superconductors.

Low dimensional superconductivity in a topologically non-trivial material is particularly interesting. As mentioned in the previous section, when a 2-dimensional superconductors undergoes a BKT transition, vortices and anti-vortices spontaneously form even in the absence of magnetic field, and in topological superconductors these vortices might support MBS in their center. It is therefore theoretically possible to study MBS at zero field in 2D topological superconductors. One promising material for this study is the iron-based superconductor $FeTe_{0.55}Se_{0.45}$

in which MBS have been found in the center of vortices at low fields ($B = 0.5$T) [Wang et al., 2018]. This material also shows a BKT transition for films under $d \sim 6$nm [Tang et al., 2019], but no study has yet found MBS at zero field in BKT systems.

2 | Methods

We present in this chapter the measurement techniques used in our study of tr-$PtBi_2$ (cryogenics and low-noise transport techniques), as well as the fabrication techniques used to make the samples we studied.

At room temperature, charge transport in metals is dominated by phonon scattering [Ziman, 2001], and the thermal broadening is larger than the energy scale of most quantum effects, which suppresses them. In order to study the quantum properties of materials, such as Berry curvature related effects or superconductivity, with electrical transport, it is therefore necessary to decrease the temperature enough to allow these effects to be measurable. The first steps in this direction were made by the liquefaction of different room-temperature gases, beginning with oxygen in 1877 (reaching $T \sim$ 90K) and nitrogen in 1882 ($T \sim$ 77K). The most significant development came in 1908, with the liquefaction of ^{4}He by Kammerling Onnes, reaching $T \sim$ 4.2K, which led to, among other things, his discovery of superconductivity in mercury in 1911. In the case of the superconducting transition studied in this manuscript, the temperature needs to be lowered even further, down to 100mK, which requires the use of a ^{3}He - ^{4}He dilution refrigerator, as described in this chapter.

At low temperature, the resistivity of metallic materials may drop considerably. In order to maintain a good signal-to-noise ratio without increasing the current (to avoid any heating effect), we may decrease the aspect ratio of the structures studied, for instance by fabricating nano-structures, or by reducing their thickness, e.g. through exfoliation for van der Waals materials. In addition to increasing the signal-to-noise ratio of experimental measurements, this also allows for the study of materials at reduced dimensionality. The use of nano-structures patterned by e-beam lithography also gives us a greater control on the geometry and the aspect ratio of the contact scheme, and makes it possible to study more homogeneous devices.

In this chapter, we will describe in the first section the operation of a ^{3}He - ^{4}He dilution refrigerator, which was used in our experiments to reach sub-kelvin temperatures, as well as our experimental setup for low-noise electronic transport measurements. In the following section, we will present the methods used to contact macroscopic crystals, as well as the fabrication and patterning of nano-structures.

2.1 Low temperature and low noise measurements

In order to study superconductivity in trigonal-PtBi$_2$ (tr-PtBi$_2$), we had to reach temperatures lower than $T_c \sim 300$mK. Such low temperatures were obtained using ^{3}He - ^{4}He dilution refrigerators, which were inserted in either a 12T-1T magnet (for macro-structures) or a 6T-2T-2T magnet (for nano-structures) to perform magnetotransport measurements.

2.1.1 ^{3}He - ^{4}He dilution refrigerator

A dilution refrigerator is a system which uses the endothermic diffusion of ^{3}He into ^{4}He in order to reach temperatures as low as 2mK. Contrarily to "single-shot" cryogenic systems, which can only stay at low temperature for a limited time, dilution refrigerators function continuously.

Fig.2.1 represents the schematics of a dilution refrigerator. The main idea is that, at $T < 800$mK, a mixture of ^{3}He and ^{4}He separates in two phases, a concentrated ^{3}He rich phase and a dilute ^{3}He phase. At $T = 0$K, the concentrated phase is made of pure ^{3}He and the dilute phase is made of 93.4% ^{4}He and 6.6% ^{3}He. The key idea is to use the fact that the diffusion of ^{3}He from the concentrated phase to the dilute phase is endothermic. The phase separation happens in the mixing chamber, the coldest part of the dilution refrigerator (to which the cold finger, with the sample, is attached), and ^{3}He is being circulated from the dilute phase back to the concentrated phase, to keep the cooling process going continuously, as we will see below.

The dilute phase in the mixing chamber, which is below the phase interface, is connected to the "still", a chamber which contains an interface between the liquid dilute phase, and a gas phase which is maintained at low pressure by a system of pumps at room temperature. ^{3}He having a larger saturation vapor pressure than ^{4}He, the vapor is made mostly of ^{3}He (at 96%), even though the dilute phase has a very low concentration in ^{3}He (only about 0.7%). The ^{3}He vapor is then reinjected into the system, where it is cooled down to 4.2K by the Helium bath in

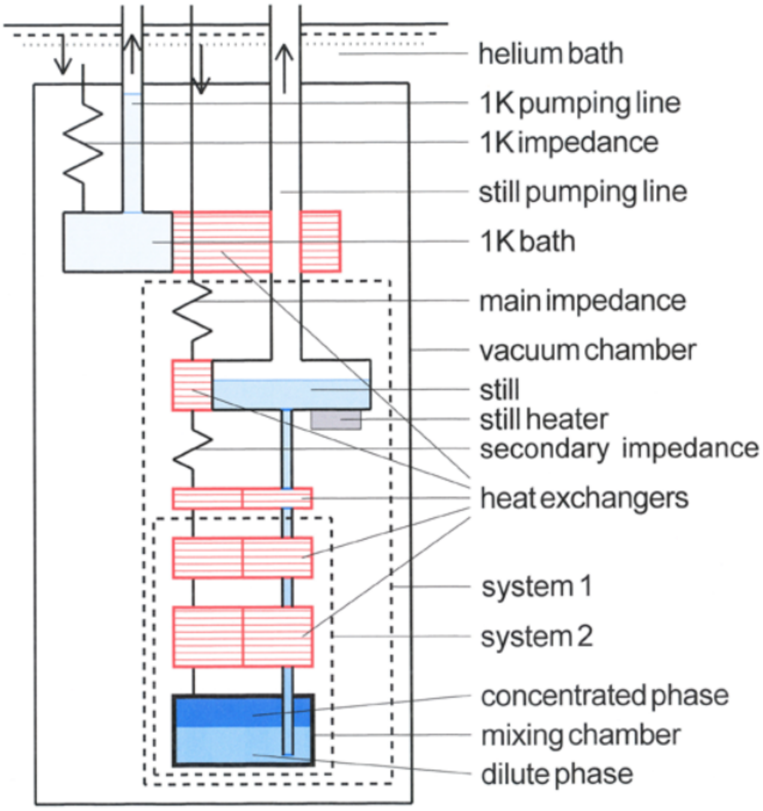
helium bath
1K pumping line
1K impedance
still pumping line
1K bath
main impedance
vacuum chamber
still
still heater
secondary impedance
heat exchangers
system 1
system 2
concentrated phase
mixing chamber
dilute phase

Figure 2.1: Schematics of a ^{3}He - ^{4}He dilution refrigerator, adapted from De Waele [2011].

which the entire refrigerator is immersed. The ^{3}He then enters a vacuum chamber, in which it is put in contact with a pumped Helium bath ("1K bath") by a heat exchanger, and is cooled down to around 1.2K. It is then further cooled down by Joule-Thomson effect in the main impedance, before thermalizing with the still to a temperature below 700mK, and passing through a further Joule-Thomson (secondary) impedance. Lastly, the incoming ^{3}He is cooled down by the mixture coming from the mixing chamber through discreet and continuous heat exchangers. The cold incoming ^{3}He then reaches the mixing chamber, where it diffuses into the dilute phase in an endothermic process. In order to enhanced the flow of ^{3}He mixture circulating in the fridge in the steady state (and therefore increase the cooling power), a small heating power is applied to the still.

2.1.2 Low noise electrical measurements technique

As we mentioned previously, the resistivity of metals (and semi-metals) decreases with temperature. One of the challenges of transport measurements at cryogenic temperatures is therefore to measure such low resistivities, and to maintain a low-enough signal-to-noise ratio so as to be able to measure small variations of this resistivity. In order to get low noise transport measurements at low temperature, several techniques are used.

First, since we are technically studying samples' resistance (through voltage measurements) rather than their resistivity, it is possible (as mentionned previously) to enhance the signal by increasing the aspect ratio of the structure, since $R_m = \rho/t \cdot L/W$, with R_m the measured resistance, ρ the resistivity, and L,W and t the length, width and thickness of the structure, respectively. In the case of layered van der Waals materials such as tr-PtBi$_2$, it is possible to exfoliate thin flakes (down to $t \sim 40$nm in our case), with an aspect ratio L/W superior to one (see sec.2.2.2), increasing the structures' resistance to $R_m > 1\Omega$.

Second, it is possible to increase the signal measured by flowing a larger current through the sample, although this technique has three limitations: it may affect the system studied (e.g. by turning a superconducting sample into a normal metal for $I > I_c$); For low resistivity samples (e.g. macro-structures), it may cause significant heating through the resistive measurement lines ; It can also lead to a rise of the electronic temperature of the system. Indeed, at very low temperature (typically, $T < 1$K), the electron-phonon coupling is greatly reduced, and electrons may not be at equilibrium with the phonon bath of the crystal lattice. This happens when the size of the device becomes of the order of magnitude or smaller than the electron-phonon inelastic length. In these conditions, applying a large voltage to a sample will cause the temperature of the electrons to increase with respect to the thermometer located near the sample. A general rule for determining a maximal voltage V which can be applied to a sample without increasing the temperature past the system's temperature T_s is $eV \leq 4k_BT_s$. At base temperature, this corresponds to a few tens of μV.

In order to measure these low voltages, and their correspondingly low variations, we use lock-in amplifiers (shortened below to "lock-in"). These devices deliver a sine wave signal at a given frequency f_0, and are used to flow an AC current through the sample by using a polarization resistance of 1MΩ, much larger than the resistance of the sample. The lock-in is then used to measure the response of the sample at that same frequency f_0, thus avoiding the $1/f$ and the 50Hz noise of the electronic devices. Other lock-ins can be synchronized to the same frequency, to measure different resistances of a single sample simultaneously. With this system, we are able to measure signal variations down to about $5\mathrm{nV/Hz}^{1/2}$ of amplitude, which corresponds to the intrinsic noise of the lock-ins. Moreover, in order to avoid heating through radio frequency (RF) signals, the dilution fridge is equipped with low-pass RC filters.

The samples were measured in "4-probe" configuration, i.e. by applying a current between a pair of contacts, and measuring the voltage between a different pair of contacts, to avoid measuring the contact or measurement-line resistances.

Differential resistance

When measuring with lock-ins, it is possible to measure the differential resistance of a sample by applying a DC current in addition to the AC current applied with the lock-in. Indeed, if we consider $I_{AC} \ll I_{DC}$, the measured voltage can be expanded into Taylor series as

$$V(I_{DC} + I_{AC}) = V(I_{DC}) + I_{AC} \cdot \left.\frac{\mathrm{d}V}{\mathrm{d}I}\right|_{I_{DC}} + I_{AC}^2 \cdot \left.\frac{\mathrm{d}^2V}{\mathrm{d}I^2}\right|_{I_{DC}} + ... \tag{2.1}$$

$$= V_{DC} + V_\omega + V_{2\omega} + ... \tag{2.2}$$

with V_ω and $V_{2\omega}$ the first and second harmonics, respectively. Since lock-ins filter only the response at the frequency of I_{AC}, the voltage read by (the first harmonic of) the lock-in is simply $I_{AC} \cdot \left.\frac{\mathrm{d}V}{\mathrm{d}I}\right|_{I_{DC}}$, which is directly proportional to the differential resistance of our samples. This is very advantageous, as analytically differentiating measured signals (especially more than once in a row) can introduce a large noise, while integration doesn't. With this method, it is possible to obtain $V(I)$ by integrating.

Superconductivity in macroscopic crystals was measured using DC sources operated in a delta mode, a method that is particularly adapted to the measurement of low resistances.

2.2 Sample fabrication

In this work, we studied two different kinds of samples: macro-structures and nano-structures. The first category corresponds to as-grown crystals, typically a few milimiters in size and less than 1mm thick. The second category corresponds to flakes mechanically exfoliated onto substrates, and are typically 10-20μm in size and under 150nm thick. In this section, we will describe the fabrication of these samples, and the techniques used to contact them.

2.2.1 Macro-structure fabrication

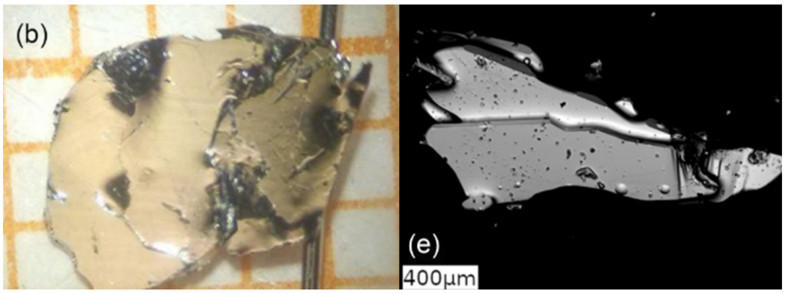

Figure 2.2: Optical (b) and SEM backscattered electrons (e) images of tr-$PtBi_2$ crystals. Adapted from Shipunov et al. [2020]

In order to make macro-structures, we selected crystals with flat (reflecting) facets, and a platelet shape (i.e. without inclusion with a different c-axis). Because of their layered nature, the crystals were very soft, and often included parts which were partially torn away (see Fig.2.2). We discarded these crystals, and only contacted the ones which looked pristine. The crystals were contacted in four-probe configuration using sliver wires and epoxy. In order to avoid a short circuit with the conducting chip carrier, the crystals were first deposited on insulating Kapton tape. An optical picture of such a contacted crystal (MS2) is shown in the inset of Fig.4.3.

2.2.2 Mechanical exfoliation

In 2005, Novoselov and Geim managed to fabricate graphene monolayers for the first time [Novoselov et al., 2005]. To do so, they developed a simple technique called mechanical exfoliation. This technique has contributed to the rise of the very active area of 2D materials, and is applicable to the wide range of van der Waals materials. In these materials, the crystallographic structure is made of layers with strong intra-layer interactions, and weak van der Waals inter-layer interactions. Exfoliation is the general process consisting in separating these layers from one another. Different types of exfoliation exist, such as liquid exfoliation (where a crystal is submerged in a liquid, usually a solvent such as IPA or acetone, and undergoes an ultrasonication treatment), or atomic force microscopy (AFM) exfoliation (where the top layers of a pile are "scratched" away by using an AFM tip in contact mode). In this work, we used mechanical exfoliation, which is the most widespread method to obtain large, high quality exfoliated flakes.

Mechanical exfoliation consists in the repeated act of cleaving a layered crystal, by attaching to both sides of the crystal and pulling them apart. The most common tool used for this purpose is adhesive tape, although it is also possible to use other types of adhesive, such as PDMS or electrostatic tape. This technique has many parameters which can be varied to adapt to different materials.

Tape

The first and most obvious parameter is the choice of the type of adhesive tape. Since mechanical exfoliation works by cleaving layers from each other, the tape must have an adhesiveness superior to the inter-layer van der Waals interactions: If the tape is not adhesive enough, a crystal will be transferred between the two tapes rather than be cleaved. On the other hand, if the tape is too adhesive, it will be difficult to cleave the crystal, as it will simply stay on the first part of the tape, since the glue of adhesive tape tends to cover the sides of the crystal (to some extent) rather than stay in contact with the lowest layer only. Another important thing to consider is how well the tape's glue holds to itself. Indeed, some tapes have an adequate adhesive power, but leave a substantial amount of glue on the substrate to which the exfoliation is transferred, or even on the flakes themselves. This can be particularly detrimental in the case of transport measurements, since glue residues on an exfoliated flake may lay between the metallic contacts and the material. Stronger adhesive tapes in particular tend to leave more significant traces of glue onto samples and substrates.

The substrate used in the exfoliation must also be considered carefully. Indeed, the last step of an exfoliation is usually to transfer the cleaved crystal parts to a chosen substrate. Ideally, the way this would work would be that whole crystals are not actually transferred from the tape to the substrate, but instead their surface would attach to the substrate and they would be cleaved one last time. In this case, the flakes present on the substrate show a freshly cleaved and very clean top surface. This is the case of graphene or $MoTe_2$ for instance. If the flakes have difficulty exfoliating from the tape (due to e.g. strong inter-layer interactions, or low adhesiveness with the tape), they may be transferred as such to the substrate, potentially keeping traces of glue on their top surface (or even between the flakes and the substrate in case of transfer between the two tapes). This is the case for tr-$PtBi_2$.

For these reasons, it is important to select the correct tape for exfoliation, to eliminate, or at least reduce, these issues. Unfortunately this selection process, like most other aspects of this technique, is based on trial-and-error, which is extremely time consuming. One part, though, is pretty straightforward, but still holds a lot of importance: the color or transparency of the tape. As it is important to be able to visualize the results of an exfoliation before transfer, the tape must make a good optical contrast with the crystals (e.g. no black tape for dark graphite crystals, and no white, opaque tape for white Boron Nitride crystals). In some cases, transparent PDMS (either as tape, available commercially with different adhesiveness, or as films mixed and baked by oneself) can be a good alternative to other adhesive tapes, since PDMS leaves no residues on substrates or flakes. Its adhesive power is lower than most tapes though, so it is difficult to use with materials with strong inter-layer interactions, such as tr-$PtBi_2$. Another option can be electrostatic tape, which also doesn't leave any residue, and can be useful when dealing with particular materials.

In this work we used Tesa Krystall-Klar adhesive tape (transparent), as it was useful in exfoliated numerous thin flakes, and left low amount of glue on the substrates. It is to be noted that manufacturers regularly change the adhesive glue formula, without necessarily re-labeling the tape, which can change their suitability as exfoliation tape. It is therefore advised, once a suitable tape has been found, to store significant quantities of it in order to avoid future problems.

Exfoliation

The exfoliation process itself is quite straightforward, however it is still important to highlight a few important point, so they are not forgotten as they are still important to the final quality of the exfoliation (i.e. size, cleanliness, thickness and quantity of exfoliated structures). The main part of the exfoliation process is to stick repeatedly a piece of tape (on which is attached a crystal) onto another adhesive surface. The most efficient and clean way to operate is by using tape as both surfaces, and preferably a single piece of tape used on both ends (which is easier to manipulate). This process is repeated a certain number of times, depending on the difficulty of the exfoliation. When sticking the tape onto itself, the aim should be to have a very dense area with many crystals (see Fig.2.3), while being careful to not stick two parts with crystals onto one another (which would damage them).

A light pressure of the pad (the soft part) of the finger can be applied on the tape in order to make sure the crystals stick to both sides of the tape. Depending on the fragility of the material, a pressure too high may provoke intra-layer breaking,

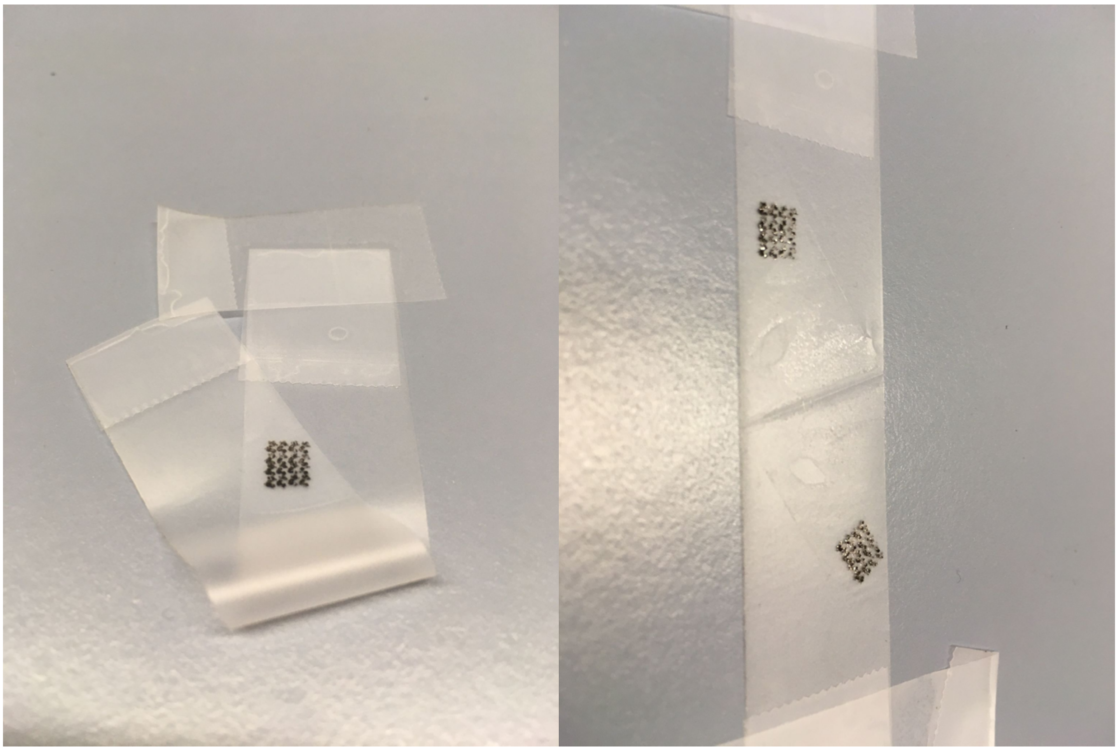

(a) (b)

Figure 2.3: Optical pictures of scotch tape during an graphite exfoliation. (a) The tape is stuck on itself during the initial exfoliation procedure. The two mother tapes are obtained by straightening the tape (b). The black squares are made of the successive iterations of the exfoliation of a single graphite crystal.

which results in tiny, densely concentrated flakes on the final substrate, instead of large, distant flakes. For most materials which present no particular exfoliation difficulty, sticking the tape to itself enough time to have an exfoliation area equivalent to that of the substrate used (about 5x5mm^2) is enough to obtain very thin flakes.

In order to improve the number of flakes obtained from a single crystal, we use the two pieces of tape obtained with this technique as so called *mother tapes*, and exfoliate from them once more using a new piece of tape (simply sticking them together once, as described above). These tapes are called *daughter tapes*, and are then transferred onto the substrates, as explain further below. It is usually possible to use two daughter tapes per mother tape, as well as both mother tapes, and so an exfoliation typically gives 6 substrates (one per tape). This is of course influenced by the difficulty of cleaving the material, and by how thin the original crystal was.

Choice of substrate

Once the tape is ready, the exfoliated crystals can be transferred to a substrate. We use Si^+/SiO_2 substrates, with a 285nm layer of oxide, because of two reasons: first, this substrate has an insulating surface, which makes it possible to do transport measurements, and a conductive bulk, which allows for applying a gate voltage to eventually tune the Fermi level of thin structures. Second, polished Si has a reflecting surface, and when a (partially transparent) thin flake is deposited at the surface of the substrate, the light reflecting at the Si surface will undergo multiple reflections at the SiO_2 surface and at the top of the flake, leading to Fabry-Perot interferences and different color contrasts for different flake thicknesses, which allows for easy optical determination of interesting flakes [Li et al., 2013; Menon et al., 2019].

An oxide layer of 285nm corresponds to the optimal thickness for enhanced optical contrast with graphene [Novoselov et al., 2005]. It is also a good choice for many other materials. The substrates should be cleaned before the exfoliation, by letting them bath in acetone and Isopropyl alcohol (IPA), preferably with a low-power ultrasonication ($\sim 30\%$), to help detach any durt which may be on the substrates. After this initial cleaning, it is possible to use Piranha acid ($H_2SO_4 + H_2O_2$) on the substrates, which removes most organic contamination. This step is necessary when making ultra-high quality few-layer structures, but was not considered useful in our case, and was therefore skipped.

Transfer

In order to transfer flakes from the tape to the substrate, the tape is stuck to the substrate from above (making a "U-shape" with the tape), to ensure as little air is trapped between tape and substrate, which might cause areas of the tape to not touch the substrate. Then, the tape-on-substrate should be rubbed gently, to ensure that the flakes stick to the substrate without destroying them. One technique is to use the back of a pen cap (e.g. Stabilo), and apply a slight pressure to it. Applying too much pressure scratches and destroys the structures, while not applying enough makes the structures not stick to the substrate. This rubbing should last about 2 minutes, and be done in different directions, to optimize the chances of successfully transferring structures to the substrate.

Once this is done, the tape is taken off the substrate as slowly as possible (about 1 or 2 minutes for a 5mm long substrate), while keeping an angle between the tape and the substrate of about 80°. With such an acute angle, the flakes are more likely to exfoliate correctly and to not be broken , which might be related to the fact that applying an obtuse angle would cause the crystals to bend backwards and break.

Characterization and EBL patterning

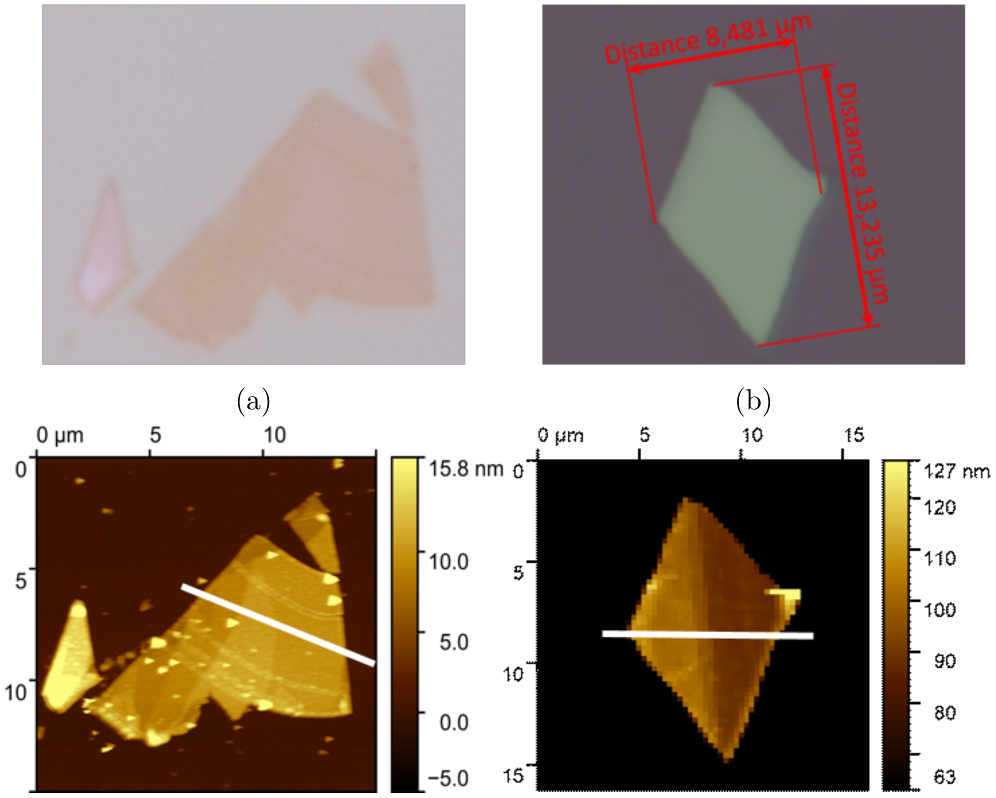
Distance 8,481 µm
Distance 13,235 µm
0 µm
5
10
0
5
10
15.8 nm
10.0
5.0
0.0
−5.0
0 µm
5
10
15
0
5
10
15
127 nm
120
110
100
90
80
63

(a) (b)

(c) (d)

Figure 2.4: (a) and (b): Optical pictures of $MoTe_2$ (a) and tr-$PtBi_2$ (b) exfoliated flakes. The $MoTe_2$ shows a color contrast typical for flakes thinner than ∼ 10nm, while the $PtBi_2$ flake shows a uniform color (which doesn't change with thickness, down to 40nm). (c) and (d): AFM images of the flakes in (a) and (b), respectively. (c) The AFM reveals the flake is 8nm thick, with a monolayer and bilayer steps (along the white line). The bilayer step is faintly visible in the optical image. (d) A 10nm step is revealed by AFM (along the white line, 95nm to 85nm), which was not visible by optical microscopy).

Such mechanical exfoliation is a statistical process: the goal is to produce many exfoliated flakes, on different substrates, and then to search for suitable flakes. Thus, after an exfoliation, the substrates should first be observed by optical microscopy. The criteria for suitable flakes depend on the specific project, but usually involve lateral size, thickness (determined by the color contrast, as shown in Fig.2.4a), shape, flatness/cleanliness and environment (e.g. a flake must be "accessible" for contacting, and can't be surrounded by thick structures, or be too close to a substrate edge). AFM is then used to determine the surface state of a flake, as well as its precise thickness. In the case of tr-PtBi$_2$ however, all thicknesses (down to $\sim$ 40nm, the thinnest exfoliated flake we found) appear with the same color (see Fig.2.4b), due to the metallicity of tr-PtBi$_2$. In this case, we relied on AFM research to find thin flakes.

The flake is contacted using standard EBL patterning techniques, with a modified SEM. The desired contact geometry is patterned into PMMA (poly(methyl methacrylate)), which is a positive electron sensitive resist. The PMMA serves as a lithography mask for depositing the metalic contacts, made of a thin sticking layer of Cr (typically 10nm), and a thicker conducting layer of Au (up to about 140nm, to cover the flake). this process is described in details in Labracherie [2021]. The contacts on the flake are connected to large metallic pads, which are then bonded to the chip carrier used in our setups.

2.2.3 Samples studied

In this work, we present results on both macro- and nano-structures. The first macro-structure, MS1, was contacted and measured by Dr. Federico Caglieris. Three additional crystals, MS2, MS3 and MS4, were contacted and measured by Valentin Labracherie: MS2 is a pure tr-PtBi$_2$ crystal, while MS3 and MS4 were grown with Rh doping of respectively 3% and 10%.

Five nano-structures, S1-S5, were measured, with thicknesses of respectively 60nm, 60-120nm, 41nm, 70nm and 126nm. Most of the results presented in this work are from S1, S3 and S5.

3 Transport and planar Hall effect in trigonal-PtBi$_2$

PtBi$_2$ has attracted a lot of interest in the last 5 years, beginning with the discovery of a very large linear magnetoresistance in the pyrite crystal structure [Gao et al., 2017]. The trigonal crystal structure, which also shows strong spin-orbit coupling as well as a breaking of the inversion symmetry, has been predicted to have a topological band structure with triply degenerate points [Gao et al., 2018]. A strong Rashba-like spin-splitting was also measured in this structure [Feng et al., 2019], as well as pressure-induced superconductivity [Wang et al., 2021]. In this chapter, we will start with a review of the recent literature on PtBi$_2$, before presenting band structure calculations for the trigonal crystal structure which were realize for this work. We will then discuss transport measurements results in macroscopic single crystals, as well as in exfoliated structures of trigonal-PtBi$_2$ (tr-PtBi$_2$).

3.1 Crystalline configurations

3.1.1 Pyrite configuration

The pyrite configuration of PtBi$_2$ (cubic, space group $Pa\overline{3}$) was predicted to be a 3D Dirac semi-metal candidate by Gibson et al. [2015], because of its symmetries and charge compensation. Two years later, it was found to show an extremely large and unsaturated magnetoresistance (MR), up to 1.12×10^7 % at 33T and 1.8K [Gao et al., 2017], with a linear magnetic field dependence above $B = 14$T Zhao et al. [2018]. This linear dependence, often found in Dirac and Weyl semimetals [Feng et al., 2015; Kushwaha et al., 2015; Shekhar et al., 2015; Huang et al., 2015], could make for a MR of 2.2×10^7 % at 60T, even higher than for

WTe_2 [Ali et al., 2014]. At lower fields, the carrier densities can be extracted from the Hall resistance, and show a near perfect charge compensation [Zhao et al., 2018], as expected theoretically. This compensation between electron and hole pockets was later confirmed at higher field (55T) by a study of quantum oscillations. Both studies by Gao and Zhao show that pyrite-$PtBi_2$ samples with a higher Residual Resistance Ratio (RRR, see 3.3.1) also have a higher MR, revealing a link between high crystal quality and MR in this material. Surface states have also been observed in pyrite-$PtBi_2$ by ARPES measurements [Wu et al., 2019; Thirupathaiah et al., 2021]. However, the surface states observed formed Fermi contours instead of Fermi arcs, because of their lack of topological protection [Wu et al., 2019; Kargarian et al., 2016].

In addition to these properties, pyrite-$PtBi_2$ has also been shown to become superconducting under an external pressure of 13GPa [Chen et al., 2018]. Interestingly, the onset of the superconducting transition ($T_c \sim 2.2$K) does not seem to vary at higher pressure, and no structural transition is observed.

3.1.2 Trigonal configuration

Contrarily to pyrite-$PtBi_2$, tr-$PtBi_2$ (space group $P31m$ [Shipunov et al., 2020]) is a layered van der Waals material, making it possible to thin it down through exfoliation, and was not predicted to be a Dirac semi-metal. Nonetheless, tr-$PtBi_2$ also shows a large and unsaturated magnetoresistance, reaching 1.3×10^5 % at 32T and 1.8K [Gao et al., 2018] for the highest quality structures (highest RRR). The sub-quadratic power-law dependence has been attributed to either linear Dirac dispersion [Gao et al., 2018], or to open orbits in the Fermi surface [Wu et al., 2020]. Just as for pyrite-$PtBi_2$, the trigonal configuration was also found to be superconducting under pressure [Wang et al., 2021], with $P_c \sim 5$GPa and $T_c \sim 2$K, and the critical temperature also shows a very weak dependence under pressure, up to 48GPa.

These properties resulted in a rise of interest in $PtBi_2$ in the past couple of years. We focus in this work on tr-$PtBi_2$.

3.2 Band Structure Calculations

The band structure of tr-$PtBi_2$ was calculated by Dr. Jorge I. Facio (ITF, IFW Dresden), from the crystal parameters obtained by powder XRD measurements [Shipunov et al., 2020]. Fully relativistic density-functional theory (DFT) calculations, including spin-orbit coupling, were performed, and the energy bands

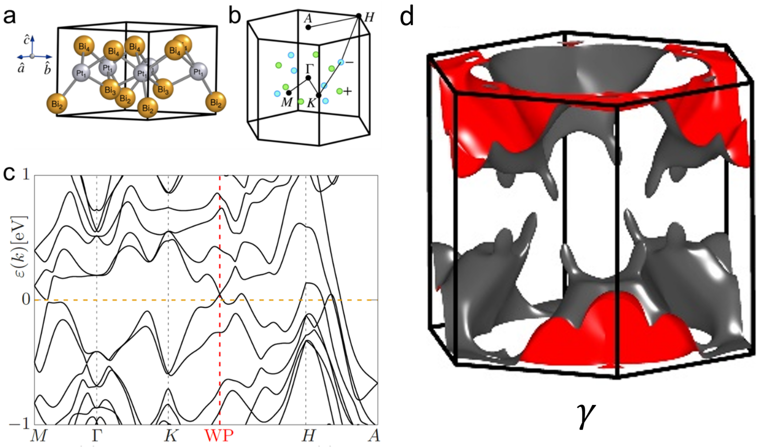

Figure 3.1: (a) Crystal structure of tr-$PtBi_2$. (b) Brillouin Zone. Green and blue points correspond to Weyl nodes with respectively positive and negative chirality. (c) Band structure along the path shown in (b). The path includes a Weyl node (red dashed line) at 48meV above the Fermi energy (orange dashed line). (d) Fermi surface of the γ pocket, obtained from DFT calculations. The outer (inner) face is colored gray (red).

obtained along the Brillouin Zone (BZ) path represented in Fig.3.1.b are shown in Fig.3.1.c. The band structure shows a semi-metallic nature, as has already been reported [Gao et al., 2017; Shipunov et al., 2020], with a number of bands crossing the Fermi energy and creating several electron and hole pockets. Since the inversion symmetry $\mathcal{I}$ is broken in non-centrosymmetric tr-$PtBi_2$, band crossings at Weyl nodes are allowed. We found 12 symmetry-related Weyl nodes, 48meV above the Fermi energy (see Fig.3.1:c). 6 nodes are related by combinations of three-fold rotation and reflection symmetries (Fig.3.1:b, in green), and the 6 others are related to them by time-reversal symmetry (Fig.3.1:b, in blue).

The band structure calculations indicate that the Weyl cones are only slightly canted (see Fig.A.2:a), making tr-$PtBi_2$ a type-I Weyl semi-metal. The band associated with the Weyl node, called γ, has a larger nearby pocket, and the two are merged together at the (DFT calculated) Fermi energy (see Fig.A.3). The Fermi surface corresponding to the γ band at the Fermi energy is represented in Fig.3.1.d, and shows finger-like extremities, where the Weyl nodes are located. This is similar to calculations performed by Jiang et al. [2020] (band III in their paper), who found these fingers connect across the entire BZ, forming "Fermi tubes", with an canted angle ranging from 20° to 30°. The difference between Fermi tubes and unconnected fingers can probably be attributed to a slight difference in the Fermi energy between the two studies.

In order to investigate for Fermi arcs connecting the Weyl nodes in the surface electronic structure, the band structure of a semi-infinite slab along the [001] direction was calculated. Clear spectral weight can be seen connecting Weyl nodes of opposite chirality (see Fig.A.4). Interestingly, we found that Fermi energy contours in tr-$PtBi_2$ surface states are highly sensitive to the surface termination, with the Bi_2−terminated surface showing a much more intense spectral weight than the Bi_4−terminated surface.

3.3 Magnetotransport characterization

In this work we prepared and measured a number of single crystals, both in the form of macro-structures and nano-structures (obtained by exfoliation). While many properties of the material (e.g. carrier density and mobility) are expected to remain similar between the two (provided the nano-structures remain in a "bulk-like" thickness range, where the band structure is not affected by quantum confinement effects), some differences are to be expected. Mechanical exfoliation may damage the crystal structure, inducing defects which increase the resistivity of the exfoliated structures. It can also produce intra- and inter-layer strain, which can potentially modify some behaviors in nano-structures. Generally, nano-structures should display a higher resistance due to their higher aspect ratio, which gives a better signal-to-noise ratio in our measurements and allows to reveal and study many details otherwise inaccessible in macro-structures.

In this section, we show a detailed characterization of a macro-structure through transport measurements, and a comparison with a nano-structure.

3.3.1 Macro-structures

To characterize our macro-structures, we used a 15T cryostat with a lambda plate, which works down to temperature of about 2.5K, and an insert equipped with a piezo-driven 2D-rotator, allowing us to tilt the sample with respect to the direction of the field. The structure we measured (MS1) was about 1.5mm in length and width, for around 100µm of thickness. Contacts were taken by hand using silver wires and epoxy, and attached to the top surface of the crystal in 4-probe measurement configuration. MS1 was contacted and measured by Dr. Federico Caglieris (IFF, IFW Dresden, now CNR-SPIN Genova), although we performed the analysis.

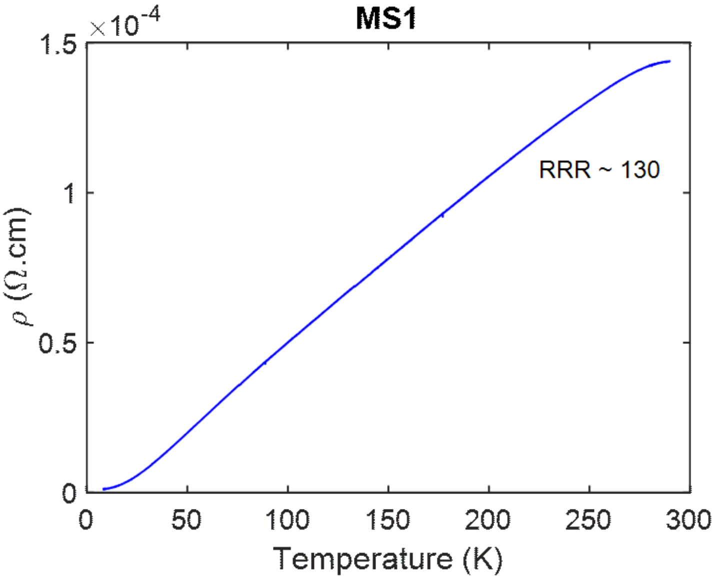

Figure 3.2: Temperature dependence of a macroscopic sample's resistivity between room and liquid-Helium temperature, giving a residual resistance ratio of 130.

The cooldown of the structure shows a typical metallic temperature dependence of the resistance, with an almost linear dependence at high temperature ($T > 35$K) and a higher order dependence at lower temperatures ($T < 35$K) [Ziman, 2001], before stabilizing at about 4K. The remaining resistance is induced by the defects of the crystal structure, which dominate at low temperature when electron-phonon interactions are suppressed. We can determine the $RRR = \dfrac{\rho(300K)}{\rho(4K)} \sim 130$ (with ρ the resistivity, see Fig.3.2), which indicates the good crystalline quality of the crystal. This ratio is similar to that of Xing et al. [2020] (162), but smaller than for Gao et al. [2018] (640).

Magnetoresistance

We studied the magnetoresistance (MR) of MS1, at $T = 5$K and for different orientations of the field with respect to the [001] direction of the crystal. We performed magnetic field sweeps for both opposite directions of the field (i.e. towards positive and negative fields), in order to symmetrize the longitudinal voltage in field. We measured this field dependence for angles ranging from $\theta = -30°$ to $\theta = 120°$, with θ the angle between the direction of the field and the [001] crystal direction. Fig.3.3 presents the symmetrized relative MR (in %), defined as

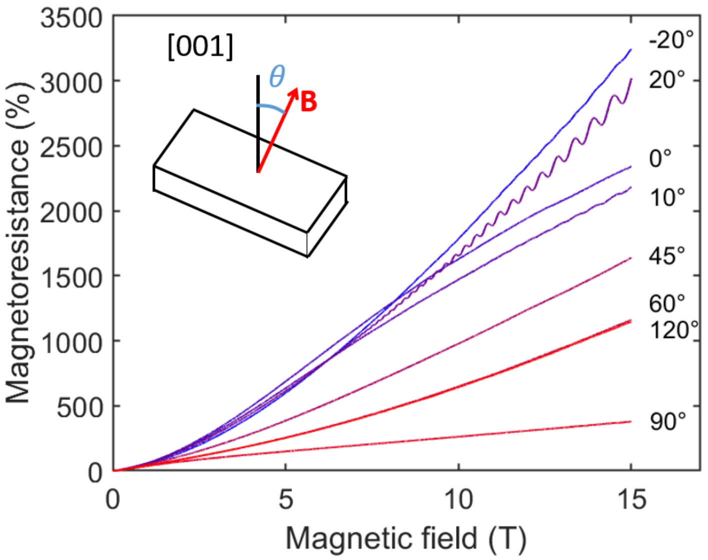

Figure 3.3: Magnetoresistance of MS1 for different tilting angles of the magnetic field (0° corresponding to the out-of-plane direction), measured at 5K. The curves at $\theta = 60°$ and $\theta = 120°$, which are symmetric tilting angles with respect to the sample's plane, are almost perfectly superimposed. Inset: Schematic of a sample, with definition of θ.

$\mathrm{MR}(B) = \dfrac{R(B) - R(B=0)}{R(B=0)}$, for different angles.

MS1 exhibits a colossal MR, with MR $> 2000\%$ for an out-of-plane field at 15T. However, an even higher MR can be reached when the field is tilted by approximately $\theta_{max} \sim \pm 20°$ in either direction, where it reaches $\sim 3000\%$. This behavior is consistent with the one reported by Gao et al. [2018], albeit with a lower maximal value of the MR. As we mentioned before, the difference in the amplitude of the MR can be attributed to a lower crystalline quality, as indicated by the five times larger RRR of their sample (640). This relation between the amplitude of the MR and the RRR is confirmed by the work of Xing et al. [2020], who measured a similar MR at $\theta = 0°$ (2200% at 14T, 2K) and a similar RRR (162) as for MS1.

The enhanced MR for a magnetic field tilted by $\theta_{max} = \pm 20°$ from the out-of-plane direction ($\theta \sim 30°$ for Gao et al. [2018]) might be related to the similar canted angle of the Fermi tubes formed by the γ pocket, at $\sim 20° - 30°$ [Jiang et al., 2020].

The angular dependence of the MR with the magnetic field is complex. We will therefore focus on three different characteristics of the MR here: its amplitude, its symmetry with respect to out-of-plane and in-plane directions, and the Shubnikov-de Hass oscillations (SdHo) measured for some angles.

Angular dependence of the magnetoresistance

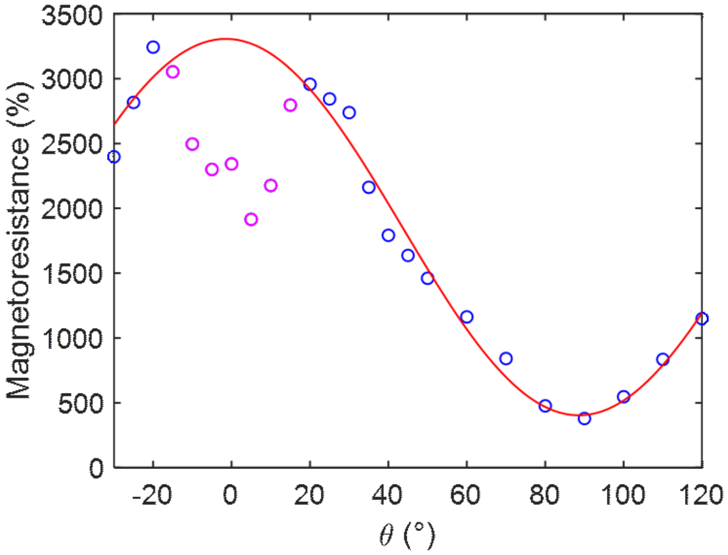

Figure 3.4: Magnetoresistance of MS1 at 5K and 15T for each angle, extracted from Fig.3.3, shown in blue and magenta. In order not to be influenced by the SdHo, the value of the MR at 15T was extrapolated from fourth-order polynomial background fits of the data. The sinusoidal fit, in red, was made by excluding the angles $-15° \leq \theta \leq 15°$, shown in magenta.

Since the MR under an out-of-plane magnetic field is much larger than under an in-plane field, we can expect, as a first approximation, the MR to follow a $\cos(\theta)$ dependence (like the out-of-plane component of the field), with a maximum for an out-of-plane field ($\theta = 0°$) and a minimum for an in-plane field ($\theta = 90°$). Instead, we find that, although the general behavior is that of a cosine, the MR at low temperature shows a local minimum around $\theta \sim 0°$ (see Fig.3.4). For these angles, the field dependence no longer corresponds to a simple power law, as it does for other angles. Instead, the MR at low angles shows an inflection point at low field, around $B \sim 2 - 3$T.

In order to study this in details, we computed for each angle θ the logarithmic derivative of the MR vs. field, $a(B) = \frac{\mathrm{d}log(\mathrm{MR})}{\mathrm{d}log(B)}$, which gives us the field dependence of the MR power law exponent. We find three different types of behavior,

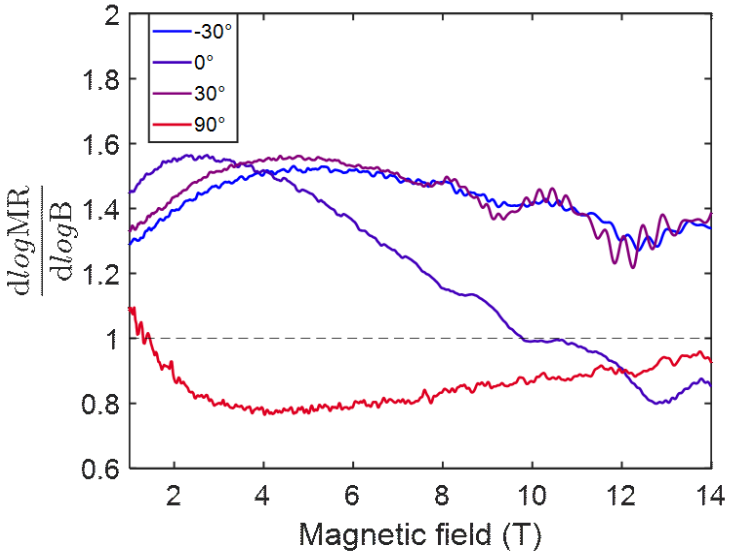

Figure 3.5: Logarithmic derivative of the Fig.3.3, shown for 4 specific angles, corresponding to 3 different qualitative responses in field. The resulting data was slightly smoothed to remove high frequency noise.

depending on the angle (see Fig.3.5): for angles away from the out-of-plane direction $\theta \in [-30°, -20°] \cup [20°, 60°]$, the exponent reached a maximum of $a \sim 1.5$ around 5T, followed by a small decay towards $a \sim 1.4$ at high field. This behavior is very similar for both positive and negative angular ranges. For low angles $\theta \in]-20°, 20°[$, the exponent reaches its maximum, with the same magnitude, at a lower field of about 3T and then decreases quickly. The power law even becomes sublinear above 14T for $\theta \in [-10°, 10°]$. This large reduction of the power law exponent is the reason for the large suppression of the MR around the out-of-plane direction. Around the in-plane direction ($\theta \sim 90°$), the power law is sub-linear. Interestingly, the power law shows no sign of saturation up to 14T.

The full angular dependence of the MR and its logarithmic derivative are shown in Fig.B.1a and Fig.B.1b respectively, which show a continuous evolution with the angle.

Symmetry of the magnetoresistance

Fig.3.3 and Fig.3.4 show another unexpected behavior: the MR is not symmetric around the out-of-plane direction. Even without taking into account the angles where it is suppressed, the MR is higher for $\theta = -20°$ than for $\theta = 20°$. This

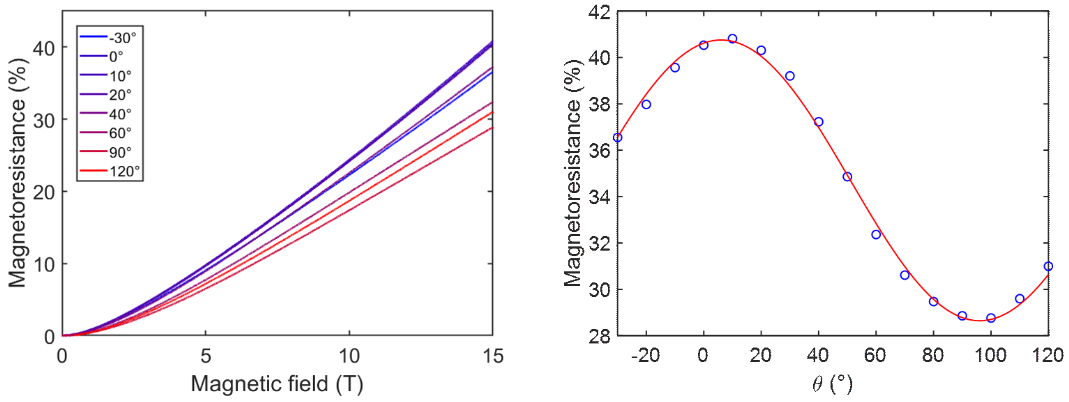

(a) (b)

Figure 3.6: (a) Magnetoresistance of a macro-structure for different tilting angles of the magnetic field (0° being the out-of-plane direction), measured at 50K. (b) Magnetoresistance at 15T for each angle, extracted from Fig.3.6a. A cosine fit is shown in red. The phase of the cosine was left as a free parameter, and is found to be offseted by 10.3°.

difference cannot be attributed to a misalignment of the sample in the superconducting coils, as the MR is symmetric around the in-plane direction $\theta = 90°$ (see e.g. $\theta = 60°$ and $\theta = 120°$ in Fig.3.3).

We repeated these measurements at higher temperature ($T = 50K$), where the MR is greatly reduced compared to at low temperature, as expected (40% vs. 3000% at 5K, see Fig.3.6a). The anisotropy of the magnetoresistance is much weaker at 50K such that the in-plane and out-of-plane MR are comparable (30% and 40% respectively). At this temperature, the angular dependence of the MR is very well fitted by a cosine law, with a $\theta_0 = 10.3°$ phase shift. Interestingly, there is no longer any suppression of the magnetoresistance around $\theta = 0°$ (out-of-plane direction, see Fig.3.6b). This is confirmed by the analysis of the power law exponent of the magnetoresistance, which is qualitatively the same at every angle (Fig.3.7): the exponent decreases with the field and shows a saturation at around 1.3 for $B > 8$T.

The comparison between the low- and high-temperature measurements shows that the origin of the colossal magnetoresistance is not related to the power law exponent, which can actually be higher at high temperature. However, the appearance of the magnetoresistance's suppression at low temperature suggests a quantum origin, although a more detailed temperature dependence of the suppression would be needed to get more insight into this origin.

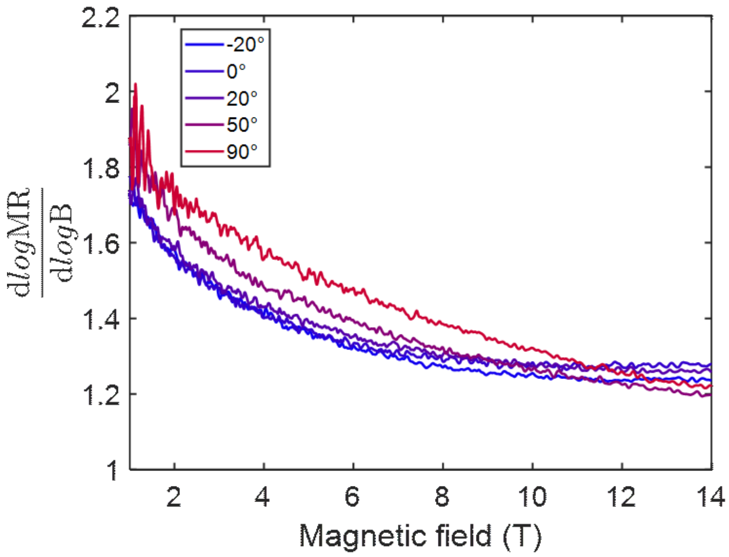

Figure 3.7: Logarithmic derivative of the data in Fig.3.6a, shown for 5 specific angles. The resulting data was slightly smoothed to remove high frequency noise. The response is qualitatively similar for every angle of the field.

Quantum oscillations

Schubnikhov de-Haas oscillations (SdHo) are measured at low temperature ($T = 5K$), for angles around $\theta = 10°$ (see Fig.3.3). In order to study them, we remove from the MR data a fourth-order polynomial background. The results are represented in Fig.3.8, where the fluctuation of the resistance are plotted as a function of 1/B. A detailed analysis, performed by varying FFT parameters and at different angles, shows independent contributions at three frequencies in the FFT spectrum, 38T, 350T and 1250T, and are associated with three carrier pockets, γ, α and β respectively (see Fig.3.9 and Veyrat et al. [2021]). This is in good agreement with the theoretical predictions from our band structure calculations (see Fig.3.10b). According to these calculations, the γ pocket associated with the low frequency oscillation is linked to the Weyl-node band (band 48 in blue, in Fig.3.10b), while the other pockets are associated with topologically trivial bands. Two additional pockets are expected to contribute to oscillations (band 49 and 50), albeit with much higher frequencies (above 3000T and 4000T respectively, see Fig.B.2) and were not identified experimentally.

The amplitude and frequency of the SdHo depend on the orientation of the magnetic field θ, as can be seen in Fig.3.10a: while the lowest frequency oscillations are always present for angles $|\theta| \leq 50°$ (emerging only weakly from the background

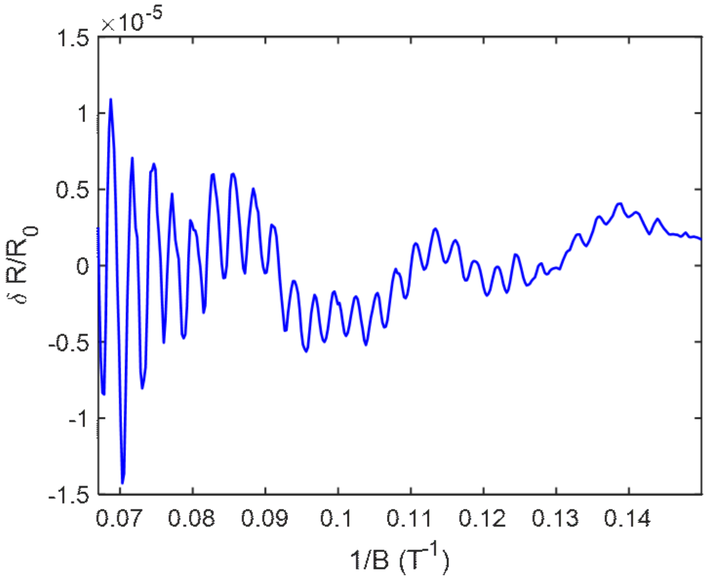

Figure 3.8: Schubnikhov de-Haas oscillations, measured for an angle $\theta = 10°$ at 5K. A fourth-order polynomial background was removed from the raw data. The oscillations are represented as a function of the inverse of the field, and show multiple frequency contributions.

of the spectrum for some specific angles), the oscillations associated with the α pocket only appear for $\theta \in [10°, 35°]$ and $\theta \leq -15°$ while those associated with the β pocket only appear for $\theta \in [-20°, 15°]$. When the oscillations are visible, their angular dependence at least partially agrees with band structure simulations (Fig.3.10b). The amplitude of the oscillations is not correlated to the magnitude of the magnetoresistance, as negative angles around $\theta = -15°$ show significantly smaller oscillations compared to their positive counterparts (see Fig.3.3), despite showing very similar magnetoresistances.

While the band structure simulations do not reproduce the experimental data exactly, they nonetheless reproduce its main features (similar frequencies and some of the angular dependence). Similar discrepancies between band structure simulations and experimental results have already been observed in this compound by Gao et al. [2018].

Effective mass

It is usually possible to extract from the temperature dependence of SdHo the effective mass of the electrons of the contributing band. For single-frequency SdHo,

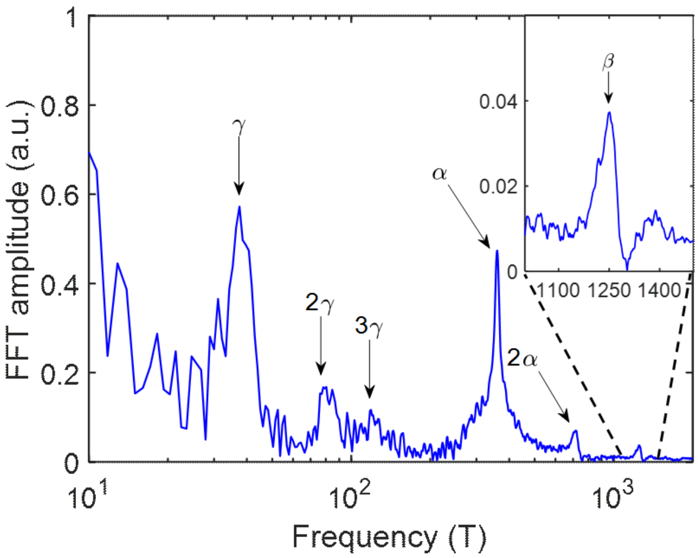

Figure 3.9: Fast Fourier Transform of the SdHo at $\theta = 10°$ (Fig.3.8), over the entire field range. Three peaks are clearly visible: α, at 38T, β at 350T and γ at 1250T. Given the wide range of frequencies, the data is shown in semilog scale. Inset:

this is done by measuring the temperature dependence of the amplitude of the oscillation at a given magnetic field, and fitting it with the Lifschitz-Kosewitz formula [Shoenberg, 1984]. This formula is only valid for a single-pocket contribution, but it can still be used when multiple bands contribute to oscillations if these contributions can be isolated from one another. For bands with different mobilities or effective mass, for instance, it can be possible to perform the analysis over a magnetic field range where only one pocket contributes. However, this does not appear to be the case in our sample. We therefore attempted to isolate each pocket by filtering out every frequency not related to the SdHO of the pocket that is under consideration, thanks to a bandpass around each oscillation frequency, and analysed the temperature dependence of the resulting oscillations. This didn't prove possible for the filtered γ and β pockets, as the filtered oscillations still show multifrequency features (see Fig.B.4.b and Fig.B.4.d). The filtered α pocket does show what appear to be single frequency oscillations (see Fig.B.4.c), however they cannot be analyzed properly with the LK formula (see Fig.B.5a and Fig.B.5b).

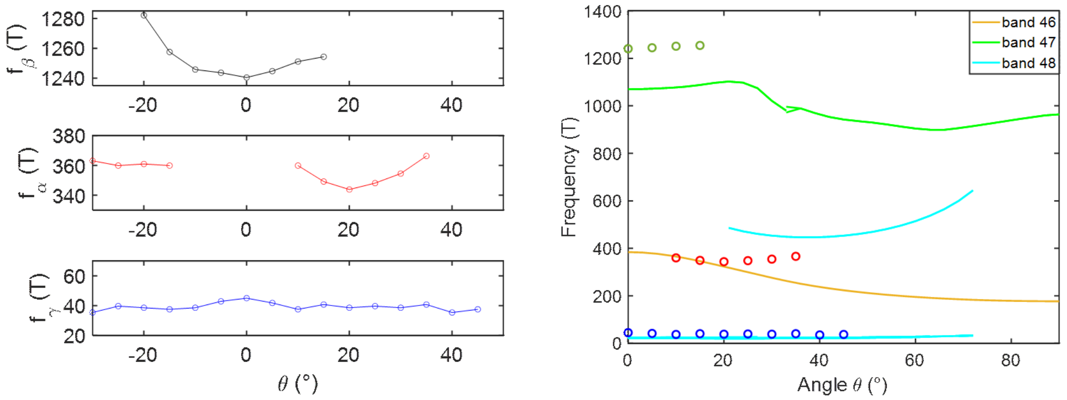

(a) (b)

Figure 3.10: (a) Angular dependence of the different SdHO peaks. Little dependence is found. Only the γ pockets shows a contribution to the SdHO at every angle studied. Missing points in the different graphs mean the absence of the corresponding frequency in the FFT. (b) Theoretical prediction of the SdHO frequencies from different bands, and their angular dependence. The frequencies found experimentally are indicated in red (α pocket), green (β pocket) and blue (γ pocket) circles. For some angles, band 48 (in cyan) presents several extremal orbits, which results in multiple oscillation frequencies expected from simulations.

3.3.2 Exfoliated structures

In addition to macro-crystals, we also measured 5 exfoliated structures in order to study the influence of quantum confinement on transport properties. Nanostructures allow us to make much more controlled experiments, with a better defined sample geometry (through e-Beam lithography) and higher signal-to-noise ratio. The exfoliated flakes we studied ranged in thickness from 41nm to 126nm. All exfoliated flakes were studied using a dilution fridge and a cryostat equipped with a 6T-2T-2T vector magnet.

Exfoliated samples typically show RRR values much lower than in bulk crystal. For exfoliated samples of tr-PtBi$_2$, we obtained RRR values between 1.3 and 15, with the highest being obtained for the thickest sample S5 (t = 126nm). In this section we present results for that sample, as all samples show qualitatively similar properties.

Similarly to macro structures, the resistance of S5 shows a linear dependence down to low temperature, where it saturates below $T < 15K$ (see Fig.3.11a). At 1K, S5 shows a much lower magnetoresistance than the macro-structure MS1, both for

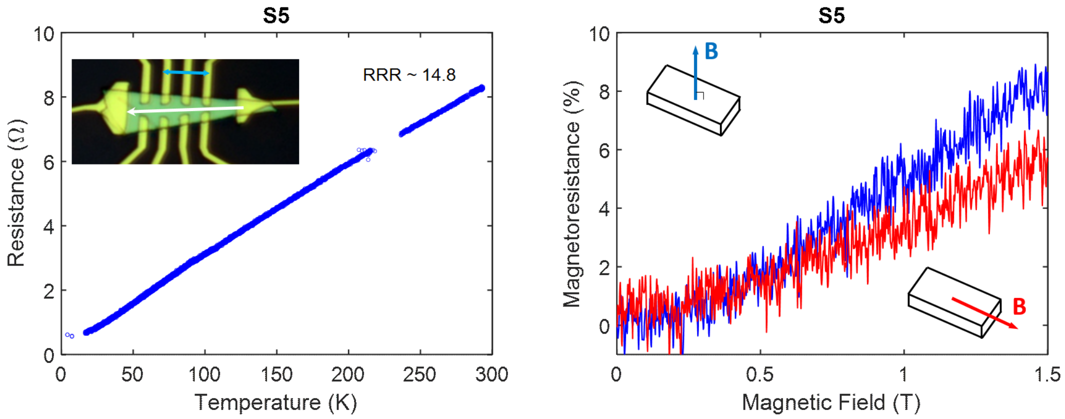

(a) (b)

Figure 3.11: (a) Cooldown of S5 from room temperature to 4K, yielding $RRR = 14.8$, indicating a good sample quality for exfoliated structures. Inset: Optical image of the structure, with the contact configuration measured. The current is applied along the white arrow, while the voltage is measured between the contacts marked by the blue double-arrow. (b) MR measured at $T \sim 1$K, for both in- and out-of-plane fields (respectively in red and blue), shown in percentage.

in- and out-of-plane fields (6% and 8% at 1.5T respectively, compared to 55% and 108% for MS1 at the same field and at 5K), as shown in Fig.3.11b. Contrarily to the macro-structure, no SdHo have been observed in any exfoliated structure, even at magnetic fields up to 6T. As for macro-structures, the magnetoresistance itself cannot be interpreted with a simple two-band model.

3.4 Planar Hall Effect in exfoliated structures

3.4.1 In-plane field mappings

When studying the response of exfoliated samples to in-plane fields at 1K, we noticed an angular dependence of the magnetoresistance: mappings of in-plane fields (see Fig.3.12) show an anisotropic, π-periodic variation of both the longitudinal and transverse resistances, giving two maxima and minima when doing a full rotation of the in-plane field. The extrema are shifted angularly by about $\pi/4$ between the two signals. This π-periodicity and $\pi/4$ shift between longitudinal and transverse signals are the hallmarks of the planar Hall effect (PHE, see sec.1.2). In this section, we discuss these preliminary results showing PHE and anomalous PHE in tr-PtBi$_2$.

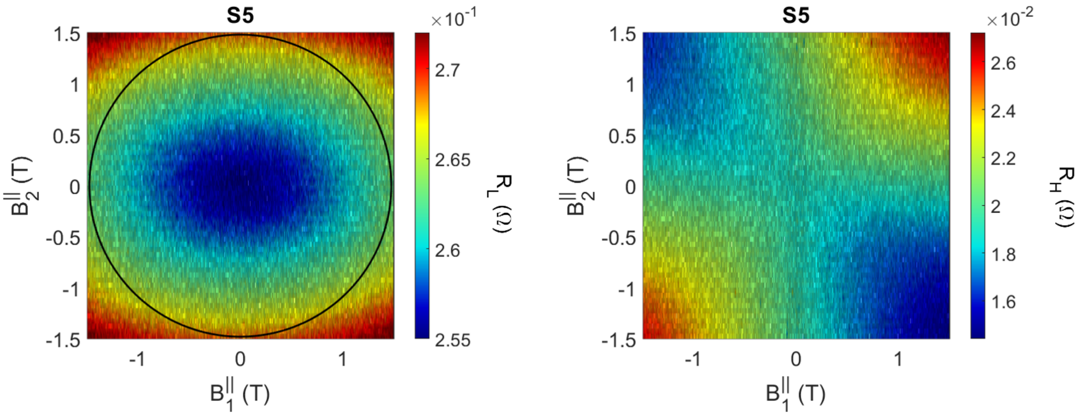

(a) (b)

Figure 3.12: In-plane magnetic field mappings of the longitudinal (a) and transverse (b) resistances (T = 1.1K and I_{AC} = 20μA), for sample S5, showing a π-periodicity when rotating the field. The contact configuration used is shown in Fig.3.13a. The black circle in (a) represents a constant in-plane field at B=1.5T.

To study the PHE in our system, we extracted the angular dependence of both signals at constant in-plane fields, ranging from 0.5T to 1.5T in steps of 20mT. Since our data points are not located along these circles but rather on a regular grid, we collected all points within ±10mT of the field we considered, in order to have a significant enough number of point to perform our analysis. The points collected this way are not evenly distributed, but are rather concentrated around certain angles. We then performed a consolidation of our data by averaging points closer than 0.1° together into a single point, before interpolating the result every 1° and smoothing it with a window of 20°. The angular dependence of S5 at 1.5T is represented in Fig.3.13b. The high frequency oscillations in both signals (especially visible in the longitudinal one) come from the analysis procedure, however it doesn't have a significant impact on our analysis as it has a relatively small amplitude and a much higher frequency in comparison to the effects we investigate in this study.

3.4.2 Data fitting

As we explained in section 1.2, the PHE is characterized by a π-periodic angular variation of the resistance in both the longitudinal and transverse configurations,

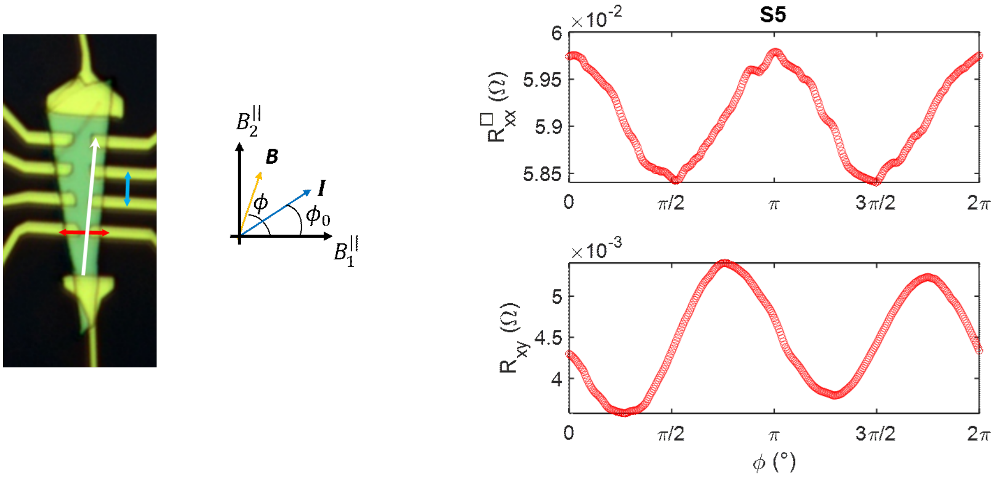

(a) (b)

Figure 3.13: (a) Left: Optical image of sample S5 showing the contact configuration used, with the current along the white arrow and the longitudinal and transverse resistances respectively between the blue and red double arrows. Right: schematic of the directions of the fields $B_1^{||}$ and $B_2^{||}$ with respect to the sample. The angle ϕ of the magnetic field is defined from $B_1^{||}$. The angle ϕ_0 implicated in the PHE signal (see text) represents the angle of the current, and is also defined from $B_1^{||}$. (b) Angular dependence of the longitudinal (top) and transverse (bottom) resistances of S5 for a constant in-plane field $B = 1.5$T (black circle in Fig.3.12a). Both signals are mainly π-periodic.

following

$$\begin{aligned} \rho_{xx}^{\text{PHE}}(B,\phi) &= \rho_{\perp}(B) - \Delta\rho(B)\, cos^2(\phi-\phi_0) \\ \rho_{xy}^{\text{PHE}}(B,\phi) &= -\Delta\rho(B)\, cos(\phi-\phi_0)\, sin(\phi-\phi_0), \end{aligned} \tag{3.1}$$

with $\Delta\rho = \rho_{\perp} - \rho_{||}$ ($\rho_{\perp}$ and $\rho_{||}$ are the magnetic field dependent resistivities of the sample when the in-plane field is respectively perpendicular and parallel to the current) and $\phi - \phi_0$ the angle between the field and the current (see Fig.3.13a). We fitted the angular dependences of the measured longitudinal and transverse resistivities at each field in order to show that the π-periodic oscillations share a common amplitude, and therefore confirm their PHE origin.

Multiple contributions

We have to take into account in our fitting procedure a certain number of effects which affect our measurements. First, the contacts on each side of the sample are not perfectly aligned with respect to the current, meaning that transverse contacts also measure a longitudinal component. The reverse is also true, but doesn't need to be taken into account because of the large difference in amplitude between the two signals. Second, the sample itself is not perfectly aligned in the magnetic field plane, which means that our system is also influenced by a small out-of-plane field which is 2π-periodic. This needs to be taken into account, as the out-of-plane MR is larger than the in-plane MR, and can result in a contribution of the out-of-plane field of up to 10% of the signal for a misalignment of a few degrees. Lastly, because we use invasive contacts on our structures we do not measure the entire transverse signal but rather only a fraction of it [Gluschke et al., 2020]. We correct for this effect by multiplying the transverse resistance with a geometric (field independent) factor. Once we have taken all these contributions into account, a significant 2π-periodic signal remains in the transverse measurements which cannot be explained by the out-of-plane field alone. We understand this contribution as being a Berry-phase induced Anomalous Planar Hall Effect (APHE) [Battilomo et al., 2021], as we will discuss later.

Fitting formula

When taking into account all the contributions mentioned above, we can express the longitudinal and transverse resistivities as

$$\begin{aligned}
\rho_{xx}(B,\phi) &= \mathrm{MR}^{\perp}_{xx}(B,\phi) + \rho^{\mathrm{PHE}}_{xx}(B,\phi) + \rho^{2\pi}_{xx}(B,\phi) \\
\rho_{xy}(B,\phi) &= \mathrm{MR}^{\perp}_{xy}(B,\phi) + C_H.\left(\rho^{\mathrm{PHE}}_{xy}(B,\phi) + \rho^{2\pi}_{xy}(B,\phi)\right) + C_L.\rho_{xx}(B,\phi),
\end{aligned} \tag{3.2}$$

where $\mathrm{MR}^{\perp}_{xx}(B,\phi)$ and $\mathrm{MR}^{\perp}_{xy}(B,\phi)$ represent the MR due to the misalignment-related out-of-plane field ; $\rho^{\mathrm{PHE}}_{xx}(B,\phi)$ and $\rho^{\mathrm{PHE}}_{xy}(B,\phi)$ represent the planar Hall effect contribution, as defined previously (eq.3.1) ; $\rho^{2\pi}_{xx}(B,\phi)$ and $\rho^{2\pi}_{xy}(B,\phi)$ represent a 2π-periodic, field-dependent contribution ; and C_H and C_L represent the geometric factor corrections to the transverse and longitudinal signals, and account respectively for the invasive transverse probes and the contacts misalignment.

To determine $\mathrm{MR}^{\perp}_{xx}(B,\phi)$ and $\mathrm{MR}^{\perp}_{xy}(B,\phi)$, we measured the longitudinal and transverse resistances for an out-of-plane field. As mentioned earlier, the contribution of the in-plane component due to the magnetic field misalignment can be neglected, as it amounts at most to about 5% of the signal. To account for the misalignment of the sample's contacts, we symmetrized and anti-symmetrized the results for $\mathrm{MR}^{\perp}_{xx}$ and $\mathrm{MR}^{\perp}_{xy}$ respectively, thus selecting only the longitudinal and transverse contribution from each signal, and we fitted the results with polynomials of order 4 (red lines in Fig.3.14). As we said above, the out-of-plane component of the field is 2π-periodic in ϕ, and will reach a maximum $B^{\perp}(\phi_{\perp}) = B.sin(\theta)$ for an

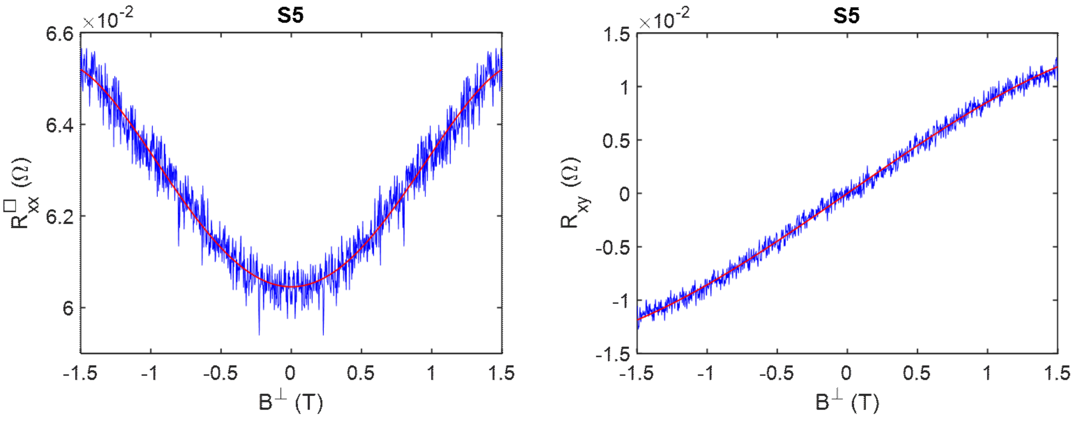

(a) (b)

Figure 3.14: Out-of-plane magnetic field dependence of the longitudinal (a) and transverse (b) resistances of S5 (in blue). The signals were fitted using 4th order polynomials (in red).

angle $\phi_\perp$, with θ the angle of the sample with respect to the field's plane. The out-of-plane field thus follows the angle dependence $B^\perp(\phi) = B.sin(\theta).cos\,(\phi - \phi_\perp)$, and we represent its magnetoresistance by

$$\mathrm{MR}_{xx}^\perp(B,\phi) = \mathrm{P4}_{xx}(B_\perp(\phi)), \tag{3.3}$$
$$\mathrm{MR}_{xy}^\perp(B,\phi) = \mathrm{P4}_{xy}(B_\perp(\phi)), \tag{3.4}$$

with $\mathrm{P4}_{xx}$ and $\mathrm{P4}_{xy}$ the 4th order polynomials shown in Fig.3.14. The longitudinal and transverse terms share a single free fit parameter, $\phi_\perp$. θ is fixed to the values extracted from the angular dependence of the superconducting critical field (see sec.4.11): $\theta = 5°$ for S3 and S4, and $\theta = 2°$ for S5.

We consider field-dependent 2π-periodic contributions for both longitudinal and transverse signals, with independent amplitudes, and a free phase parameter ϕ_1 independent of the PHE signal:

$$\rho_{xx}^{2\pi}(B,\phi) = A_{xx}^{2\pi}(B).cos(\phi - \phi_1), \tag{3.5}$$
$$\rho_{xy}^{2\pi}(B,\phi) = A_{xy}^{2\pi}(B).sin(\phi - \phi_1). \tag{3.6}$$

These contributions are distinct from the $\mathrm{MR}^\perp$ terms, which amplitudes are entirely determined by the magnetic field and the sample's misalignment angle.

Fitting procedure

There are two different types of parameters involved in the fit: parameters shared between the longitudinal and transverse resistances ($\rho_\perp(B)$, $\rho_{||}(B)$, ϕ_0, ϕ_1 and $\phi_\perp$), and parameters which only involve one signal ($A^{2\pi}_{xx}(B)$, $A^{2\pi}_{xy}(B)$, C_H and C_L). Some of these parameters also have an unknown field dependence. In order to determine all of these parameters in a single process, we fitted together both longitudinal and transverse data for each value of field between 0.5T and 1.5T (2×51 sets of data), all at the same time. Field-independent parameters were shared between every set of data, while field-dependent parameters where split into multiple independent parameters (one for each field).

Although the number of free parameters in this fit is large, their value can be determined reliably as they are all somewhat independent, with many parameters of different nature (amplitudes, phase offset etc.) and pertaining to signals of different periodicity.

3.4.3 Results

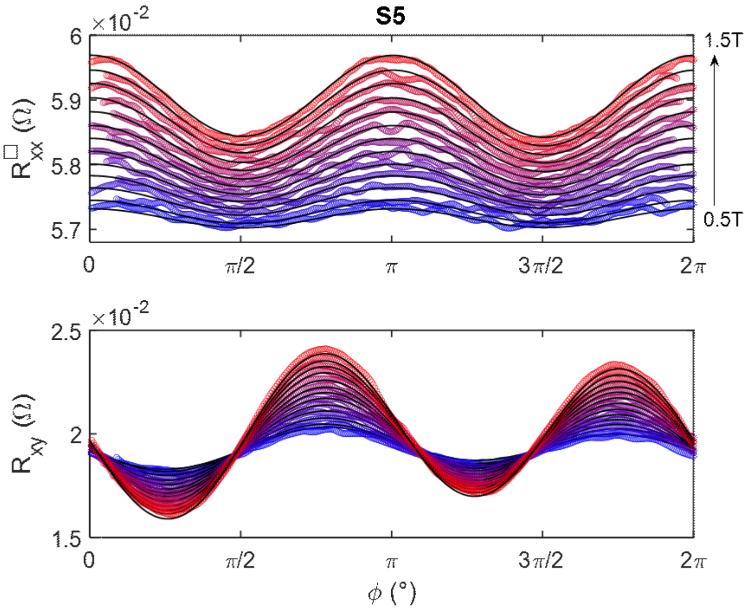

Figure 3.15: Angular dependence of the longitudinal per square (top) and transverse (bottom) resistances, for in plane fields from 0.5T (blue) to 1.5T (red), every 80mT. The fits (eq.3.2) are shown in black.

The fits we obtained, along with the measured angular dependences of the longitudinal and transverse resistances for S5, are plotted in Fig.3.15 for multiple fields from 0.5T to 1.5T (every 80mT). The longitudinal resistance is shown per square. The agreement between the data and the fits is excellent, and the latter yield $\phi_0 \sim 91°$ for the PHE phase, which is compatible with the orientation of the current in the structure, and $\phi_1 \sim -94°$ for the 2π-periodic signal. The fits also yield the longitudinal correction $C_L \sim -0.34$, and the transverse correction factor $C_H \sim 5.5$ obtained is of the order expected by Gluschke et al. [2020] for very intrusive transverse probes.

Planar Hall Effect

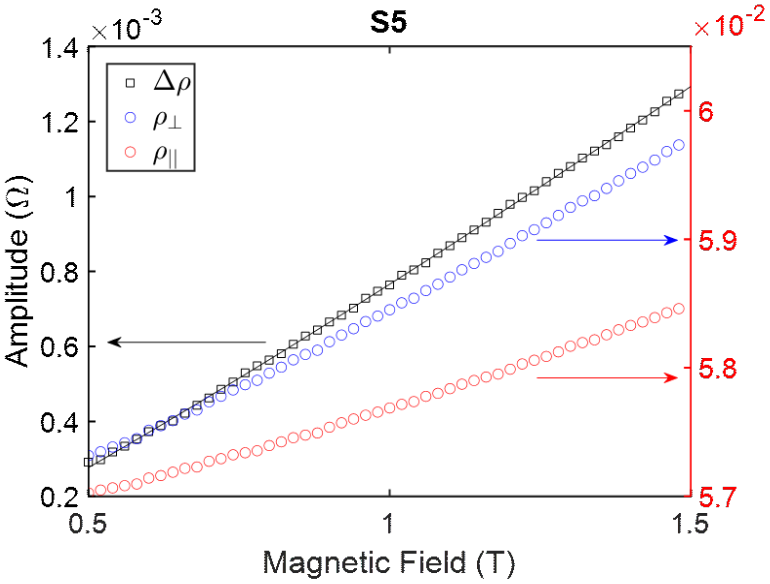

Figure 3.16: The field dependence of the PHE (π-periodic signal) amplitude $\Delta\rho = \rho_\perp - \rho_{||}$ is shown on the left axis (black squares). It is fitted with a power law $\Delta\rho \propto B^{1.15}$ (black line). The right axis shows the field dependence of its two components, $\rho_\perp$ and $\rho_{||}$ (in blue and red respectively).

We extracted from Fig.3.15 the field dependence of the parameters $\rho_\perp$ and $\rho_{||}$ (respectively blue and red circles in Fig.3.16). They both increase with the field, although $\rho_\perp$ increases faster than $\rho_{||}$. This difference leads to a non-zero amplitude $\Delta\rho = \rho_\perp - \rho_{||}$ of the PHE when the field increases (black squares in Fig.3.16). The field dependence of $\Delta\rho$ is well fitted with the power law $\Delta\rho \propto B^{1.15}$ (black line).

As we mentioned previously in sec.1.2, the PHE is a manifestation of an anisotropic response of the resistivity of a sample to in-plane magnetic fields, which can originate from magnetic ordering in ferromagnets [Nazmul et al., 2008], or from the chiral anomaly in Weyl and Dirac semi-metals [Burkov, 2017; Nandy et al., 2017; Kumar et al., 2018]. The amplitude is expected to depend quadratically on the magnetic field in type-I Weyl semi-metals [Burkov, 2017], while in type-II Weyl semi-metals, when the current and the magnetic field are applied in the tilting direction the the cones, the amplitude of the PHE is expected to depend linearly on the magnetic field [Nandy et al., 2017].

We can rule out ferromagnetism as the origin of the PHE in our system, since tr-$\mathrm{PtBi_2}$ is a non-magnetic material. The quasi-linear field dependence of the PHE amplitude in our sample, as well as the increase with field of both $\rho_\perp$ and $\rho_{||}$, does not correspond to the model of Burkov [2017] for type-I Weyl semi-metals, which predicts $\Delta\rho \propto B^2$, a constant $\rho_\perp$ and a decreasing $\rho_{||}$ with magnetic field. However, this model only looked at the contribution of the chiral anomaly to the magnetoresistance, and Li et al. [2019] have discussed the fact that a strong orbital magnetoresistance can hide the effects of the chiral anomaly, and sub-quadratic field dependences have been reported in some topological metals [Singha et al., 2018]. Therefore, the non-trivial origin of the PHE cannot be excluded and further additional experiments are planned, both at higher magnetic fields (to determine precisely the field dependence of the effect), as well as by varying the temperature (to get more information on its origin).

Anomalous planar Hall Effect

The field dependences of the 2π-periodic signals are represented for both transverse and longitudinal resistances in Fig.3.17. As we expected from Fig.3.15, the longitudinal resistance (in blue) does not show any 2π-periodic signal. The transverse resistance (in red) however shows a significant 2π-periodic signal, with about 15% of the PHE amplitude, and varies linearly with magnetic field (red line). Battilomo et al. [2021] proposed a theoretical explanation for such an effect in two-dimensional *trigonal* systems. They show that the crystal symmetries (i.e. lack of C_2 rotational symmetry), along with a strong spin-orbit coupling, allow for a non-vanishing Zeeman splitting-induced Berry curvature, which results in a $2\pi/3$-periodic contribution to the transverse resistivity with a linear field dependence at low fields. Importantly, this effect does not contribute to the longitudinal resistivity, and can coexist with the regular PHE. In the presence of symmetry-lowering defects (e.g. crystalline domains or stacking faults between the van der Waals layers), the C_3 rotation symmetry may be broken, which would result in an increase of the period of the APHE contribution to 2π, as we measured. Further

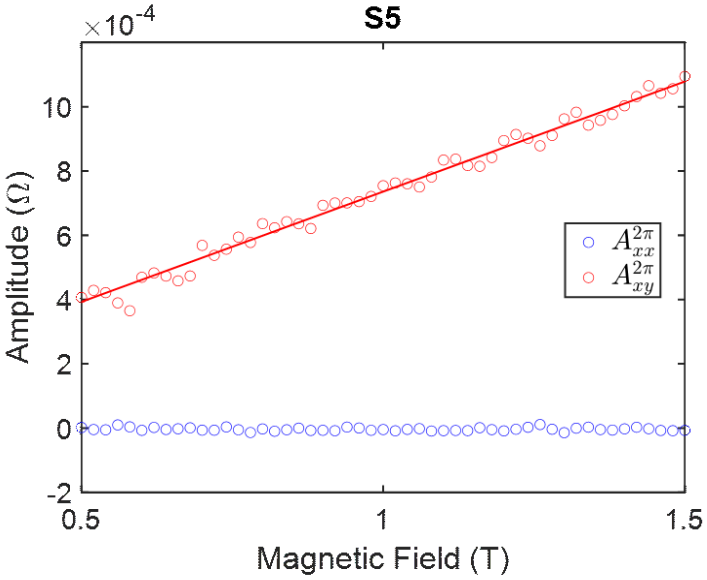

Figure 3.17: Field dependence of the amplitude of the 2π-periodic signals of the longitudinal and transverse resistances, respectively in blue and red circles. The amplitude of the former stays constant with field, at zero, while for the latter it increases linearly with field (red line).

characterization in temperature and at higher field is needed to study this effect further, and will be performed in the near future.

3.4.4 Other samples

We have conducted the same study in two other samples, S3 and S4, which showed similar effects. Our overall conclusions are the same, as we can see for S3 in Fig.3.18b: The longitudinal and transverse resistances both show π-periodic and 2π-periodic signals increasing with magnetic field, and which are well fitted with our model, which yields $\phi_0 \sim 183°$, $\phi_1 \sim 287°$, $C_H \sim 1.98$ and $C_L \sim 0.15$. The difference in the values of ϕ_0 between S3 and S5 is consistent with the physical angle between the current lines in the two flakes, which is about 90° (see Fig.3.18a). There are some differences between the samples however. First, the longitudinal and transverse resistances of S3 (and S4) are not fitted perfect by our model anymore, as a slight angular shift can be seen in the longitudinal resistance between the fits (black line in Fig.3.18b) and the data. This is due to the fact that the transverse and longitudinal resistances are shifted by slightly less than $\pi/4$ in these samples, while the theoretically expected shift is exactly $\pi/4$ in the PHE. Also,

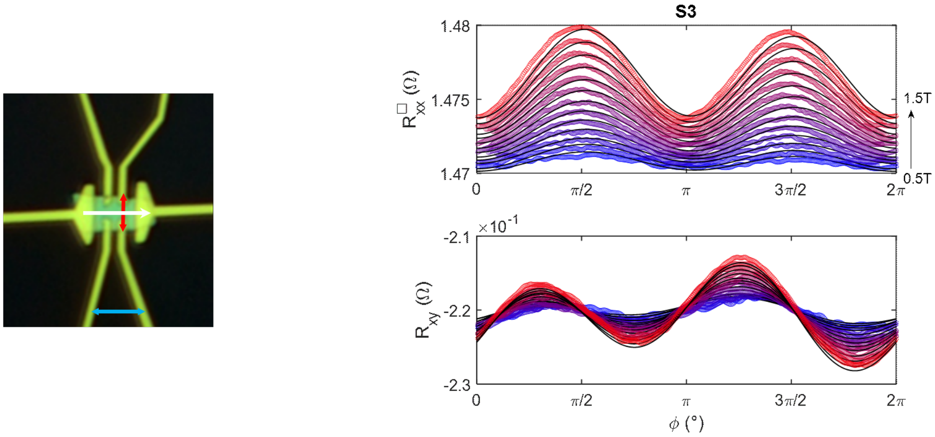

(a) (b)

Figure 3.18: (a) Optical image of sample S3 showing the contact configuration used, with the current along the white arrow and the longitudinal and transverse resistances respectively between the blue and red double arrows. (b) Angular dependence of the longitudinal (top) and transverse (bottom) resistances for in-plane fields from 0.5T (blue) to 1.5T (red), every 80mT. The fits of the data using eq.3.2 are shown in black.

the amplitude of the PHE in S3 follows the power law $\Delta\rho \propto B^{1.87}$ (see Fig.B.6a), very close to a quadratic field-dependence, while S5 shows a quasi-linear field-dependence.

Remarkably, the 2π-periodic signal in the transverse resistance shows the same linear field-dependence in S3 as in S5 (see Fig.B.6b), which indicates that this effect is not linked to the PHE.

3.4.5 Discussion

Our preliminary results show the existence of a π-periodic planar Hall effect in thin exfoliated structures of tr-PtBi$_2$, and was confirmed in three different samples for thicknesses ranging from 41nm (S3) to 126nm (S5). We also measured an additional 2π-periodic signal in the transverse resistance, which we interpret as an anomalous PHE. These results were also confirmed at lower AC current for all three samples (although with lower signal-to-noise ratios). Neither π- nor 2π-periodic signals show a dependence in current.

Although the APHE model of Battilomo et al. [2021] was developed for strictly 2D trigonal systems, the symmetry arguments used, and their conclusion, should remain valid in the intermediate case of thin nano-structures. The strongest argument in favor of this model is the very linear magnetic field dependence of the signal, which is quite uncommon, as well as its manifestation exclusively in the transverse resistivity, instead of both longitudinal and transverse resistivities (which is case for the PHE). As we mentioned earlier, stacking faults between the van der Waals planes could destroy the C_3 symmetry of the crystal structure, and explain the 2π periodicity of the transverse signal instead of the $2\pi/3$-periodicity expected in the original model. We should be able to test this hypothesis by repeating these measurements at higher fields: following Battilomo et al. [2021], if the C_3 symmetry is not broken in the system we should see a $2\pi/3$-periodic signal emerge in the transverse resistance at high-enough field, which would invalidate our hypothesis. A study at higher field would also allow for a more precise determination of the π-periodic signal's field dependence. We are therefore planning a new study using a mechanical rotator to rotate the sample in a constant field up to 14T, in order to gain more insight into the origin of both π- and 2π-periodic signals.

4 Superconductivity in trigonal-PtBi$_2$

In this chapter, we report on the superconducting transition of both macro- and nano-structures of trigonal-PtBi$_2$ (tr-PtBi$_2$) at very low temperature. We begin with the definition of critical parameters used throughout this chapter, before presenting our results of superconductivity in macro-structures and nano-structures.

4.1 Critical parameters

When characterizing the superconductivity in our samples, we choose to define the critical parameters T_c, B_c and I_c as the values at which the resistance R reaches half of the normal resistance R_N, e.g. $R(T_c) = R_N/2$ (the critical current also corresponds to the peak of differential resistance dV/dI, see Fig.4.1a). This definition has the advantage of being simple, effective, and is used widely by the transport community [Fatemi et al., 2018]. Determining the normal resistance is not straightforward however.

For most contact configurations, R_N is defined as the value of the differential resistance dV/dI at very large DC current. This works well for configurations in which the differential resistance is constant at high current (see Fig.4.1a). This definition is coherent with field and temperature measurements (see Fig.4.1b and Fig.4.1c), and is used for most of the contact configurations.

For some contact configurations however, the differential resistance does not reach its constant value at the highest current measured ($I_{DC} = 75\mu$A, see Fig.4.2a), or dV/dI measurements where not possible (macro-structures). Since the resistance is also not constant at the highest temperature measured ($T = 600$mK, see

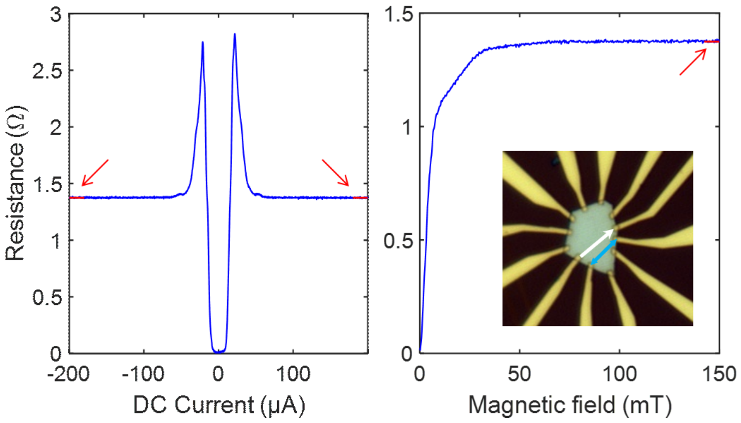

(a) (b) (c)

Figure 4.1: Differential resistance dV/dI (a) and resistance dependence with magnetic field (b) and temperature (c), in blue, in nano-structure S1. The normal resistance R_N is defined as the average of the differential resistance at high current (red line in (a)). This value is reported in (b) and (c), also as a red line, and is indicated by red arrows. (b) Inset: optical image of S1 with the contact configuration used (current along the white arrow, voltage along the blue double arrow).

Fig.4.2c), we defined the normal resistance for these configurations from magnetic field measurements. However, at large fields the resistance is not constant, but slowly increases with field (see Fig.4.2b, above 600mT). The normal resistance was therefore defined as the average of the resistance at fields corresponding to after the end of the superconducting transition and before the magnetoresistance becomes significant.

4.2 Superconductivity in Macro-structures

In order to study the superconducting properties of tr-$PtBi_2$ in macroscopic samples at very low temperatures we contacted three additional macro-structures (MS2, MS3 and MS4) using the same method as for MS1. MS2 was grown as pure $PtBi_2$, while MS3 and MS4 were grown with different Rhodium dopings, although MS3 is practically pure (3% doping) and behaves similarly to the undoped sample. All structures have shown a superconducting transition at low temperature. In this section, we will focus on the undoped case sample MS2.

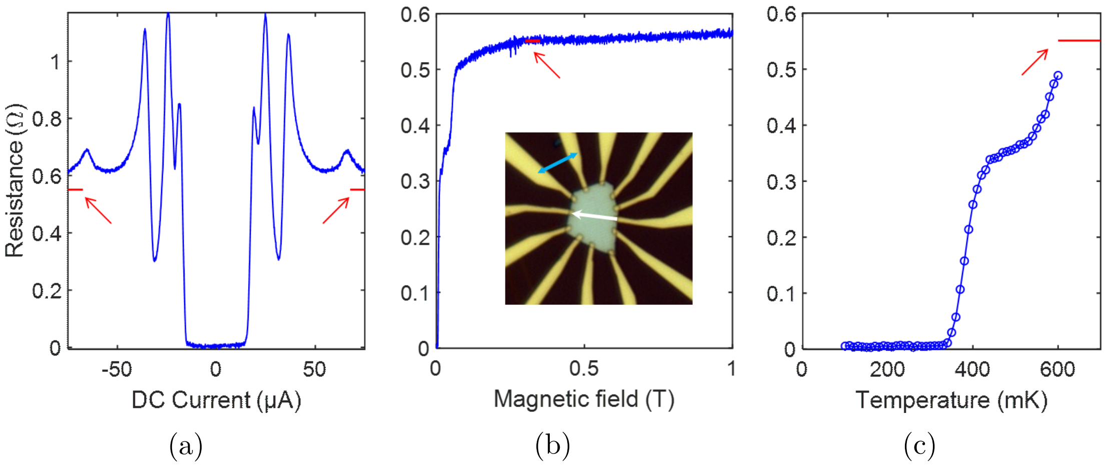

Figure 4.2: Differential resistance dV/dI (a) and resistance dependence with magnetic field (b) and temperature (c), in blue, in nano-structure S1, for a different configuration. The normal resistance R_N is defined as the average resistance between 300-350mT (red line in (b)). This value is reported in (a) and (c), also as a red line, and is indicated by red arrows. (b) Inset: optical image of S1 with the contact configuration used (current along the white arrow, voltage along the blue double arrow).

4.2.1 3D superconductivity

We cooled MS2 down to $T \sim 100$mK using a dilution fridge. It shows a high crystalline quality: the resistance decreases with temperature down to about 15K, where it starts saturating, showing a RRR of 98 (see Fig.4.3). When cooled down further, the resistance stays constant until about 800mK, where it starts to decrease towards zero, suggesting a superconducting transition around $T_c \sim 600$mK, as we first reported in Shipunov et al. [2020].

The zero resistance state is destroyed by magnetic fields, as can be seen for an in-plane field in Fig.4.4, with a critical field $B_c = 50$mT. We note that the zero-resistance state is slightly shifted with respect to $B = 0$T due to remanent fields. Remanent fields in our system are no more than a few mT at most, but the high sensitivity of the superconductivity to magnetic fields implies that transport properties can be significantly influenced by such fields.

Interestingly, point-contact measurements show an enhancement of the superconductivity (i.e. of B_c and T_c), probably linked to increased local pressure (see sec.C.1.2 and [Veyrat et al., 2021]).

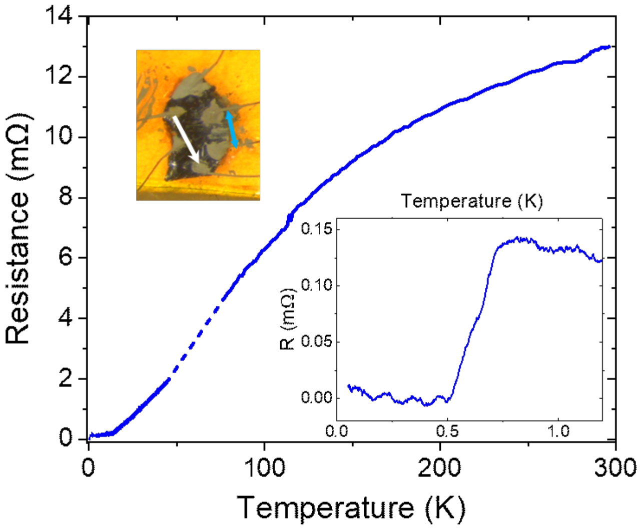

Figure 4.3: Temperature dependence of the resistance of MS2 between room temperature and the base temperature of our dilution fridge ($T \sim 100$mK), giving a residual resistivity ratio of 98. The dashed line corresponds to missing points due to measurements errors. Inset left: Optical picture of MS2, with the current flowing along the white arrow, and the voltage measured along between the contacts shown by the blue double-arrow. Inset right: Zoom-in below 1K, showing a superconducting transition of the sample around $T_c \sim 600$mK.

Magnetic field anisotropies

Even though the superconductivity does not show any significant magnetic field anisotropy when sweeping the field along the out-of-plane direction and the two in-plane directions (Fig.4.5), weak anisotropies are revealed by complete field mapping (Fig. 4.6). These anisotropies are small however (~ 1.4 between the plane and out-of-plane directions, and ~ 2 in the plane) which indicates three-dimensional superconductivity rather than a layered superconductivity, for which one would expect a much larger anisotropy [Devarakonda et al., 2020].

Critical field versus temperature

To further study the superconducting phase in macro-structures, we measured the temperature dependence of the in-plane critical magnetic field. To this purpose, we measured a series of magnetic field sweeps, from 0T to 500mT and back, at

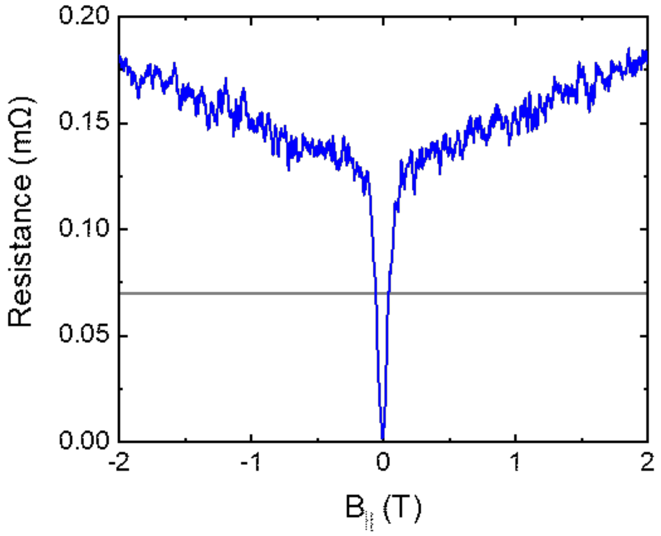

Figure 4.4: Magnetic field response of MS2 for an in-plane field, showing a superconducting transition below $B_c \sim 50$mT. The horizontal line corresponds to $R = R_N/2$, with R_N the resistance in the normal state. The intersection between this line and the data gives the critical magnetic field.

different temperatures ranging from 150mK (well bellow T_c) to 750mK (above T_c). From this, we could determine the critical magnetic field at different temperatures. The temperature dependence of the critical field is shown in Fig.4.7, and the full data in Fig.C.1. The temperature dependence of the critical field is well described by the Ginzburg-Landau (GL) theory at 3D (see eq.1.3), with a linear dependence down to $T = 250$mK. The value of the superconducting coherence length at zero-temperature given by this model is $\xi_0 \sim 60$nm. The same results are obtained for the forward and backward sweeps. This result shows that superconductivity in tr-PtBi$_2$ macro-structures is more three-dimensional than layered or surface-held: if this were the case, the Ginzburg-Landau theory predicts that the in-plane critical field would not depend linearly on the magnetic field (see eq.1.4 and eq.1.5).

To study the nature of the superconductivity in macro-structures, specific heat as well as SQUID measurements were performed, but they did not give any signature typical of superconductivity, which could indicate that the superconducting state in macro-structures is percolative. Nonetheless, the large superconducting coherence length obtained from charge transport measurements suggests that it could be possible to observe superconductivity of reduced-dimension in thin exfoliated samples.

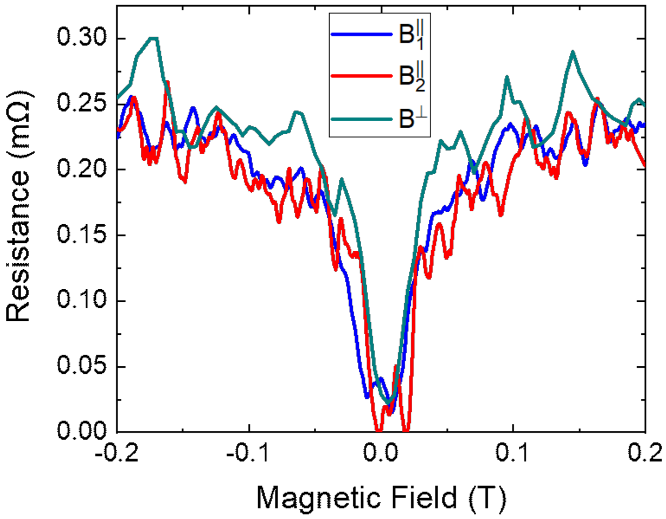

Figure 4.5: Magnetic field response of MS3 for different directions of the field, showing an isotropic behavior. $B^{\perp}$ (green) was extracted from a 2-dimensional mapping in field.

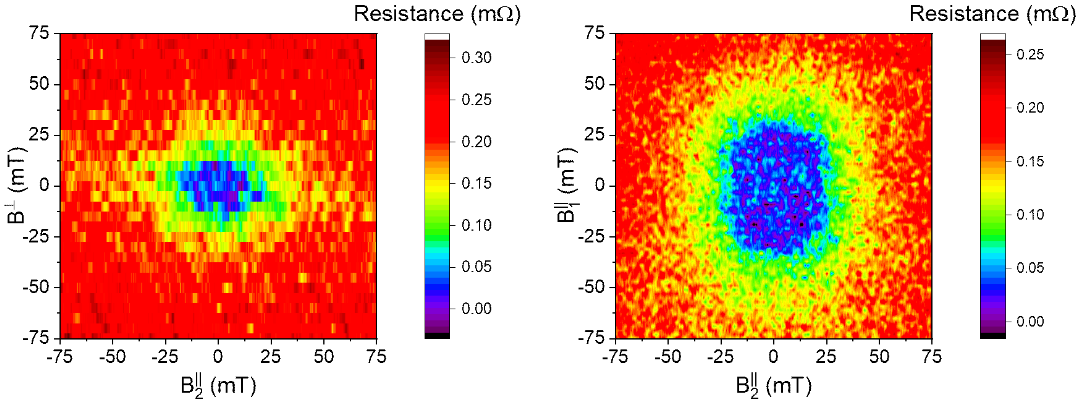

(a)

(b)

Figure 4.6: Field mappings of the resistance of MS3, between the sample plane and the out-of-plane direction (a), and between the two in-plane directions (b).

4.3 Superconductivity in exfoliated structures

As mentioned previously, the large coherence length of the superconductivity found in macro-structures coupled to the van der Waals nature of the material make it

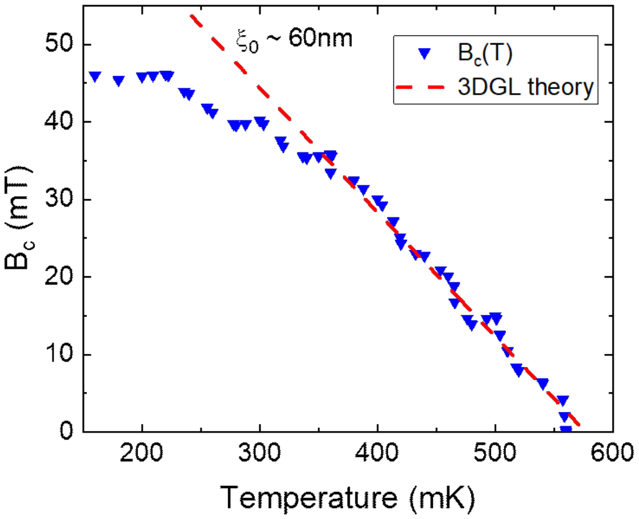

Figure 4.7: In-plane critical magnetic field of MS2 as a function of the temperature, extracted from the contour in Fig.C.1 (blue triangles). Close to T_c, the data is well fitted by the 3D Ginzburg-Landau theory (red dashed-line), and yields a coherence length $\xi_0 = 60\text{nm}$.

possible to study confined superconductivity in thin exfoliated structures of tr-PtBi$_2$, with thicknesses lower or comparable to the superconducting length. As stated before in sec.3.3.2, we studied 5 exfoliated structures in total. In this section, we will focus on presenting results for one particular structure, S1 (the first exfoliated structure we measured), and for the particular contact configuration V0 shown in the inset of Fig.4.8. The main results presented in the next two subsections are currently posted on arXiv [Veyrat et al., 2021].

4.3.1 Characterization of the superconductivity

Sample S1 is 60 nm thick for about 10 µm in width. It shows a good crystalline quality, with a RRR of 9. When cooled down to sub-kelvin temperatures, the sample showed a slightly broad superconducting transition around $T_c = 350\text{mK}$ (Fig.4.8, in red), much lower than for macro-structures. We will discuss this figure in more details shortly.

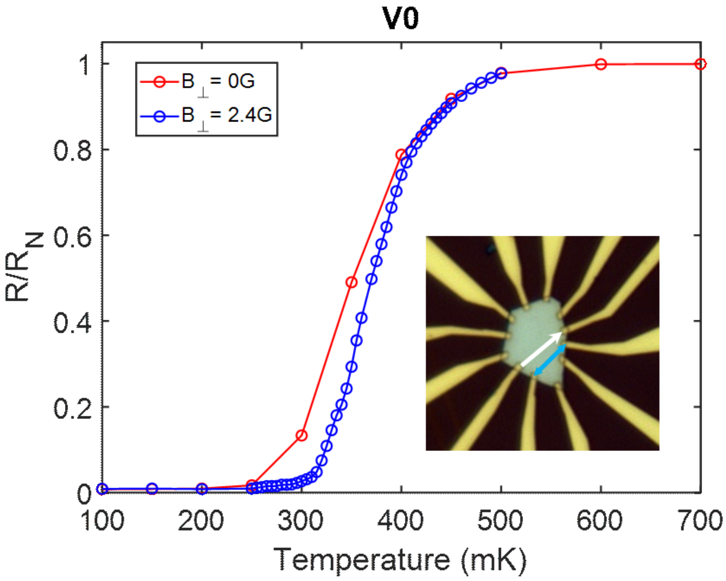

Figure 4.8: Reduced resistance as a function of the temperature (in red), showing a superconducting transition at $T \sim 350$mK. Applying a small out-of-plane magnetic field of 2.4G, to compensate for the remanent field, improves the transition to $T_c = 370$mK (in blue). Both data were extracted from the zero-current data of differential resistance mappings in temperature and current (see Fig.C.6 for the mapping at $B = 2.4$G). Inset: Optical image of the structure, with the contact configuration measured. The current is applied along the white arrow, while the voltage is measured between the contacts marked by the blue double-arrow.

Current and field response

To further characterize the superconducting state, we measured the differential resistance of the sample (see Fig.4.9a) by applying a DC current in addition to the AC polarization current (see sec.2.1.2). The zero resistance state persists until the DC current reaches $I^0_{DC} = 10\mu$A, for an AC current $I_{AC} = 1\mu$A. We find a critical current $I_c \sim 22\mu$A (defined as the current for which the differential resistance reaches its maximum). Therefore, since our AC polarization current of 1μA is one order of magnitude lower than I^0_{DC}, it will not influence significantly the superconductivity in our AC resistance measurements (without DC current). We find this AC current to be a good compromise to measure at-equilibrium properties while maintaining the highest signal-to-noise ratio possible.

We then focused on the response of the sample to an external magnetic field. We find the critical magnetic field to be $B_c^{||} \sim 143$mT for an in-plane field, and $B_c^{\perp} \sim 6$mT for an out-of-plane field. While the in-plane critical field is significantly higher

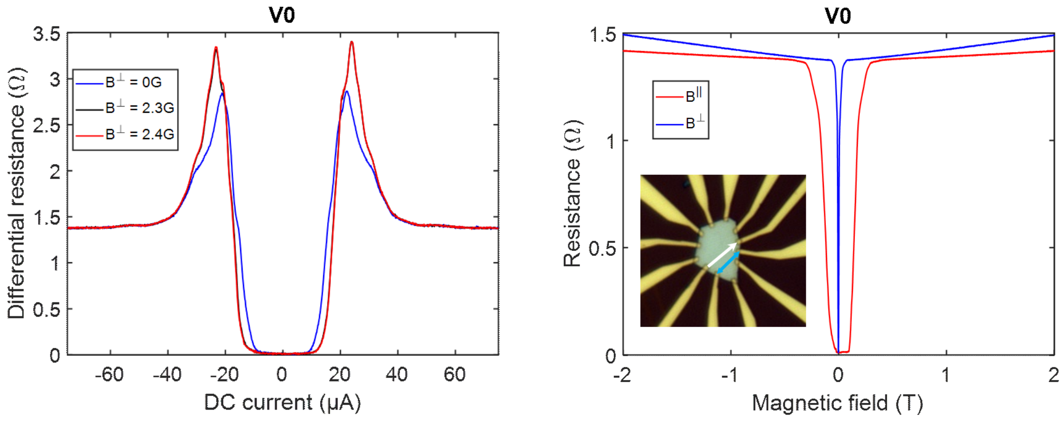

(a) (b)

Figure 4.9: (a) Differential resistance measured at different (out-of-plane) magnetic fields, in order to compensate for the remanent field. (b) Magnetic field dependence of the resistance, for both in- and out-of-plane fields (respectively in red and blue). A clear anisotropy can be seen, with $B_c^{||} \sim 143$mT and $B_c^{\perp} \sim 6$mT.

than for macro-structures, the out-of-plane field is greatly reduced. This leads to a high anisotropy in the field response, with a critical field ratio of $B_c^{||}/B_c^{\perp} \sim 25$ (Fig.4.9b), compared to a rather isotropic response in macro-structures. When the sample's misalignment is taken into account, this ratio reaches 55 (see sec.4.3.2). Such a large difference is a direct consequence of the reduced dimensionality of the superconductivity in this sample.

Remanent field and reset procedure

The effects of remanent fields are visible for exfoliated structures under out-of-plane magnetic field, with the effective zero field state being shifted to the negative fields for a sweep from positive to negative fields and vice versa. In Fig.4.9b (blue curve), the center of the transition is at $B^{\perp} \sim -3$mT for a sweep from positive to negative fields. Remanent fields are not as visible for in-plane fields, due to a strong asymmetry in the field transition (a small one also exists for an out-of-plane field), as can be seen in Fig.4.9b (red curve). We have studied this effect in different samples, and understand it as metastabilities in the superconducting state. However, this study goes well beyond the scope of this manuscript, and we will therefore not include it here. In practice, we can avoid most measurement issues related to metastabilities by always increasing the magnitude of in-plane fields (e.g. sweeping from 0 to positive or negative fields), and by applying a "reset" procedure (see below) when decreasing them.

Since a few millitesla of out-of-plane field can be enough to greatly influence the superconductivity in our samples, we developed an empirical "reset" procedure to minimize both the out-of-plane remanent field and the effect of metastabilities. The superconductivity being less sensitive to in-plane remanent fields for S1, we did not need to develop a similar procedure for them. We note nonetheless that, for other exfoliated structures, a similar procedure along an in-plane direction must be applied to remove the effects of metastabilities.

The "reset" procedure we developed for S1 consists in sweeping the out-of-plane field around zero, back and forth with decreasing amplitude, before setting it at zero: $B^{\perp} = 0T \rightarrow 1T \rightarrow -0.5T \rightarrow 0.2T \rightarrow$ 0T. We found this procedure to be very efficient in avoiding any remanent fields and metastabilities.

Due to the high sensitivity of the superconductivity to the out-of-plane magnetic field, we could measure precisely the remaining out-of-plane remanent field to be -2.4G (see Fig.4.9a) by comparing the differential resistance of the sample at different small applied fields (in attempted compensation of the remanent field): The remanent field is compensated when the peaks on either side of the zero-resistance plateau are maximized. This is the most accurate method we found to compensate the remanent field, and is as sensitive as a fraction of Gauss (see Fig.4.9a).

Temperature dependence R(T) with remanent field compensation

Since the remanent field has a significant impact on the superconducting state, we compensated for it by applying an out-of-plane field $B^{\perp} = 2.4$G and measured the temperature dependence of the resistance R(T) again. Because of the long stabilization time of the dilution fridge, the temperature dependence was not obtained by varying the temperature continuously (with all other parameters staying constant), but were rather extracted from a series of differential resistance measurement done at constant temperatures (see Fig.C.6): The resistance at each temperature was taken as the zero-DC-current value of the differential resistance (to reduce the noise of the measurement, we averaged the zero-current value over a 1μA range centered around zero).

With the remanent field compensated for, we see an improvement of the superconducting critical temperature to $T_c = 370$mK (a 20mK improvement compared to the T_c obtained without compensation), as well as a sharper transition (see Fig.4.8, in blue).

Different contact configurations

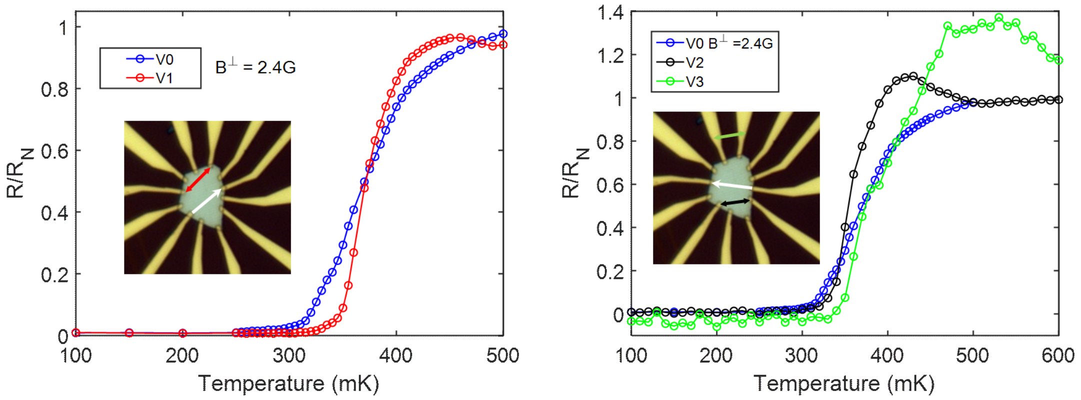

(a) (b)

Figure 4.10: Temperature dependence of the resistance for contact configuration V1 (a), and V2 and V3 (b), see insets. For V1, an out-of-plane field of $B^{\perp} = 2.4$G is applied to compensate for the remanent field. Configuration V0 is shown in blue, for comparison

Thanks to its contact geometry, we were able to measure S1 in different contact configurations, varying both the current orientation and the voltage probes. By comparing these results, we can gain insight into the inhomogeneities in the sample. When keeping the same source and drain as for the previous configuration (V0) and measuring the voltage on the other side of the structure (configuration V1), we find a slightly different superconducting transition (see Fig.4.10a): Even though $R(T) = R_N/2$ is reached for a very similar $T_c = 371$mK than for V0, the shape of the transition differs, with a peak of resistance at $T \sim 450$mK, just above T_c.

A behavior similar to V1 was also observed for two other configurations (V2 and V3) with different drain, source and voltage probes (see Fig.4.10a), with a resistance peak, for $T \gtrsim T_c$, and we find respectively $T_c^{V2} = 354$mK and $T_c^{V3} = 374$mK, close to the values measured in the previous configuration. We will discuss the origin of these peaks in section 4.3.4.

4.3.2 Dimensionality of the superconductivity

Angular dependence of the critical field

In order to study the dimensionality of the superconductivity in thin exfoliated

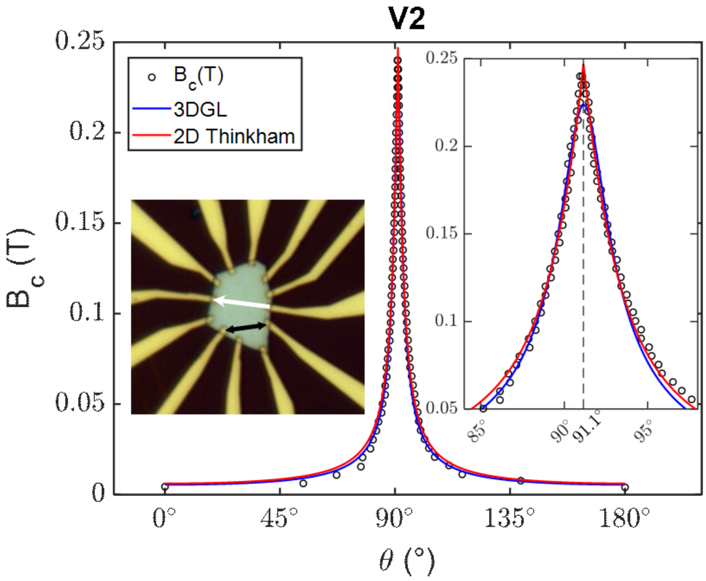

Figure 4.11: Angular dependence of the critical magnetic field for V2, with $\theta = 0°$ corresponding to an out-of-plane field. This data was extracted from Fig.C.4a, and was fitted with the 3D Ginzburg-Landau model (in blue), and the 2D Thinkham model (in red). Inset: Zoom-in on the peak, which is centered around $\theta = 91.1°$, due to a physical misalignment of the sample.

samples, we measured the angular dependence of the critical magnetic field. As we have shown in sec.1.3.4, a difference is expected in the critical field's angular dependence $B_c(\theta)$ depending on the dimensionality of the superconductivity: In contrast to 3D superconductivity, 2D superconductivity is expected to show a cusp-like peak of the critical field for an in-plane field (corresponding to $\theta = 90°$).

To measure $B_c(\theta)$, we measured the resistance of the sample while sweeping the out-of-plane field and keeping the in-plane field constant. We then increased the in-plane field by 5mT, and swept the out-of-plane field back in the other direction, and repeated these measurement up to an in-plane field of 250mT, above $B_c^{||}$ (see the results in Fig.C.4a as a magnetic field mapping).

From each sweep, we can extract the fields' values ($B^{||}$,$B^{\perp}$) for which $R(B^{||}, B^{\perp}) = R_N/2$, and compute the angles and magnitude of the total critical field. The results, presented in Fig.4.11, show a clear peak of the critical field around the in-plane field direction, and a minimum for an out-of-plane field, as expected from the theory. As we can see in the zoomed-in inset, the peak is centered around $\theta = 91.1°$, rather than 90°. This angular shift is due to a physical misalignment of the sample in our system.

Even though it is small, this misalignment has a very significant impact on our measurements, as the measured in-plane critical magnetic field is actually reduced by about 29% compared to the "true" in-plane critical field. The figure shows fits of the data to either the 3D Ginzburg-Landau model (eq.1.6, in blue), or the 2D Thinkham model (eq.1.7, in red), with no parameter constraint (free parameters for the fit are the in- and out-of-plane critical fields, as well as the misalignment angle). The 2D model globally fits the data better than the 3D model, which cannot account for the cusp-like shape of the peak.

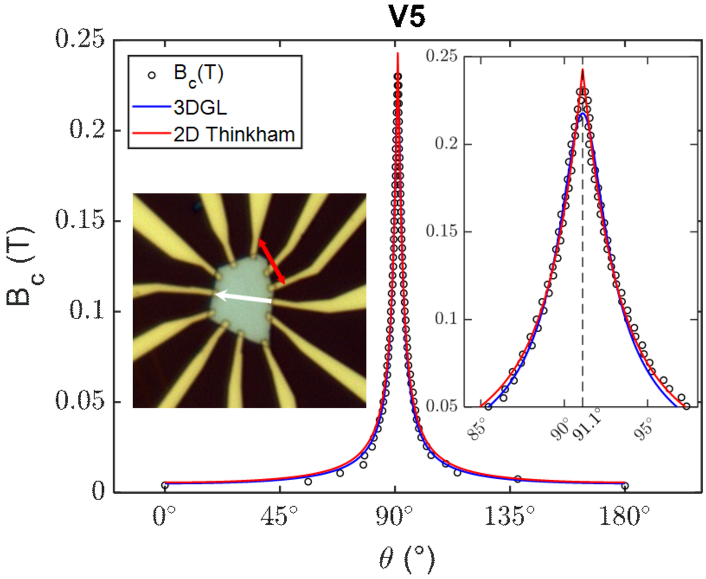

Figure 4.12: Angular dependence of the critical magnetic field for V5, with $\theta = 0°$ corresponding to an out-of-plane field. This data was extracted from Fig.C.5a, and was fitted with the 3D Ginzburg-Landau model (in blue), and the 2D Thinkham model (in red). Inset: Zoom-in on the peak, which is centered around $\theta = 91.1°$, due to a physical misalignment of the sample.

We repeated this analysis with other pairs of contacts (see e.g. configuration V5 in Fig.4.12), all of which also show cusp-like peaks around the in-plane direction, with the same misalignment of 1.1°. This cusp-like angular dependence of the critical field, well fitted by the 2D-Tinkham model, and reproducible on different contact configurations, constitutes a first strong indication of the reduced dimensionality of the superconductivity in our sample.

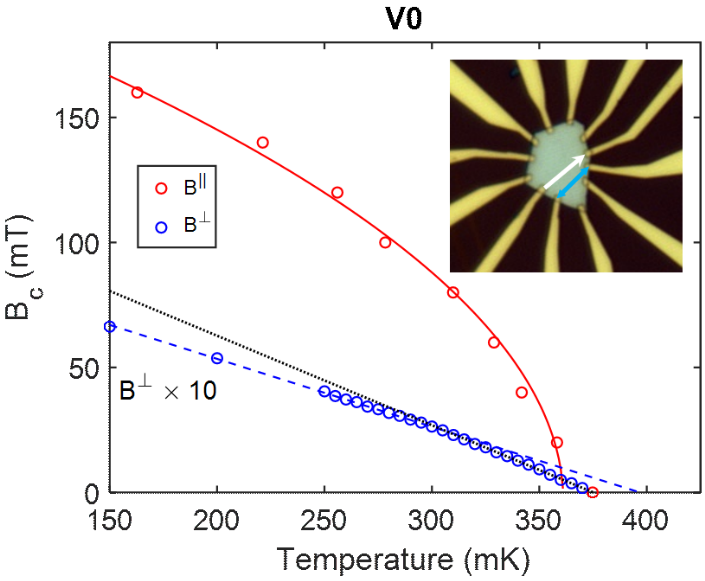

Figure 4.13: Temperature dependence of the critical magnetic field for V0, both in- and out-of-plane (red and blue respectively), extracted from Fig.C.4b. The out-of-plane field was increased by an order of magnitude for visibility. The data was fitted with a misalignment-corrected 2D Ginzburg-Landau model. For the out-of-plane critical field, two fits were done: from 150mK to 295mK in dashed blue, and from 300mK to T_c in dotted black.

Temperature dependence of the critical field

To confirm the reduced dimensionality of the superconductivity, we studied the temperature dependence of the critical field, both in-plane and out-of-plane. Since the field measurements were done along the coil's directions, we need to adapt the Ginzburg-Landau model for the in-plane field (eq.1.4). This can be done by injecting the temperature dependence of $B_c^{||}(T)$ and $B_c^{\perp}(T)$ (respectively eq.1.4 and eq.1.5) into eq.1.7, giving:

$$B_c(\theta,T) = \frac{1}{2}\frac{B_c^{||}(T)^2}{B_c^{\perp}(T)}\frac{|cos\theta|}{sin^2\theta}\left(\sqrt{1+4\frac{B_c^{\perp}(T)^2}{B_c^{||}(T)^2}\frac{sin^2\theta}{cos^2\theta}}-1\right). \tag{4.1}$$

We used the original Ginzburg-Landau equation 1.5 for the out-of-plane field, as the misalignment has no significant impact in this direction (see configuration V0 in Fig.4.11).

For the out-of-plane field, the measurements were made by sweeping the field back and forth at constant temperature. The temperature is increased between each sweep by 50mK from 150mK to 250mK, and then by 5mK from 250mK to 450mK.

For the in-plane magnetic field, in order to avoid issues associated with the metastabilities mentioned previously, the temperature was increased at fixed magnetic field (in steps of 20mK). For each field, the temperature was stabilized for 30 minutes, and the resistance was taken as the average over the last 50 points measured in order to enhance the signal-to-noise ratio. Then, the magnetic field was increased by 20mT (from 0T to 200mT) while the sample cooled-down, and the procedure was repeated. Due to the very long time required to do these measurements, we only measured over temperature ranges close to the transition at each field, to reduce the overall duration of the measurements. The full mapping obtained can be see in Fig.C.4b.

The temperature dependence of the critical field, for both orientations of the field, is plotted in Fig.4.13 (the out-of-plane critical field was enhanced by an order of magnitude for better visibility). The out-of-plane critical field still shows a linear dependence in temperature, as expected by the Ginzburg-Landau theory in both the 3D and confined cases. Nevertheless, two different slopes can be observed for different temperature ranges: from low temperature up to 295mK, the linear fit (dashed blue line) yields $T_c = 400\text{mK}$ and $\xi_0 = 176\text{nm}$, according to the Ginzburg-Landau model. This is not consistent with other measurements, which indicate that T_c is closer to 370mK. However, from 300mK on, a transition to another linear temperature dependence is observed (dotted black line), corresponding to $T_c = 376\text{mK}$ and $\xi_0 = 158\text{nm}$, in excellent agreement with our $R(T)$ measurements. This is also in perfect agreement with the zero-field measurements we did for the in-plane field-temperature mapping, which gives $T_c = 375\text{mK}$.

We have noticed a similar change of slope for the out-of-plane critical field's temperature dependence in all our different samples, and for different contact configurations. The determination of the origin of this phenomenon goes well beyond the scope of this manuscript, but it might be linked to inhomogeneities in the superconducting transition. We will discuss more about these inhomogeneities later in sec.4.3.4.

Contrarily to the out-of-plane field, the in-plane critical magnetic field no longer shows a linear temperature dependence in exfoliated structures. Taking into account the sample's 1.1° misalignment, we can fit the temperature dependence with the 2D Ginzburg-Landau theory (eq.4.1), which is shown in red in Fig.4.13. From the theory, we can extract three parameters: the critical temperature $T_c = 361\text{mK}$, less than 4% away from the value obtained from the $R(T)$; the superconducting thickness $d_{SC} = 57\text{nm}$, which is of the order of the sample's thickness ; and the in-plane coherence length at zero temperature $\xi_0^{||} = 138\text{nm}$, close to the value obtained from the out-of-plane critical field. These results can be reproduced for other contact configurations, with very similar parameters (see Fig.C.3).

The critical field's temperature dependence (in both field orientations), together with the critical field's angular dependence, show the 2-dimensional nature of the superconductivity in thin exfoliated samples of tr-PtBi$_2$. We investigate further the low dimensionality of the superconducting state in the following section, and evidence a Berezinskii–Kosterlitz–Thouless (BKT) transition in thin exfoliated samples.

4.3.3 Berezinskii–Kosterlitz–Thouless transition

V(I) characteristics

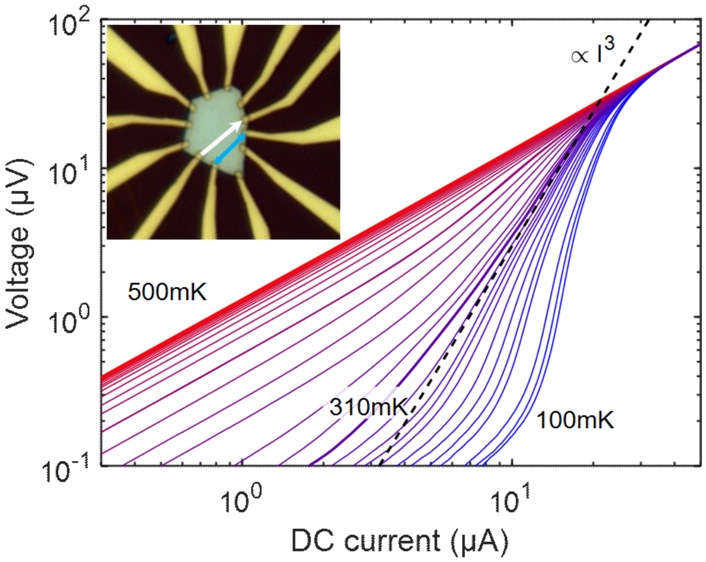

Figure 4.14: Current-voltage V(I) characteristics of V0 at different temperatures, shown in logarithmic scale. The characteristics vary continuously from superconducting to normal state in temperature. At $T = 310$mK, the slope of the characteristics reaches a maximum of 3 (black dashed line), typical of a BKT transition.

One typical way of identifying a BKT transition in transport is to consider the temperature dependence of the current-voltage V(I) characteristics. In a perfect material, at high temperature ($T > T_c$) the potential should follow Ohm's law at any current, while at lower temperature ($T < T_c$) and at low enough current ($I < I_c$), the voltage should drop down to zero. In a BKT transition, the potential is expected to follow a temperature dependent power law $V \propto I^{a(T)}$ (see sec.1.3.4). The exponent a is equal to 1 in the normal state, and increases at lower temperature for $T < T_c$ (with T_c the BCS critical temperature). In a homogeneous and infinite sample, the exponent shows a jump at the BKT temperature T_{BKT}, from $a(T_{BKT}^{+}) = 1$ to $a(T_{BKT}^{-}) = 3$, and keeps increasing with decreasing temperatures, while in an inhomogeneous and finite sample the transition is expected to be broadened in temperature. In both cases, the BKT temperature T_{BKT} is defined by the relation $a(T = T_{BKT}) = 3$.

In order to evidence a BKT transition, we measured V(I) characteristics at different temperatures, from $T = 100$mK to $T = 500$mK. In practice, in order to enhance the signal-to-noise ratio, we measured the differential resistance (see Fig.C.6) and integrated it, after having checked the equivalence with direct $V(I)$ measurements. The data for V0 is plotted in logarithmic scale in Fig.4.14 to make the power law more visible. A temperature dependence typical of BKT transitions is evidenced, with an increasing slope (i.e. power law exponent) with decreasing temperature. At around $T = 310$mK, the power law exponent reaches 3 (dashed black line), and keeps increasing at lower temperature.

Power law exponent

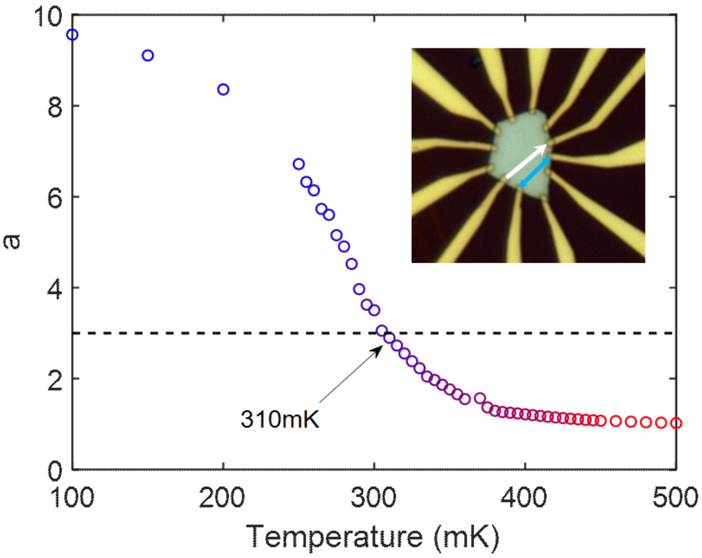

Figure 4.15: Maximum of the exponent of the V(I) power law at different temperatures, extracted from Fig.C.7a, making it easier to identify precisely $T_{BKT} = 310$mK.

A more accurate method of analyzing the power laws is to perform the logarithmic derivative of V(I) at different temperatures, $a(I_{DC},T) = \left.\frac{\partial log(V)}{\partial log(I_{DC})}\right|_T$ (see Fig.C.7a), and to extract the temperature dependence of their maximum, as presented in Fig.4.15. This analysis shows that, at high temperature, the exponent is constant and equal to 1, and starts to increase around $T = T_c = 370$mK, before reaching 3 at a temperature between 305mK and 310mK, confirming our initial analysis. It then increases further at lower temperature. This indicates again that a BKT transition takes place around $T_{BKT} = 310$mK.

This method suffers from one important drawback: since it is based on V(I) sweeps, a "large" DC current ($I_{DC} \sim 20\mu A \gg I_{AC} = 1\mu A$) has to be applied to the sample, which brings the electrons out of equilibrium. Due to our sample's low resistance (typically $R \sim 1\Omega$ in the normal state), the excitation energy of the current $eV_{DC} \sim 20\mu V$ remains lower than the broadening of the Fermi-Dirac distribution at low temperature ($4k_BT \sim 35\mu V$ at 100mK), so that measurements are done very close to equilibrium, avoiding heating issues related to electron-electron interactions. Nevertheless, we will show below that the temperature dependence of the resistance at low current provides another signature of the BKT transition, at equilibrium.

Temperature dependence of the resistance

In a homogeneous material, the resistance of an infinite sample should drop to zero below $T = T_{BKT}$. As we mentionned earlier in sec.1.3.4, the Halperin-Nelson theory [Halperin and Nelson, 1979] gives an expression of the temperature dependence of a sample above $T = T_{BKT}$:

$$\begin{aligned} R(T)/R_N &= \frac{1}{1+\Delta\sigma/\sigma_N}, \text{with} \\ \frac{\Delta\sigma}{\sigma_N} &= \frac{4}{A^2}\left[sinh\left(2\alpha\sqrt{\frac{T_c - T_{BKT}}{T - T_{BKT}}}\right)\right]^2, \end{aligned} \tag{4.2}$$

where A is a number of order unity and α is the scale of the vortex-core energy (typically $\alpha \sim 1$). No reasonable fit of our data can be achieved using this formula without some of the parameters taking meaningless values. This is due to the presence, in our data, of a resistance "tail" at low temperature (see Fig.4.16) which is incompatible with the Halperin-Nelson model which predicts $R(T < T_{BKT}) = 0$.

If we fix $T_{BKT} = 310$mK, as obtained previously from the $V(I)$ measurements, the best fit is obtained for the parameters $A = 2.86$, $\alpha = 0.37$ and $T_c = 512$mK

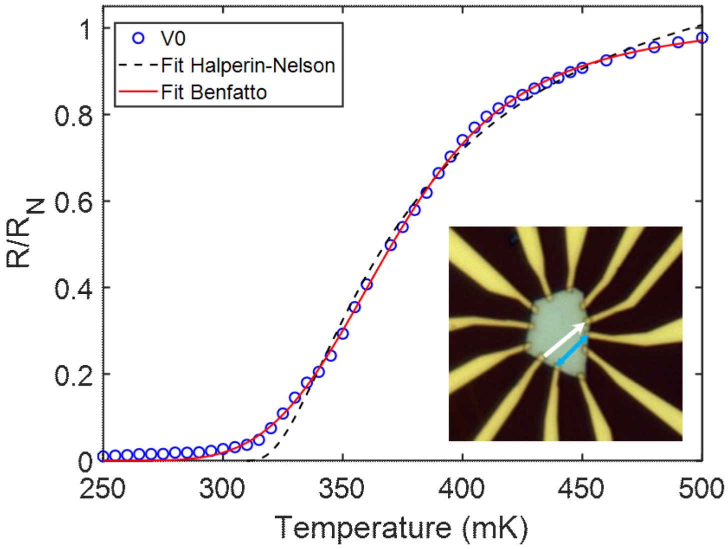

Figure 4.16: Temperature dependence of the reduced resistance (same data as in Fig.4.8, in blue.) The reduced resistance is fitted with both the Halperin-Nelson (homogeneous) model, in black, and the Benfatto (ingomogeneous) model, in red. The homogeneous model cannot represent the data correctly. The inhomogeneous model gives a small gaussian broadening of the transition temperature, with $\delta =$ 25mK, and accounts very well for our measurements over the entire measured temperature range.

(black dashed line in Fig.4.16). The large value of T_c is an artificial attempt at broadening the transition, but it is incompatible with our other measurements of $T_c \sim 370$mK.

Following the model of [Benfatto et al., 2009] (see sec.1.3.4), we can take into account the spatial inhomogeneities in our sample by considering a broadening of the transition temperature, in the form of a Gaussian distribution. The temperature dependence of the resistance thus follows

$$\frac{R(T)}{R_N} = \frac{1}{\sqrt{2\pi}\delta} \int \mathrm{dt} \exp\left(-\frac{(t-T_{BKT})^2}{2\delta^2}\right) \times \left(1 + \frac{4}{A^2}\left[sinh\left(b\sqrt{\frac{t}{T-t}}\right)\right]^2\right)^{-1}, \tag{4.3}$$

with δ the Gaussian spread of T_{BKT} and $b = 2\alpha\sqrt{(T_c - T_{BKT})/T_{BKT}}$. By fixing both $T_c = 370$mK and $T_{BKT} = 310$mK to the values determined previously (from $R(T_c) = R_N/2$ and the V(I) characteristics, respectively), we obtain a very good fit of our data (see red line in Fig.4.16) over the entire temperature range.

We obtain as parameters, $A = 18.5$, $b = 1.27$, and the transition temperature broadening $\delta = 25$mK. This broadening is consistent with the range of T_c measured between different contact configurations, which is of the same order (see e.g. configurations V2 and V3 in Fig.4.10b and V4 and V5 in Fig.4.20a with, respectively, $T_c^{V2} = 354$mK, $T_c^{V3} = 374$mK, $T_c^{V4} = 406$mK and $T_c^{V5} = 346$mK). At low temperature, the fit deviates slightly from the data, which is non-zero, due to measurements artifacts related to common mode rejection ratio issues, a limitation of the measurement of low impedance samples with lock-in techniques.

Combined with the V(I) characteristics' temperature dependence, this shows the existence of a BKT transition in nano-structure S1. This is highly unusual, as this sample is relatively thick (60nm, which corresponds to several dozen layers), and BKT transitions have until now only been reported for films thinner than 12nm [Mondal et al., 2011]. This led us to study more structures with different thicknesses, to confirm the existence of this transition, and potentially evidence it in even thicker structures.

Thinner structure

In addition to sample S1, we measured three more samples of varying thickness, between 41nm and 126nm (S3, S4 and S5). However, we can only apply the previous analysis to sample S3, as we will explain in more details in the next section (sec.4.3.4). Since sample S3 is thinner than sample S1 (41nm vs. 60nm), we expect it to show a BKT transition as well. Looking at the temperature dependence of the V(I) characteristics (shown in logarithmic scale in Fig.4.17a), we see again that the slope reaches a cubic power law, between $T = 350$mK and $T = 375$mK. As for the previous sample, we analyzed the logarithmic derivative of the V(I) curves (see Fig.C.7b) and extracted the maximal power-law exponents reached at each temperature (Fig.4.17b). By interpolating the data presented in the graph, we determine the BKT temperature $T_{BKT} \sim 369$mK.

Using the same analysis procedure as before, we can then fit the resistance temperature dependence, with either the homogeneous Halperin-Nelson model, or the inhomogeneous Benfatto *et al.* model, with T_{BKT} fixed at the value determined from the V(I) characteristics above (see Fig.4.18). We see that, as for S1, the inhomegeneous model fits our data better, with a significantly smaller broadening of the transition temperature than for S1 ($\delta = 11$mK). The other parameters of the fit are $A = 3.15$ and $b = 0.25$. This confirms the existence of a BKT transition in S3. It also rules out the experimental setup as the cause of the broadening of T_{BKT} (e.g. from line filtering issues in the dilution fridge), since both samples should

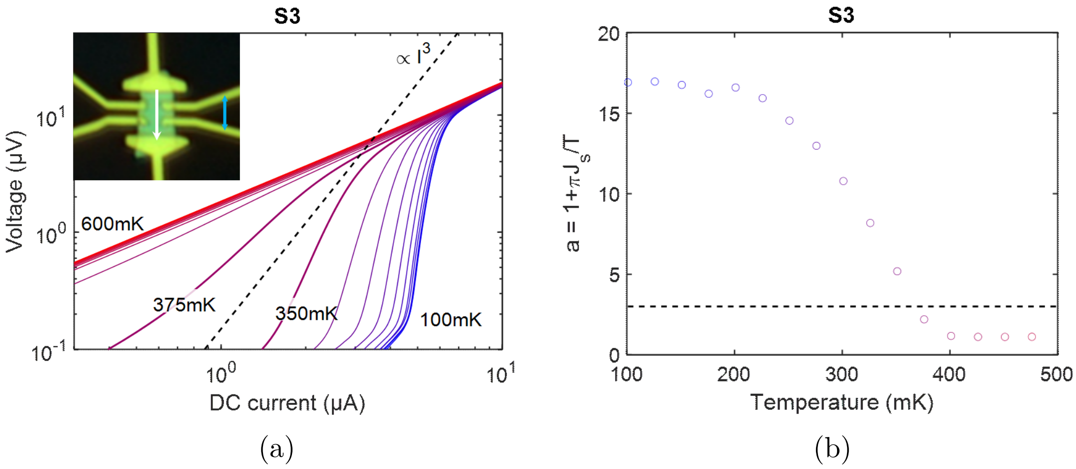

(a) (b)

Figure 4.17: (a) Current-voltage characteristics V(I) at different temperatures, shown in logarithmic scale, for sample S3, which is 41nm thick. The characteristics vary continuously in temperature from the superconducting to the normal state. Between $T = 350$mK and $T = 375$mK, the slope of the characteristics reaches a maximum of 3 (black dashed line), typical of a BKT transition. Inset: optical image of S3 with the contact configuration used (current along the white arrow, voltage along the blue double arrow). (b) Maximum of the exponent of the V(I) power law at different temperatures, extracted from Fig.C.7b, making it possible to identify the transition temperature with more precision, with $T_{BKT} = 369$mK.

then have a similar broadening. The lower transition temperature broadening for S3 implies, in our interpretation, a smaller inhomogeneity of the superconducting state.

Therefore we have strong evidence, both in the V(I) characteristics and in the temperature dependence, of a BKT transition happening in two exfoliated samples, 41nm and 60nm thick, much above what has previously been reported in the litterature [Mondal et al., 2011]. The shape of the temperature dependence can be well understood by taking into account spatial inhomogeneities in the superconducting state, which result in a minimal, sample dependent broadening of the BKT transition temperature.

4.3.4 Inhomogeneous superconducting transitions

In every sample and configuration we have studied we have noticed some deviations from the expected superconducting transitions, whether in temperature, magnetic field or current. Depending on the contact configurations, these deviations varied

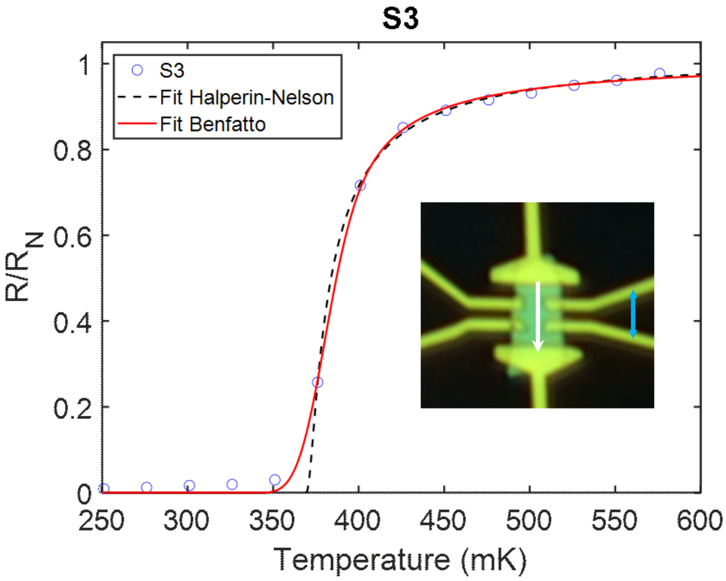

Figure 4.18: Temperature dependence of the reduced resistance of S3. The reduced resistance is fitted with both a spatially homogeneous BKT model, in black, or a spatially inhomogeneous one, in red. The homogeneous model cannot represent our data correctly. The inhomogeneous model gives a small gaussian broadening of the transition temperature, with $\delta = 11$mK, and account very well for our measurements over the entire measured temperature range.

in nature and amplitude, making analysis and interpretation of the data more difficult. In the previous section, we have shown the results for which deviations were not too significant, and for which the results were therefore unambiguous. In this section, we will discuss in more details about the nature of these different variations, about their consequences in our different samples, and about their possible origin.

We will discuss below three different types of deviations: an overshoot, a multi-step feature and an inflection point in R(T) and R(B), all of which are related to inhomogeneities of the superconductivity.

Resistance peak above the transition

As we already mentioned in sec.4.3.1, some configurations show a small peak of resistance following the superconducting transition. In Fig.4.19a, we present the temperature dependence of the resistance for three contact configurations of sample S1. Even high above their T_c (371mK, 354mK and 374mK for V1, V2 and V3

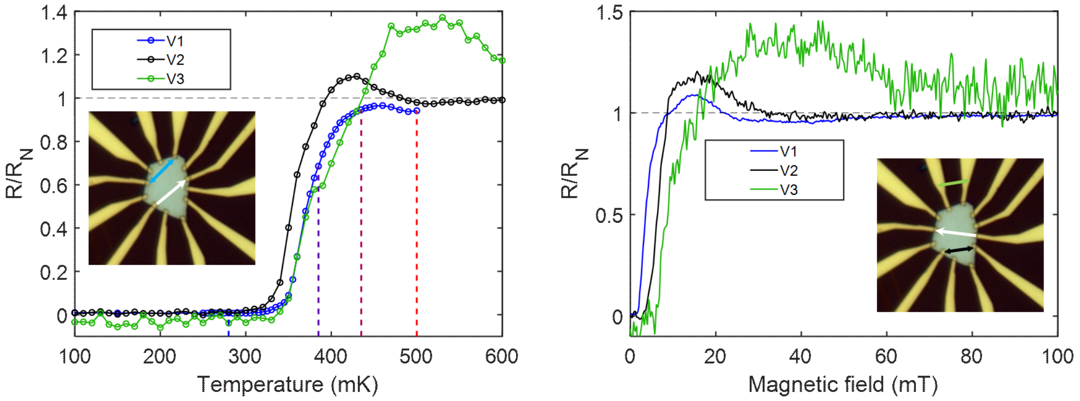

(a)

(b)

Figure 4.19: (a) Temperature dependence of the normalized resistance for 3 different contact configurations of sample S1, shown in the insets. The current for each configuration is represented by the white arrow, while the resistance is measured between the contacts indicated by the colored double arrows. The vertical colored dashed-lines correspond to the different temperatures considered in Fig.4.24. (b) Out-of-plane magnetic field dependence of the normalized resistance, for the same configurations as in (a).

respectively), defined as previously as $R(T_c) = R_N/2$, the resistance does not saturate at $R = R_N$. For V1 and V2, we can see that the peak is followed by a small depression of the resistance below R_N and before the saturation to R_N, a property which could not be evidenced for V3 in the temperature range studied, and because of the higher noise level. These effects (peak and depression) are better revealed in the (out-of-plane) field dependence (see Fig.4.19b), where both V1 and V2 reach $R = R_N$ around $B \sim 60$mT, which corresponds to about $10B_c$.

Multiple-step transition

Other deviations from the usual superconducting transition have been observed in different samples and contact configurations. For instance, configuration V4 of sample S1 (Fig.4.20a, in blue) shows a step in the resistance's temperature dependence around $T = 450$mK, with a resistance plateau over about 100mK, before increasing again until the highest measured temperature ($T = 600$mK). Despite the fact that $T_c \sim 406$mK, the normal resistance is still not reached at $T = 600\text{mK} = 1.5T_c$. On the other hand, configuration V5 (in red) shows a brutal change of slope to a much lower one around $T = 370$mK. V5 also displays a small

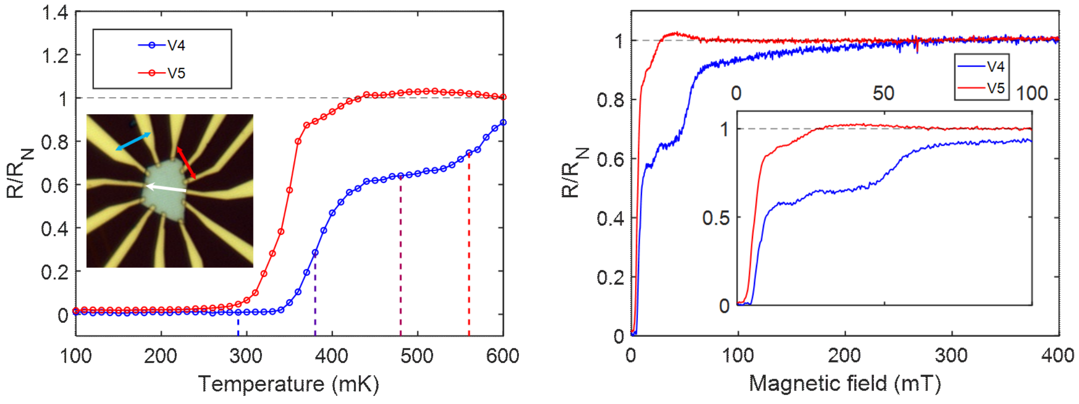

(a) (b)

Figure 4.20: (a) Temperature dependence of the normalized resistance for 2 different contact configurations of sample S1, shown in the insets. The current for each configuration is represented by the white arrow, while the resistance is measured between the contacts indicated by the colored double arrows. The vertical colored dashed-lines correspond to the different temperatures considered in Fig.4.25b. (b) Out-of-plane magnetic field dependence of the normalized resistance, for the same configurations as in (a).

peak of resistance around $T = 500$mK, as described in the previous section, and V3 (in green in Fig.4.19a) also shows a small shoulder around $T = 380$mK, showing that these deviation to the usual transition may occur concurrently.

We can again look at the magnetic field dependence of the resistance for these contacts for comparison. Similarly to its temperature dependence, V4 shows a step-like behavior with a plateau around 20mT. The resistance reaches the normal resistance at $B \sim 300$mT, or about $30B_c$. V5 also shows a change of slope followed by a small peak, respectively around 9mT and 40mT. Magnetic field measurements are easier to perform than temperature measurements, which require a stabilization of the temperature. Therefore, they can reveal finer structures than R(T) characteristics. For instance, instead of a single step, V4 shows a change of slope at 11mT followed by two steps (from 14mT to 19mT and 27mT to 44mT). The resistance then increases again quickly, until about 65mT, before slowing down until about 300mT. This slow increase cannot be attributed to the magnetoresistance, as the resistance then stays constant for about 550mT before rising steadily with the field again.

While the resistance peaks and steps are the most visible deviations from the standard superconducting transition, changes of slope, or small shoulders, are much more frequent. Overall, every sample we measured showed at least one such feature.

Inhomogeneous transition model

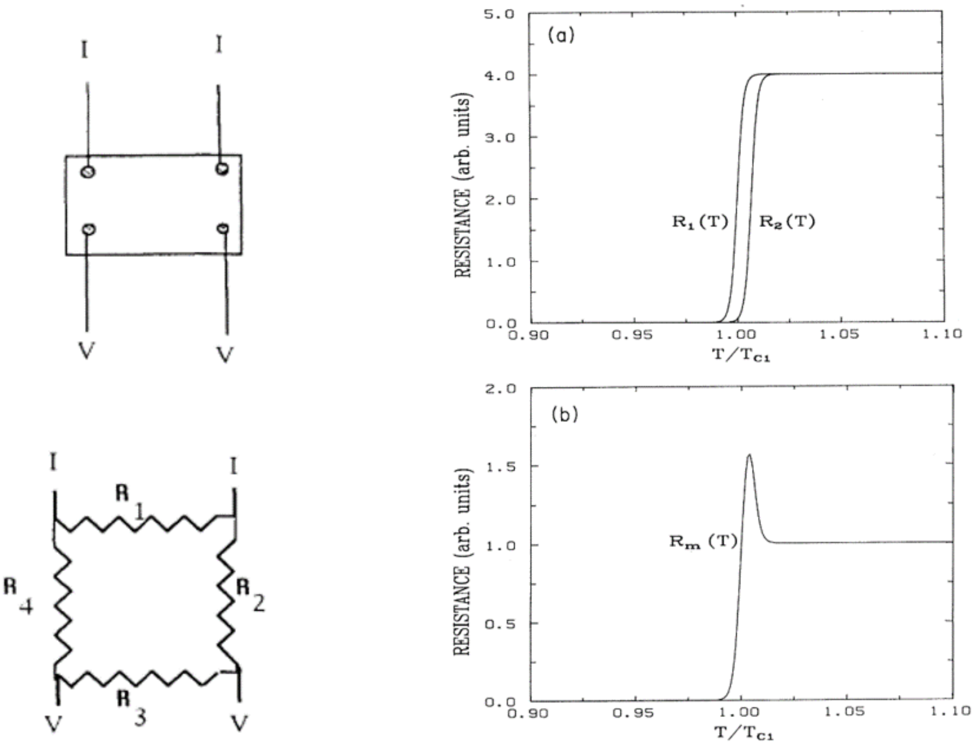

(a) (b)

Figure 4.21: Model explaining the peak above the critical temperature in superconducting transitions. Adapted from [Vaglio et al., 1993]. (a) Top: Out of line contact configuration required for the peaks to appear. Bottom: Modelization of the configuration above as a resistance circuit, with $R_1 = R_3$ & $R_2 = R_4$. (b) Top: Temperature dependences of R_1 and R_2. The transitions are considered the same, with a small shift in T_c ($T_{c2} = 1.007 \times T_{c1}$). Bottom: Measured resistance $R_m = V/I$ (formula in main text), displaying a peak just above T_c.

Resistance peaks above the superconducting transition such as described above have already been observed in the early 1990's in disordered superconductors, for particular current/voltage contact configurations [Lindqvist et al., 1990; Nordström and Rapp, 1992]. Possible origins raised at the time included current redistribution and vortex motion, creating transverse voltage in the absence of a magnetic field. Soon after, Vaglio et al. [1993] proposed a simple model attributing the origin of the peaks to spatial inhomogeneities of the superconducting transition. In this model, they consider a typical four-probe measurement scheme with out-of-line current and voltage probes (see Fig.4.21a), which can be simplified as a square circuit of four resistances (for simplicity, $R_1 = R_3$ & $R_2 = R_4$). The measured resistance is then $R_m = \frac{V}{I} = \frac{R_1^2}{2(R_1^2 + R_2^2)}$. By considering that each resistance follows a superconducting transition temperature-dependence, and taking R_1 and R_2 to have a slightly different T_c, they could reproduce the observed peak of resistance above T_c (see Fig.4.21b).

Vaglio et al. [1993] attributed all differences between the superconducting transitions to inhomogeneities in their samples, which modify slightly the T_c in different areas of the film, and they confirmed through in-line measurements (which do not show this effect) that their samples indeed showed a small spatial inhomogeneity of the T_c.

We can extend this model in different ways. First we use the Halperin-Nelson formula to modelize the superconducting transition, since we know our samples show a BKT transition:

$$\frac{R(T)}{R_N} = \left(1 + \frac{4}{A^2}\left[sinh\left(2\alpha\sqrt{\frac{T_c - T_{BKT}}{T - T_{BKT}}}\right)\right]^2\right)^{-1}, \tag{4.4}$$

We then have four tunable parameters (if we consider the normal resistance to be the same, for simplicity): α and A, which determine the sharpness of the transition, as well as the two transition temperatures T_c and T_{BKT}. As in the original model, we will consider only two different transitions, R_1 and R_2, in order to give a proof of principle rather than an accurate fit of our data. For simplicity, we will always consider the same transition for R_1, with parameters $\alpha_1 = 0.34$, $A_1 = 4$, $T_{c,1} = 370$mK and $T_{BKT,1} = 310$mK, which describe more or less accurately the transition in S1. By varying the transition R_2, it is possible to reproduce the three previously observed deviation types.

We first take for R_2 the same transition as for R_1, but shifted by 15mK ($T_{c,2} = 385$mK and $T_{BKT,2} = 325$mK). As in the study of Vaglio et al. [1993], this leads to a sharp peak above $T_{BKT,1}$ (see Fig.4.22). Interestingly, since the BKT transition results in a variation of the resistance over a much broader range of temperatures than the regular GL transition, it leads to a small depression of resistance just after the peak. This is similar to what we observe in several contact configurations (e.g. V1 and V2). Importantly, it is impossible to obtain such a depression when considering a standard second-order transition (see below), as in the original model,

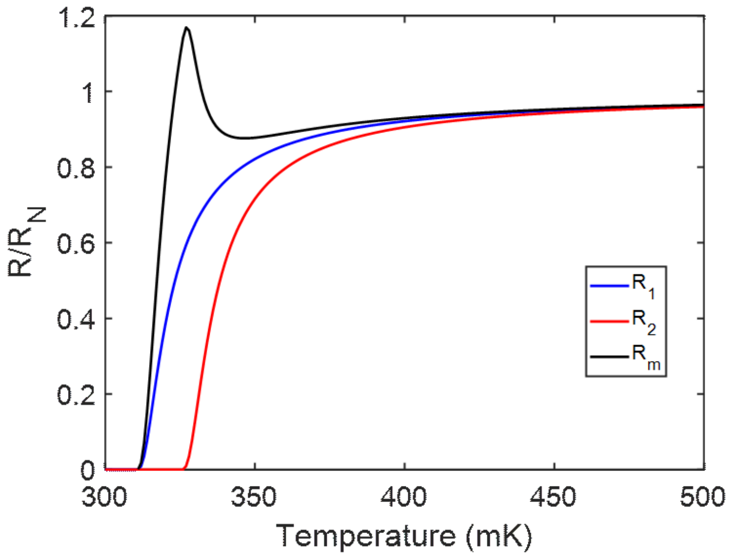

Figure 4.22: Measured resistance R_m (in black) obtained for R_1 and R_2 (in blue and red, respectively). The two transitions are described by the Halperin-Nelson formula, with $\alpha_1 = 0.34$, $A_1 = 4$, $T_{c,1} = 370$mK and $T_{BKT,1} = 310$mK for R_1, and $\alpha_2 = \alpha_1$, $A_2 = A_1$, $T_{c,2} = 385$mK and $T_{BKT,2} = 325$mK for R_2. The measured resistance R_m shows a peak followed by a small depression.

which confirms that a BKT transition occurs in S1.

If we now consider that the spatial inhomogeneities in the superconducting state may not only shift the transition in temperature, but also affect it's shape (i.e. $\alpha_2 \neq \alpha_1$ and $A_2 \neq A_1$), we can explain the two other observed behaviors in the measured resistance. As before, we consider a second transition R_2 shifted to higher temperatures (i.e. $T_{c,2} > T_{c,1}$), but also sharper than R_1, so that the two transitions may cross (see Fig.4.23). For instance, if we take as parameters $\alpha_2 = 0.5$, $A_2 = 10$, $T_{c,2} = 400$mK and $T_{BKT,2} = 312$mK, we obtain an abrupt change to a smaller slope above $T_{BKT,2}$ (Fig.4.23a), as observed in V1, V2 and V5. If we increase very slightly $T_{BKT,2} = 314$mK, we may even obtain a small plateau of measured resistance in the transition (Fig.4.23b), followed by an increase with a different slope than before. This was seen in V4, as well as in other structures.

We can obtain very similar results for all three deviations by considering a simple second-order transition (modelized by $R(T) = \dfrac{A}{1+e^{-a\frac{T-T_c}{T_c}}}$, see appendix section C.2.3). However in this case, the model cannot reproduce the small depression of resistance after the peak.

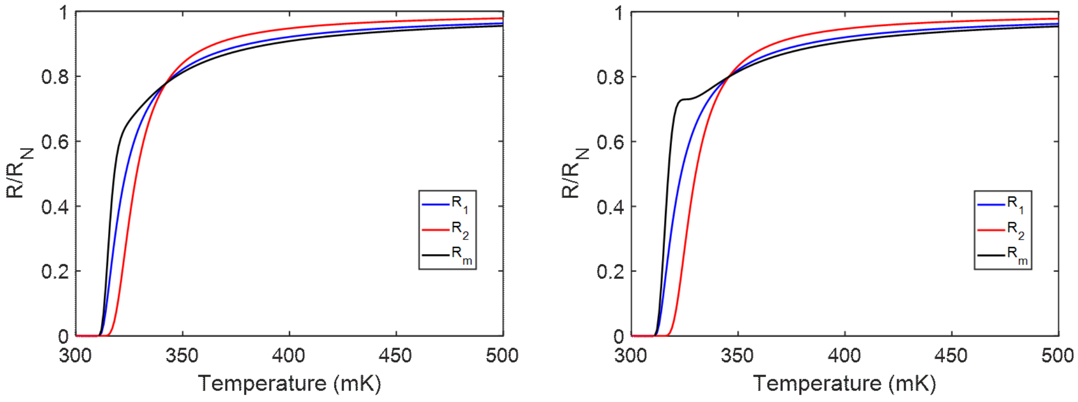

(a) (b)

Figure 4.23: Measured resistance R_m (in black) obtained for R_1 and R_2 (in blue and red, respectively). The two transitions are described by the Halperin-Nelson formula, with for R_1 $\alpha_1 = 0.34$, $A_1 = 4$, $T_{c,1} = 370$mK and $T_{BKT,1} = 310$mK, and for R_2 $\alpha_2 = 0.5$, $A_2 = 10$, $T_{c,2} = 400$mK and either $T_{BKT,2} = 312$mK (a) or $T_{BKT,2} = 314$mK (b). The measured resistance R_m shows either a brutal change of slope (a), or a plateau (b).

This model could be extended to represent more accurate transitions, to include more than two different resistances and to take into account the precise contact geometries of each studied configuration. Nonetheless, our simple approach is satisfactory since it can qualitatively reproduce every deviation from the standard transition we have measured, and it suggests that inhomogeneities in the superconductivity have a significant influence on our measurements.

Origin of inhomogeneities of the superconductivity

This model is very general and only requires spatial inhomogeneities in the superconducting transition to function, without presupposing anything about their origin. We discuss below about the potential origins of inhomogeneities in our samples.

The first possibility could be spatial inhomogeneities in the sample itself, either in the charge density, the transport length, the local thickness, or in other types of defects originating from the mechanical exfoliation for instance. However, AFM images do not indicate any significant variation of thickness in S3 and S4 (they are flat to around $\sim$ 1nm, which should not have any major impact on the superconductivity in the sample's bulk), even though these samples show the same kind of deviations from the typical superconducting transition as discussed above (see Fig.C.9 for S4).

To gain more insight into the inhomogeneities, we can look at the differential resistances $dV/dI(I_{DC}, T)$ of the different contact configurations, and their evolution with temperature. Since the transition from superconducting to normal state at $I_{DC} = I_c$ is accompanied by peaks of differential resistance, this is a sensitive measurement to investigate whether a contact configuration detects contributions from multiple superconducting transitions, as suggested by our model.

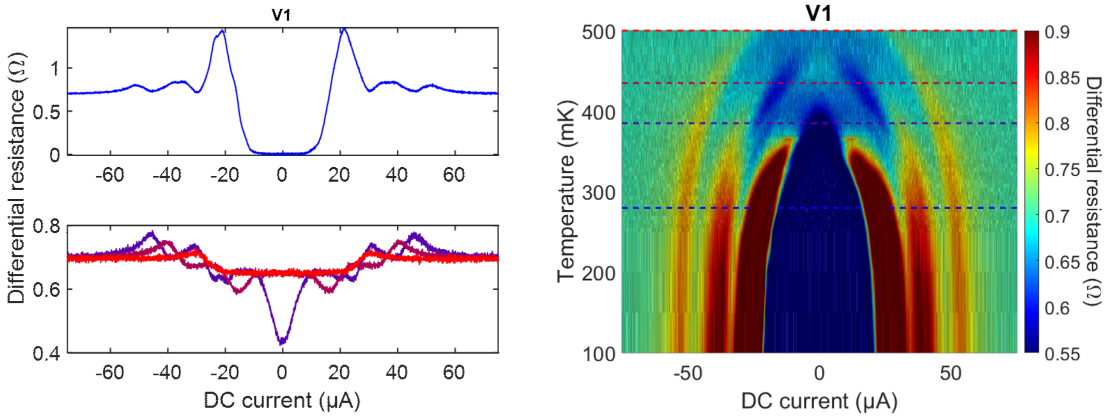

(a) (b)

Figure 4.24: (a) Differential resistance of V1 (S1) at different temperatures, shown with dashed lines in Fig.4.19a and (b), and color coded, with (from blue to red), $T_1 = 280$mK, $T_2 = 385$mK, $T_3 = 435$mK and $T_4 = 500$mK. (b) Colormap of the differential resistance of V1 versus DC current and temperature. The color scale is set to enhance the differential resistance peaks, which can be seen in red to yellow.

In Fig.4.24a, we represent such differential resistance curves for V1 at 4 different temperatures, $T_1 = 280$mK, $T_2 = 385$mK, $T_3 = 435$mK and $T_4 = 500$mK. At low temperature (blue curve), before the beginning of the superconducting transition ($R(T_1) = 0$, see Fig.4.19a), we have a typical differential resistance profile, with a zero resistance plateau at low current surrounded by two peaks. These peaks are themselves surrounded by 2 additional pairs of peaks at higher currents. At higher temperature, during the increase of resistance (T_2, in purple), the inner peaks disappear while the other peaks are slightly reduced and shifted to lower currents. At T_3, in dark red, we still see signs of peaks, and a plateau of resistance at low current at $R \sim 0.94 R_N$. When increasing the temperature up to T_4 in red, where $R(T)$ has almost reached R_N, we measure only one pair of small peaks, surrounding a very large plateau at the same resistance $R \sim 0.94 R_N$. The full temperature dependence of the differential resistance is shown in Fig.4.24b. We note that every pair of peaks behaves similarly in temperature, staying at constant current until a given temperature before moving to lower current as the temperature increases further, until they eventually merge and disappear at high enough temperature.

Interestingly, the last differential resistance profile at $T_4 = 500\text{mK}$ almost corresponds perfectly to what would be expected for a typical superconducting transition (two peaks surrounding a plateau of zero-resistance), but with a finite resistance at low DC current. This would correspond to the differential resistance of a superconducting domain in series with a domain of constant resistance (e.g. a domain in the normal state). Generally, these measurements support our interpretation in terms of multiple superconducting transitions in our sample.

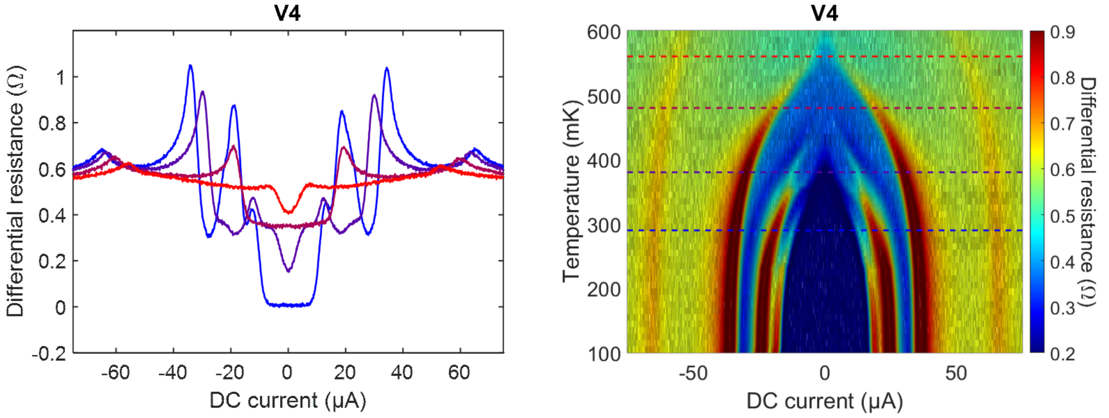

(a) (b)

Figure 4.25: (a) Differential resistance of V4 (S1) at different temperatures, shown with dashed lines in Fig.4.19a and (b), and color coded, with (from blue to red), $T_1 = 290\text{mK}$, $T_2 = 380\text{mK}$, $T_3 = 480\text{mK}$ and $T_4 = 560\text{mK}$. (b) Colormap of the differential resistance of V4 versus DC current and temperature. The color scale is set to enhance the differential resistance peaks, which can be seen in red to orange.

We can see something very similar in the differential resistance for configuration V4: Fig.4.25a shows many peaks surrounding a zero resistance state at low temperature, but as the temperature increases these peaks disappear slowly. At $T_3 = 480\text{mK}$ (in dark red, see Fig.4.20a), the differential resistance also shows a plateau at low current (at $R = 0.64R_N$) surrounded by two pairs of peaks. At higher temperature, we can see that the outermost pair of peaks still hasn't disappeared (see Fig.4.25b), which is supported by the fact that $R(T_4 = 560\text{mK}) < R_N$ (see Fig.4.20a).

The large similarities in the differential resistance evolution with temperature, for contact configurations showing otherwise different qualitative behaviors in the

$R(T)$, strengthens our hypothesis of spatial inhomogeneities in the superconducting transition. To confirm this, we are currently collaborating with S. Sykora (TUD, formerly IFF) to conduct percolation simulations on a 2D grid, with inhomogeneities represented by a randomized potential perturbation of the superconducting links, and preliminary results indicate good qualitative agreement with our data.

4.4 Summary and conclusion

In this chapter, we have shown that tr-PtBi$_2$ is a superconductor, in macro- as well as in nano-structures. While nano-structures show a lower T_c than macro-structures ($T_c \sim 370$mK for nano-structures compared to $T_c \sim 600$mK for macro-structures), they also show a much larger anisotropy in magnetic field, with respectively a much lower and a much higher critical field for the out-of-plane and the in-plane fields ($B_c^{\perp} \sim 6$mT and $B_c^{||} \sim 140$mT for nano-structures compared to $B_c \sim 50$mT for macro-structures). This anisotropy is due in part to a reduction of the dimensionality of the superconducting state in exfoliated structures, which we have characterized. We evidenced a BKT transition happening at low temperature in our two thinnest structures (S3 and S1, respectively 41nm and 60nm). To the best of our knowledge, both exfoliated structures are the thickest reported samples to exhibit a BKT transition (respectively 3 and 5 times thicker than for Mondal et al. [2011]).

We have also measured two additional structures (S4, 70nm and S5, 126nm) at the same time as S3, both of which also showed 2D superconductivity (determined from $B_c(T)$ and $B_c(\theta)$ measurements). However, we could not evidence a BKT transition in these samples, due to a lower resolution in temperature.

We characterized 3 main types of deviations to the expected superconducting transition, in temperature and magnetic field, and showed that each type could be obtained qualitatively by a simple model which considers inhomogeneities in the superconductivity resulting in several different transitions impacting the measurements. These deviations also have a strong impact on the V(I) characteristics. Their presence can make the analysis challenging, or even impossible for some contact configurations, since when the deviations are too important (e.g. long intermediate resistance steps, significant change of slope etc.), our definition of the critical parameters (e.g. $R(T_c) = R_N/2$) doesn't correspond to the middle of the transition anymore. We expect all our previous conclusions to stand despite these inhomogeneities, as our analysis was based on contact configurations which did not show significant deviations.

The strong impact of inhomogeneities on the superconducting state may be a possible explanation for the absence of bulk superconductivity in macroscopic crystals. Indeed, such inhomogeneities could result in a partial superconducting transition of the crystal with superconducting islands embedded in a normal metal (and vice versa), making the impact of the superconducting volume fraction of the sample not measurable by SQUID or specific heat measurements. If the superconducting islands are dense enough to percolate however, these macro-structures would appear superconducting in charge transport measurements.

Conclusion

In this thesis, we investigated the transport properties of trigonal-$PtBi_2$, a layered van der Waals material with strong spin-orbit coupling. We report for the first time, through density functional theory calculation, the existence of 12 symmetry-related Weyl nodes in its band structure, at 48meV above the Fermi energy. A detailed study of the energy dispersion around these points shows a minimal tilt, making tr-$PtBi_2$ a type-I Weyl semi-metal. These calculations also show a high sensitivity of the topological surface states on the surface termination, with a much higher intensity of the Fermi arcs' spectral weight for Bi_2-terminated surfaces than for Bi_4-terminated surfaces.

Magneto-transport measurements of macroscopic single crystals of tr-$PtBi_2$ show multiple-bands electronic transport, in agreement with our band structure calculations, with three bands contributing to Shubnikov-de-Haas oscillations. We characterized at low temperature an anisotropy of the magnetoresistance with the out-of-plane field orientation, which shows two symmetric maxima $\theta_{max} \sim 20°$ away from the out-of-plane direction. This anisotropy vanishes at higher temperature. The angle θ_{max} could possibly corresponds to an anisotropy of the Weyl cone pocket, which is oriented in this direction.

Thanks to the layered nature of tr-$PtBi_2$, we were able to exfoliate and study thin nano-structures with thicknesses of the order of the coherence length. At temperatures above 1K, these structures exhibit an anisotropic resistance when an in-plane magnetic field is rotated in the structure's plane. We characterized this anisotropic response to be a combination of a planar Hall effect, with a π-periodic variation of the longitudinal and transverse resistance, and an anomalous planar Hall effect, with a 2π-periodic contribution to the transverse resistance. Both effects are probably linked to the topological nature of tr-$PtBi_2$, with high Berry curvature in the band structure.

At very low temperature, around 600mK, macro-structures become superconducting. This does not seem to be a bulk superconductivity, as specific heat and SQUID measurements do not give any indication of superconductivity. Nonetheless, our charge transport characterization of the superconducting state is coherent with the 3D Ginzburg-Landau theory, with a linear temperature dependence of the in-plane critical magnetic field and only a small anisotropy in its magnetic field response. In this framework, a high coherence length of the superconductivity can be extracted, with $\xi_0 \sim 60$nm.

Nano-structures of tr-PtBi$_2$ become superconducting at a slightly lower temperature than macro-structures, around 370mK, and have a lower out-of-plane critical magnetic field as expected from their 2D geometry. Nonetheless, we have found that nano-structures show an enhanced stability of the superconductivity against in-plane fields, with an in-plane critical field up to three times higher than in macro-structures. By studying the temperature and angular dependence of the critical field, we characterized the dimensionality of the superconductivity to be two-dimensional. We also evidenced a Berezinskii–Kosterlitz–Thouless (BKT) transition in structures as thick as 60nm, which is 5 times larger than the thickest reported samples exhibiting such a transition. A small broadening in temperature of the BKT transition in the 60nm thick structure, which was visible in the temperature dependence of the resistance, could be attributed to inhomogeneities in the superconductivity.

Our study of tr-PtBi$_2$ has raises several important questions, and opens the way to further studies in different directions. A detailed characterization of the out-of-plane angular dependence of the magnetoresistance in macro-structures, and its temperature dependence, should be conducted in order to determine the origin of the anisotropy observed. If this anisotropy is indeed, as we believe, linked to the topological band structure, this might provide some experimental confirmation of the Weyl nature of tr-PtBi$_2$. A more complete study of the in-plane magnetoresistance and PHE in nano-structures, at higher magnetic fields, should also be conducted in order to determine more accurately the field dependence of the different contributions to the in-plane oscillations of the resistance. It would also be interesting to measure structures of different thicknesses to determine if these contributions, or their relative amplitudes, are thickness dependent, as suggested by our initial measurements.

In addition to these well understood properties, we measured in nano-structures a non-symmetric hysteresis in the magnetic field transition, which results in the superconductivity persisting sometimes well above the critical magnetic field when the field is swept in a particular direction, with a large heat release occurring at the superconducting-to-normal-state transition. While we have characterized it experimentally, a theoretical understanding of this feature and its origin is still lacking, and further investigation is necessary to fully understand it.

The van der Waals nature of tr-$PtBi_2$ opens up many possibilities of interesting studies by designing suitable heterostructures with e.g. electrostatic gates or other materials. For instance, it would be possible to study the formation of vortices and antivortices around the BKT transition in a flake of tr-$PtBi_2$ by stacking on it a thin flake of WTe_2 (separated by an insulating few-layer h-BN) acting as a highly sensitive magnetic field sensor.

The most important question raised by our study, and by other experiments not reported in this manuscript, regards the nature of the superconductivity in macroscopic single crystals of tr-$PtBi_2$, with charge transport results coherent with the 3D Ginzburg-Landau theory despite no sign of bulk superconductivity from heat transport measurements, indicating that most of the volume remains in the normal state, even at low temperature. These results point toward a possible percolative nature of the superconducting state in macro-structures of tr-$PtBi_2$, which needs to be investigated.

This hypothesis is comforted by recent simulations we conducted of percolating transport in nano-structures in the presence of inhomogeneities. These preliminary results could qualitatively reproduce many features we observed in our measurements, including the presence of multiple steps in superconducting transitions, and might help us understand the nature of the superconductivity in bulk crystals.

Appendices

A | Topology and Band structure

A.1 Quantum spin Hall effect

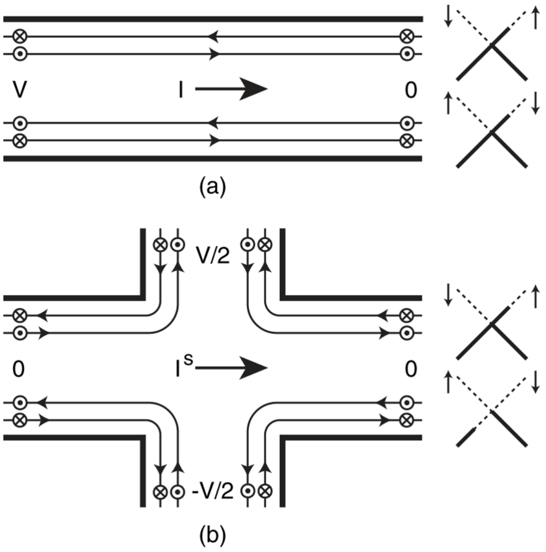

Figure A.1: Schematic drawing showing edge channels in a QSH insulator, in the two-terminal (a) and four-terminal (b) geometries. The diagrams on the right side indicate how the edge states are populated. Adapted from Kane and Mele [2005]

At low temperature, a very large spin-orbit coupling converts graphene from a semi-metallic system to a quantum spin Hall (QSH) insulator, in the absence of external magnetic field. In this state, the bulk of the graphene sheet is gaped, and gapless edge states appear at the edges of the sample, similarly to the quantum Hall effect (QHE). These edge states support the transport of charges, as well as the transport of spin. In a two-terminal configuration (see Fig.A.1.a), a charge current I flows along the direction of an applied electric field. When an electric field is applied in a four-terminal configuration (Fig.A.1.b) however, a spin current I^S develops perpendicularly to the applied field. This geometry can also be used to measure spin currents, as such a current injected from the left to the right lead results in a voltage developing between the top and bottom leads.

A.2 Band Structure calculation

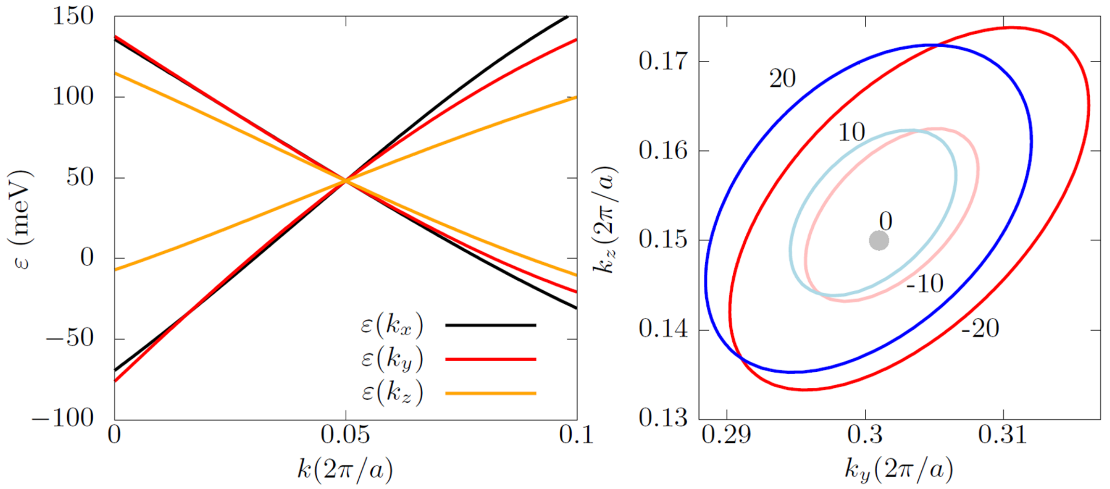

Figure A.2: Left: Energy dispersion around the Weyl point, along the three cartesian directions. The Weyl cone is weakly canted. Right: Isoenergetic contours around the Weyl point, at 0meV, ±10meV and ±20meV with respect to the Weyl point energy. The isoenergetic contours reduce to a single point at 0meV, as expected for a type-I Weyl node.

Fig.A.2 shows the energy dispersion around the Weyl node along the three cartesian directions (left) as well as the isoenergetic contours around the Weyl node (right) for different energies. The energy dispersion shows that the Weyl cones are only slightly canted, indicating that the Weyl node is of type-I. This is confirmed by the isoenergetic contours, which reduce to a single point at the Weyl node energy. Away from that energy, the cones are anisotropic in the (k_y, k_z) plane, as indicated by the ellipsoidal shape isoenergetic contours. Further below the Weyl node energy, at about 15 meV above the Fermi energy, the Weyl cones merge with a larger pocket from the same band (see Fig.A.3). Fig.A.4 shows the existence of Fermi arcs in tr-PtBi$_2$'s surface band structure, for both Bi$_2$- and Bi$_4$- terminated surfaces.

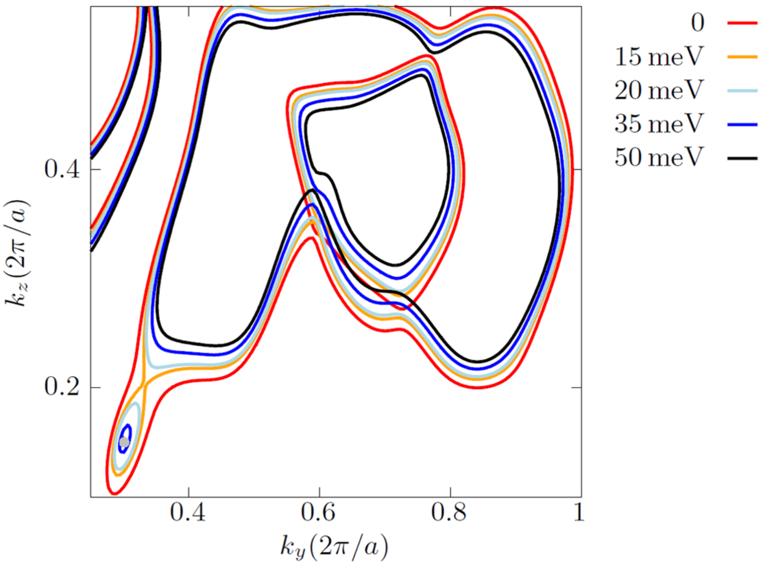

Figure A.3: Isoenergetic contours of the band associated with the Weyl node, with 0meV (red line) corresponding to the Fermi energy. The Weyl cone merges with a larger pocket at about 15meV above the Fermi energy.

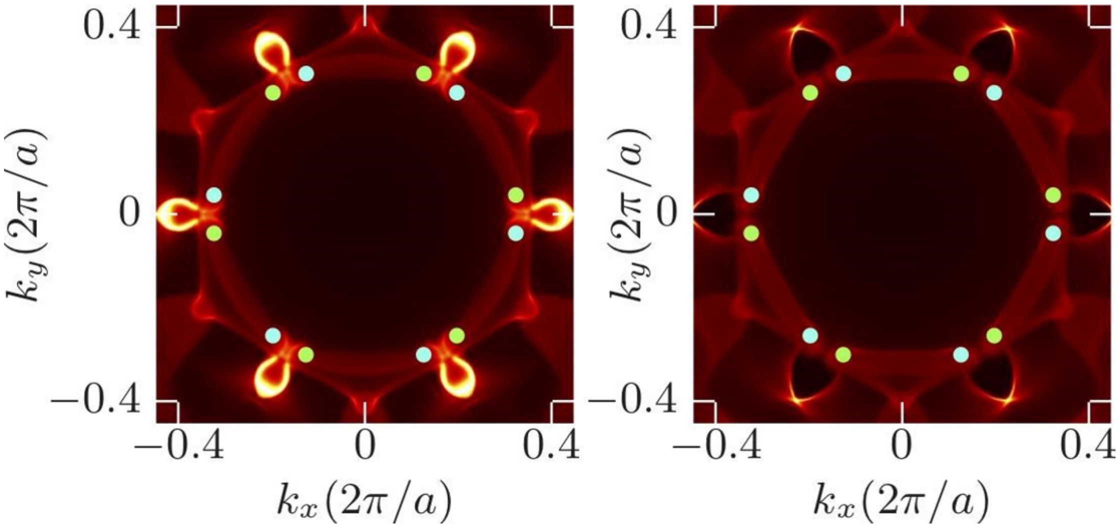

Figure A.4: Fermi surface corresponding to the Weyl node energy, for a Bi_2-terminated surface (left) and Bi_4-terminated surface (right). The Weyl points are represented by green (positive chirality) and blue (negative chirality) points.

B | Magnetotransport

B.1 Magnetoresistance

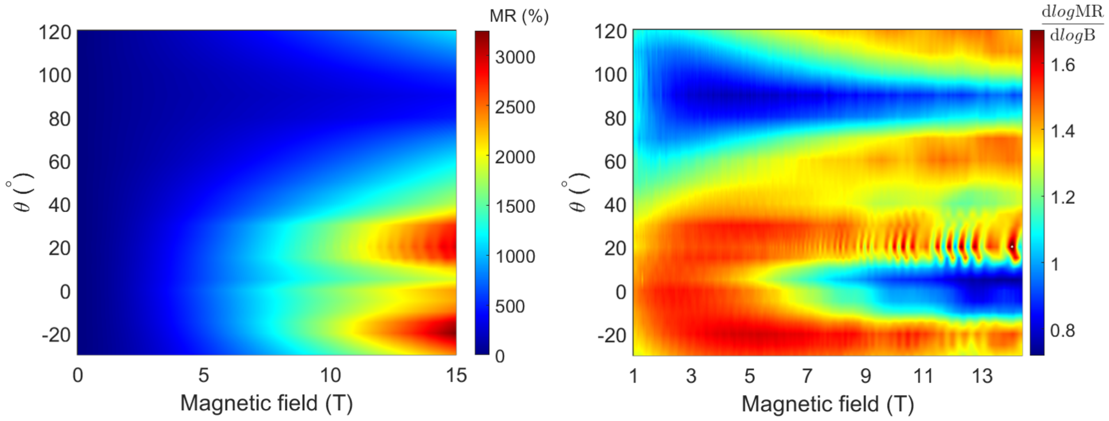

(a) (b)

Figure B.1: Angular dependence of the magnetoresistance of the macro-structure MS1 (a) and its logarithmic derivative (b) at 5K.

Fig.B.1a shows the full angular dependence of the magnetoresistance (MR) of MS1, at 5K, and its logarithmic derivative is shown in Fig.B.1b, which represents the power low exponent of the MR. The reduction of MR is clearly visible around $\theta = 0°$ in both figures.

B.2 Schubnikhov-de-Haas Oscillations

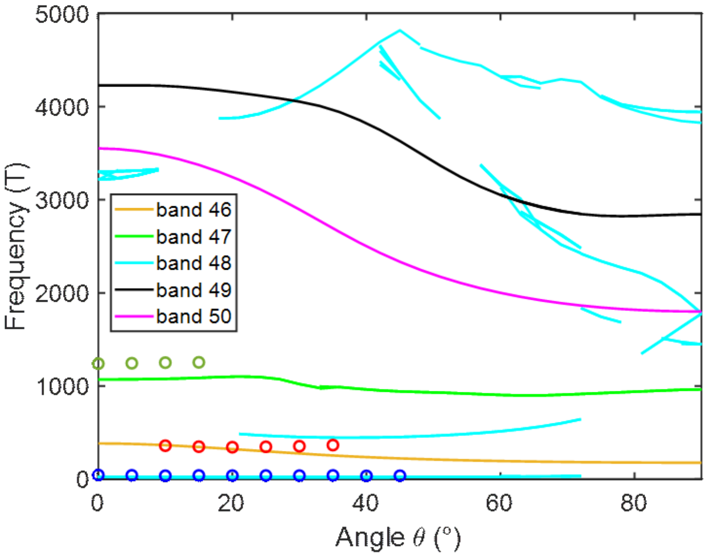

Figure B.2: Angular dependence of the quantum oscillation frequencies associated with each band. Experimental frequencies are represented in red (α pocket), green (β pocket) and blue (γ pocket) circles.

The angular dependence of the quantum oscillations frequencies of every band found in our DFT band structure calculation is shown in Fig.B.2, along with our experimental measurements. Bands 46 and 47 where already presented in the main text, as well as part of the oscillation frequencies from band 48 (associated with the Weyl nodes). Two additional bands are expected to contribute to quantum oscillations, albeit at frequencies inaccessible with our magnetic fields (above 2000T in the angular range in which quantum oscillations were measured).

B.3 Temperature dependence of Shubnikov–de Haas oscillations

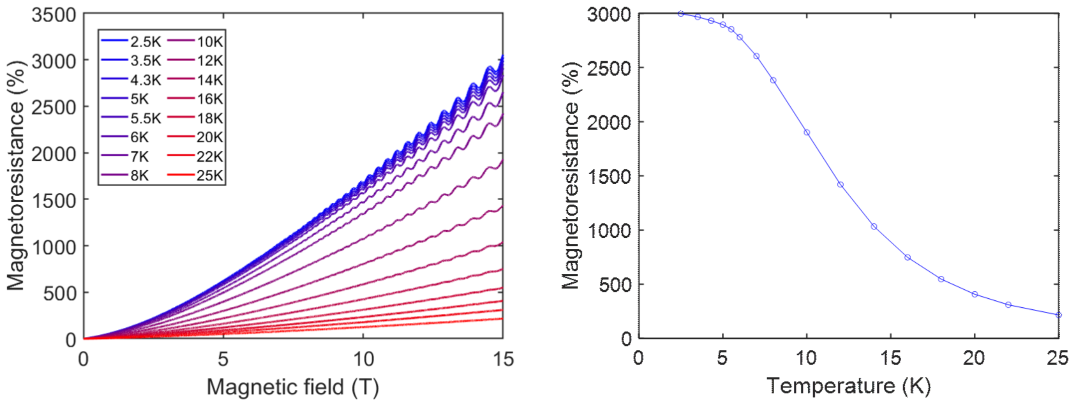

(a) (b)

Figure B.3: (a) Magnetoresistance of MS1 at $\theta = 20°$, at different temperatures from 2.5K to 25K. (b) Temperature dependence of the magnetoresistance at 15T, extracted from (a).

Fig.B.3a shows the magnetoresistance of MS1 at $\theta = 20°$ with increasing temperatures, up to 25K. The amplitude of the magnetoresistance decreases with temperature (see Fig.B.3b), as well as the amplitude of Shubnikov–de Haas oscillations (SdHo). After removing the MR background (Fig.B.4a), it is visible that multiple frequencies contribute to the oscillations. Fig.B.4c, B.4b and B.4d show the results of filtering the oscillations around the frequencies identified experimentally for each band. Only the filtered oscillations associated with the α pocket appear to come from a single frequency. The amplitude of the SdH peak at $1/B = 0.08\text{T}^{-1}$, extracted from Fig.B.4c, is shown in Fig.B.5a. The amplitude shows a saturation at low temperature, which is not linked to a saturation of the electronic temperature (as can be seen in Fig.B.3a), and cannot be fitted correctly by the LK formula over the entire temperature range. A best fit yields an effective mass $m^* = 0.18m_e$, with m_e the electron mass. However, if we reproduce this analysis for each SdH peak at different magnetic fields, we find that the effective mass is not constant with magnetic field (Fig.B.5b), which is not consistent with the LK theory for a single band.

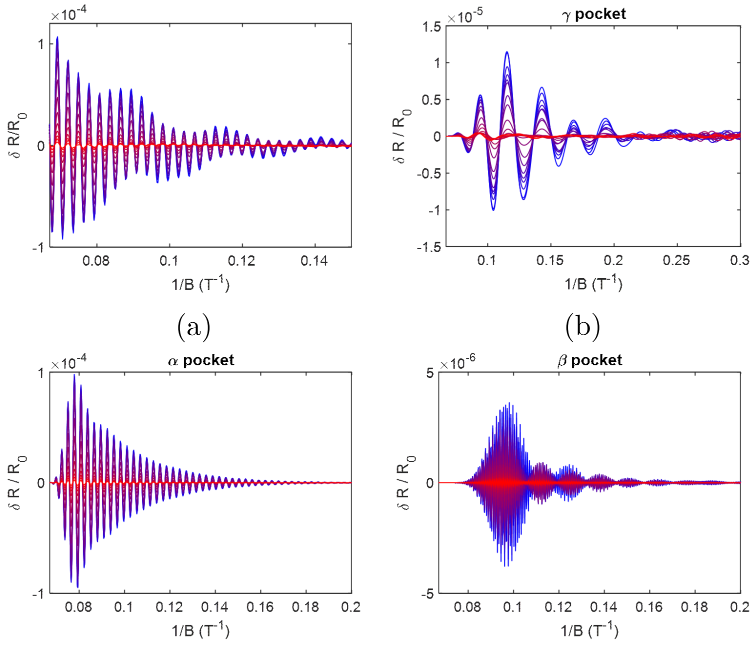

(a) (b)

(c) (d)

Figure B.4: Shubnikov–de Haas oscillations at $\theta = 20°$ extracted from Fig.B.3a, with the same color code for temperature (a). (b)-(d) show the oscillations of (a) filtered around the frequencies identified for each pocket.

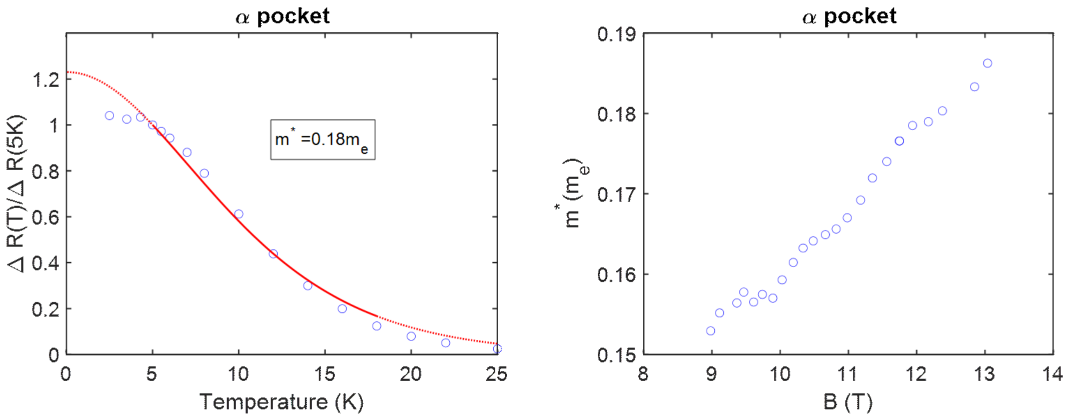

(a) (b)

Figure B.5: (a) Temperature dependence of the relative amplitude of the SdHo peak at $1/B = 0.08\text{T}^{-1}$ (blue circles) for the α pocket. The red line shows the LK fit attempt (over the full-line temperature range), yielding $m^* = 0.18m_e$. (b) Field dependence of m^* extracted for each SdHo visible peak, with the same analysis as in (a).

B.4 Planar Hall effect in S3

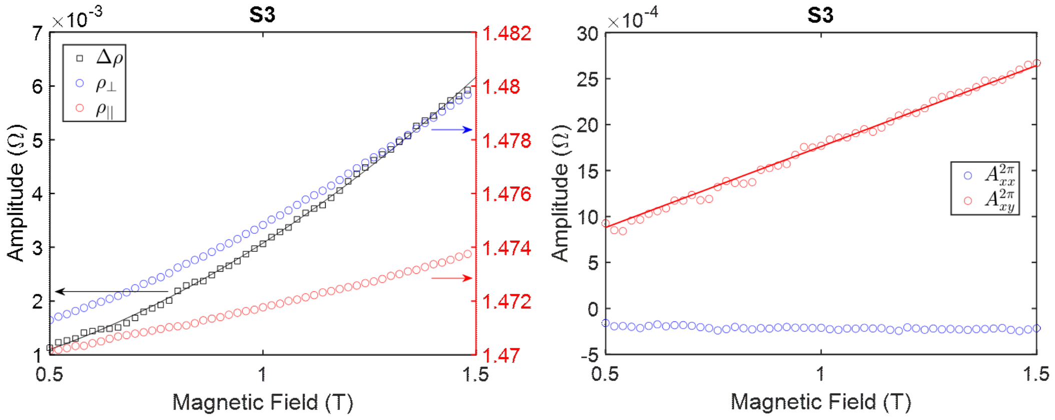

(a) (b)

Figure B.6: (a) Field dependence of the π-periodic signal's amplitude $\Delta\rho = \rho_\perp - \rho_{||}$ in S3, corresponding to the planar Hall effect (in black). It is fitted with a power law $\Delta\rho \propto B^{1.87}$ (black line). The right axis shows amplitudes of $\rho_\perp$ and $\rho_{||}$, respectively in blue and red. (b) Field dependence of the amplitude of the 2π-periodic signal (anomalous planar Hall effect) in the longitudinal (blue) and transverse (red) resistances.

In addition to nano-structure S5, we studied the variation of the resistance of S3 when rotating the magnetic field in the structure's plane. We performed the same analysis as for S5 (main text) and fitted the angular variations of the longitudinal and transverse resistances with eq.3.2. The amplitude of the π-periodic signal (planar Hall effect) shows an almost quadratic dependence on the magnetic field (see Fig.B.6a), with $\Delta\rho \propto B^{1.87}$, compared to an almost linear dependence for S5 ($\Delta\rho \propto B^{1.15}$). Nonetheless, the amplitudes of the 2π-periodic oscillations (Fig.B.6b) is very similar to that of S5, with a linear dependence for the transverse resistance and an almost-zero, constant amplitude for the longitudinal resistance.

C | Superconductivity

C.1 Macro-structures

C.1.1 Critical magnetic field

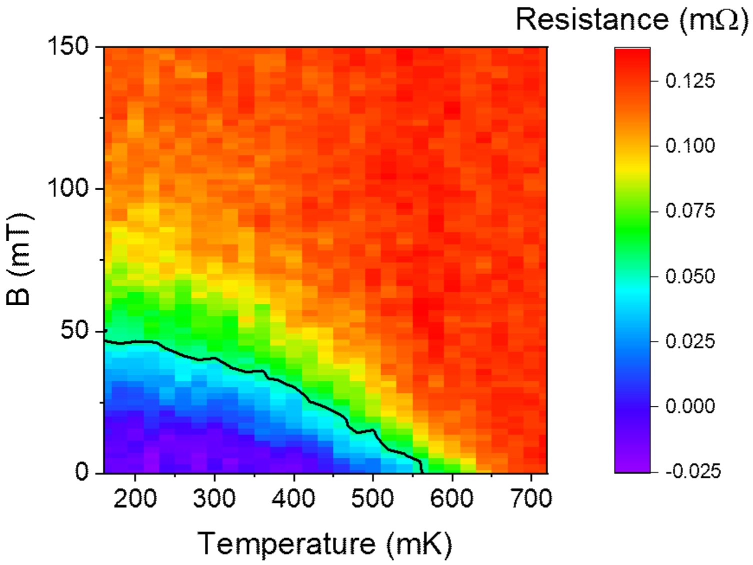

Figure C.1: Two-dimensional mapping of the resistance versus magnetic field and temperature for MS2, obtained by sweeping an in-plane magnetic field from 0T to 0.5T at constant temperature, increasing the temperature in steps. The black line corresponds to $R(B) = R_N/2$.

To obtain the temperature dependence of the in-plane critical magnetic field, we measured the resistance of MS2 by sweeping the field from 0T to 500mT and back, at fixed temperature. The temperature was then increased in steps of 20mK, from 150mK to 750mK, and we repeated the field sweep measurements once the sample's temperature had stabilized (see Fig.C.1). The critical field B_c at each temperature is defined by $R(B_c) = R_N/2$, with R_N the resistance in the normal state (black line). No significant differences are found between the two sweep directions.

C.1.2 Point-Contact Measurements

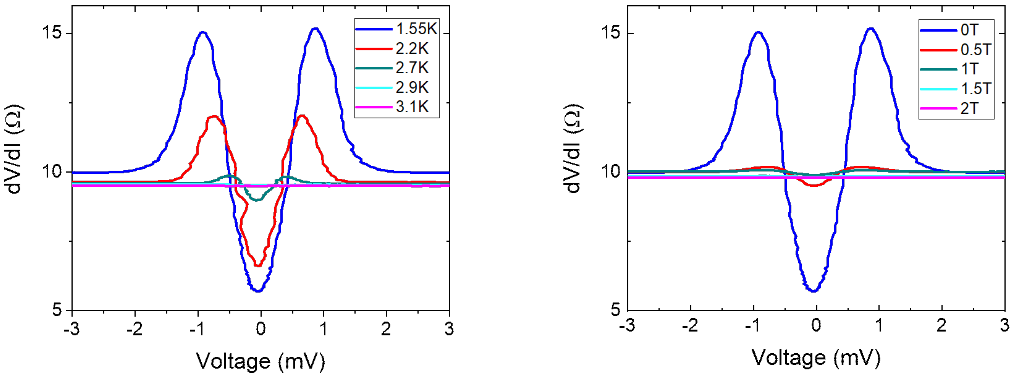

(a)

(b)

Figure C.2: (a) Differential resistance dV/dI as a function of the applied voltage, for different temperatures, measured in point-contact. Signs of superconductivity (a deviation from Ohm's law) are visible up to 2.7K, a large increase compared to measurements without pressure. (b) Point-contact differential resistance as a function of the applied voltage, for different applied magnetic fields and at 1.55K. Signs of superconductivity are still visible at $B = 0.5T$, almost an order of magnitude larger than the critical field measured at ambient pressure in MS2.

Point contact spectroscopy measurements on macroscopic crystals were realized by Dr. Dima Bashlakov of ILTPE in Kharkiv, Ukraine. For point contact measurements, the crystals are contacted to an electrical circuit on one side, which is closed on the other side by pressing on the crystal with a wire made of a noble metal (Cu, Ag or Au). This measurement techniques thus applies local pressure to the sample under the contact.

Point contact measurements on tr-PtBi$_2$ indicate that the critical temperature increases, likely due to local pressure, similarly to tr-MoTe$_2$ [Naidyuk et al., 2018], as can be seen in Fig.C.2a. The differential resistance dV/dI, which saturates at the normal resistance R_N at high bias voltage (when the sample is in the normal state), drops to almost $R_N/2$ at $T = 1.55K \sim 2.5 \times T_c$, with T_c the critical temperature measured at ambient pressure in MS2. The drop in resistance, which indicates at least a partial condensation of the carriers, is still visible at temperatures as high as 2.9K, or almost 5 times the critical temperature at ambient pressure.

Samples were also measured in point contact under an external magnetic field, at $T = 1.55K$ (Fig.C.2b). At this temperature, the samples still shows signs of superconductivity even at $B = 500mT$, about 10 times the critical field at ambient pressure. This shows that superconductivity in bulk tr-PtBi$_2$ is greatly enhanced under pressure, similarly to previously reported results [Wang et al., 2021].

C.2 Nano-structures

C.2.1 Dimensionality of the superconductivity

In this section, we present results on the dimensionality of the superconductivity in nano-structures for another contact configuration, as well as the full mapping data we used for this analysis. Fig.C.3 shows the temperature dependence of in- and out-of-plane critical magnetic fields for another contact configuration on S1. The overall behavior of the resistance is the same, and is well fitted by the 2D Ginzburg-Landau theory with misalignment. The out-of-plane critical field shows a linear temperature dependence with again a change of slope, albeit at a slightly larger temperature than for configuration V0 (320mK instead of 300mK). These two slopes correspond to $T_c = 383\text{mK}$ and $\xi_0 = 180\text{nm}$ for the low temperature slope ($T \leq 315\text{mK}$), and $T_c = 376\text{mK}$ and $\xi_0 = 172\text{nm}$ for the high temperature slope ($T \geq 320\text{mK}$). The in-plane critical field fit yields $T_c = 358\text{mK}$, $d_{SC} = 38\text{nm}$ and $\xi_0^{||} = 136\text{nm}$. These parameters are very close to those obtained previously for

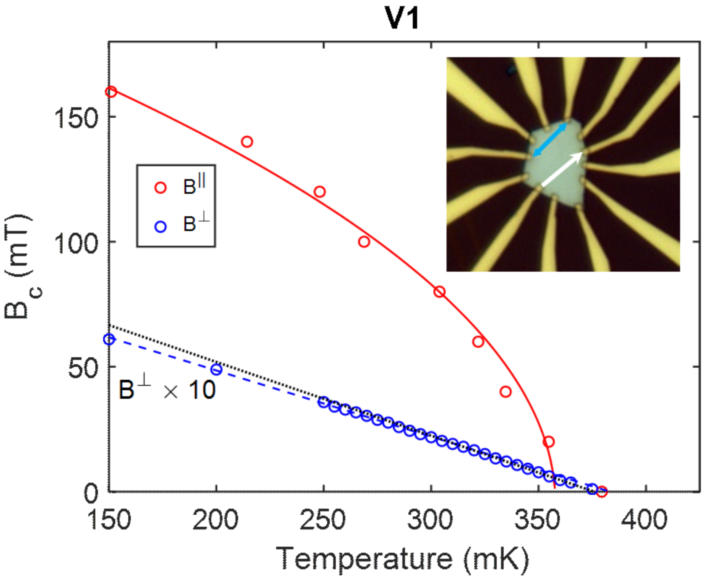

Figure C.3: Temperature dependence of the critical magnetic field for V1, both in- and out-of-plane (red and blue respectively), extracted from Fig.C.5b. The out-of-plane field was increased by an order of magnitude for visibility. The data was fitted with a misalignment-corrected 2D Ginzburg-Landau model. For the out-of-plane critical field, two fits were done: from 150mK to 315mK in dashed blue, and from 320mK to T_c in dotted black.

V0. Given that the contacts of both configurations are located on opposite sides of the sample, with respect to the current source and drain, the minor differences could originate from spatial inhomogeneities in the sample itself.

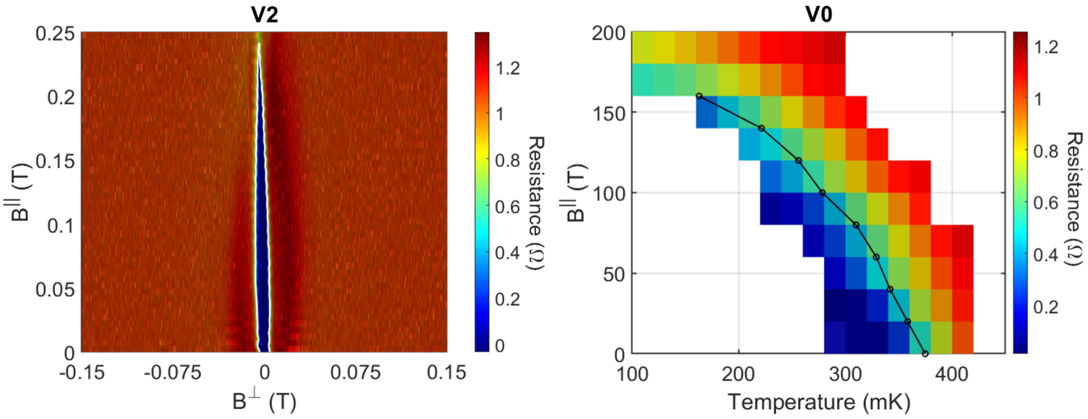

(a) (b)

Figure C.4: (a) Two-dimensional magnetic field mapping (in- and out-of-plane) for contact configuration V2 (see Fig.4.10b, inset), at 100mK. The contour at $R_N/2$ is marked by a white line. (b) Mapping of the resistance of configuration V0 with in-plane magnetic field and temperature. The black line corresponds to $R_N/2$.

To extract the angular dependence of the critical magnetic field, we measured the resistance while sweeping the out-of-plane field, at constant in-plane field. The in-plane field was increased in steps of 5mT, up to 250mT. The critical field corresponds to $R(B_c) = R_N/2$ (Fig.C.4a and Fig.C.5a). The out-of-plane field is swept at constant in-plane field to avoid hysteresis issues related to metastabilities. For the same reason, in order to measure the temperature dependence of the in-plane critical field, we swept the temperature at constant field, and increased the in-plane field in steps of 20mT (Fig.C.4b and Fig.C.5b).

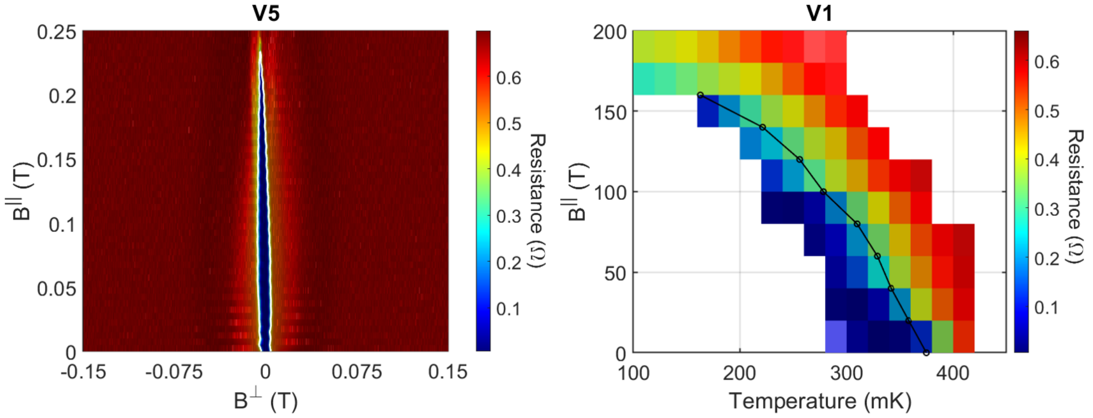

(a) (b)

Figure C.5: (a) Two-dimensional magnetic field mapping (in- and out-of-plane) for contact configuration V5 (see Fig.4.12, inset), at 100mK. The contour at $R_N/2$ is marked by a white line. (b) Mapping of the resistance of configuration V1 with in-plane magnetic field and temperature. The black line corresponds to $R_N/2$.

C.2.2 Berezinskii–Kosterlitz–Thouless transition

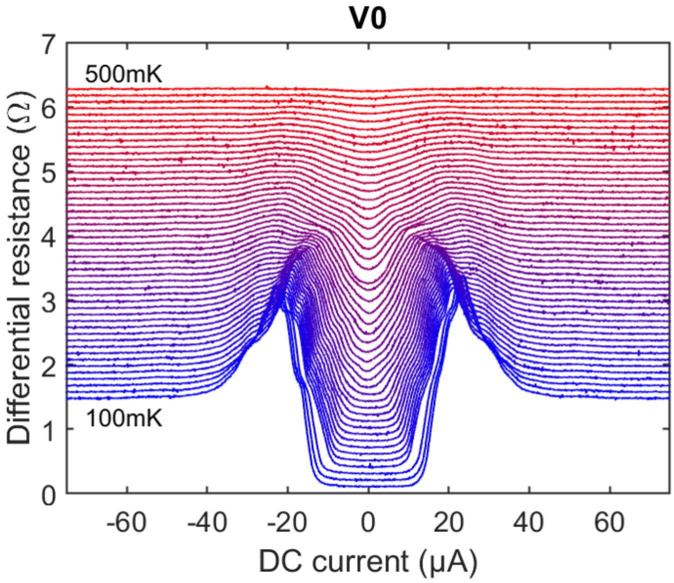

Figure C.6: Differential resistance (dV/dI) of configuration V0 measured at fixed temperature, from 100mK to 500mK in steps of 10mK. A magnetic field of 2.4G was applied to compensate for remanent fields. The curves are shifted vertically for visibility.

In order to measure the DC current dependence of the voltage V(I) in our samples, we used our lock-in amplifiers to measure the differential resistance dV/dI by applying DC and AC currents simultaneously, before integrating it to recover the V(I) characteristic. These measurements were done at multiple temperatures between 100mK and 500mK (see Fig.C.6), in order to evidence a Berezinskii–Kosterlitz–Thouless (BKT) transition. The $I_{DC} = 0$A points were also used to obtain the temperature dependence of the resistance.

Since the V(I) power law is exactly $a(T_{BKT}) = 3$ at the BKT transition temperature, we extracted the power law exponent $a(T)$ from our V(I) measurements (Fig.C.6) by taking their logarithmic derivative: $a(T,I) = \left.\frac{d log(V)}{d log(I)}\right|_T$. The results at all temperatures are represented in Fig.C.7a and C.7b.

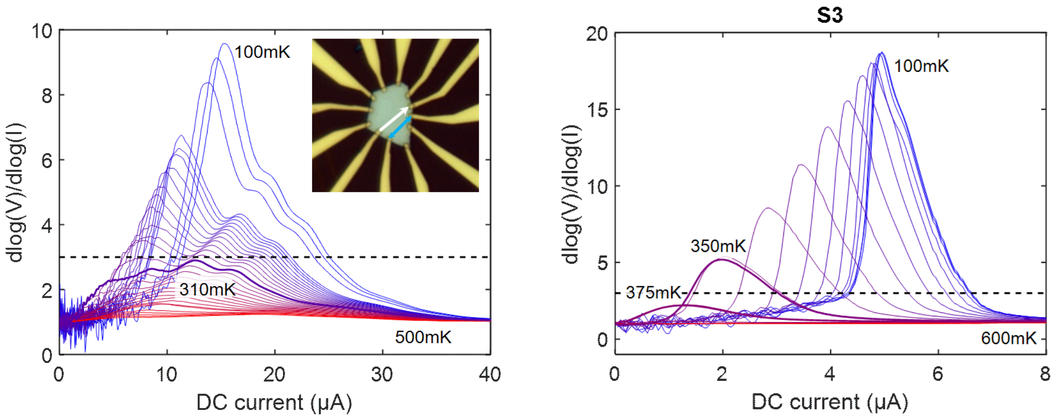

(a) (b)

Figure C.7: Logarithm derivative of the V(I) characteristics at different temperatures for S1 (a) and S3 (b). The temperatures for which the maximum is closest to 3 (corresponding the the BKT temperature) are shown as thicker lines.

C.2.3 Inhomogeneous superconducting transitions

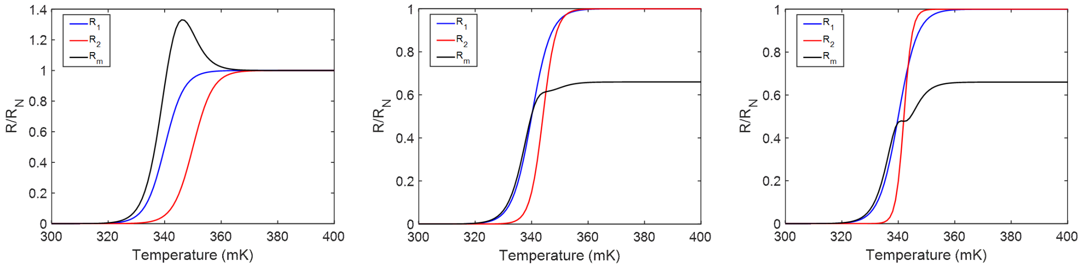

(a) (b) (c)

Figure C.8: Measured resistance R_m (in black) obtained for R_1 and R_2 (in blue and red, respectively) in three different cases. The two transitions are described by a second-order transition, with $A_1 = 1$, $a_1 = 100$ and $T_{c1} = 340$mK for R_1. R_2's parameters are $A_2 = 1$; $a_2 = 100$; $T_{c2} = 350$mK (a), $A_2 = 1$; $a_2 = 240$; $T_{c2} = 342$mK (b) and $A_2 = 1$; $a_2 = 150$; $T_{c2} = 344$mK (c). R_m is reduced by 1/3 in (b) and (c) for visibility.

We performed the same simulations as in section 4.3.4 by replacing the BKT transition R(T) with a simple second order model given by

$$R(T) = \frac{A}{1 + e^{-a\frac{T-T_c}{T_c}}}. \tag{C.1}$$

Using this model, we can qualitatively reproduce the three different behaviors of $R_m = \frac{V}{I} = \frac{R_1^2}{2(R_1^2+R_2^2)}$ discussed in section 4.3.4: a resistance peak, a change of slope in the transition and a step in the transition (see Fig.C.8). The main difference in this model between the second-order and BKT transitions is the absence in the former of the small depression of resistance following the peak, which is present in the latter and which we measured in our samples.

We observed these deviations from the standard superconducting transitions (see sec.4.3.4) in all our samples, in both temperature and field: in Fig.C.9, which shows the in-plane field dependence of the normalized resistance of S4, the transition shows both a sudden change of slope (at $B_{||} \sim 100$mT) and a resistance peak (at $B_{||} \sim 250$mT)

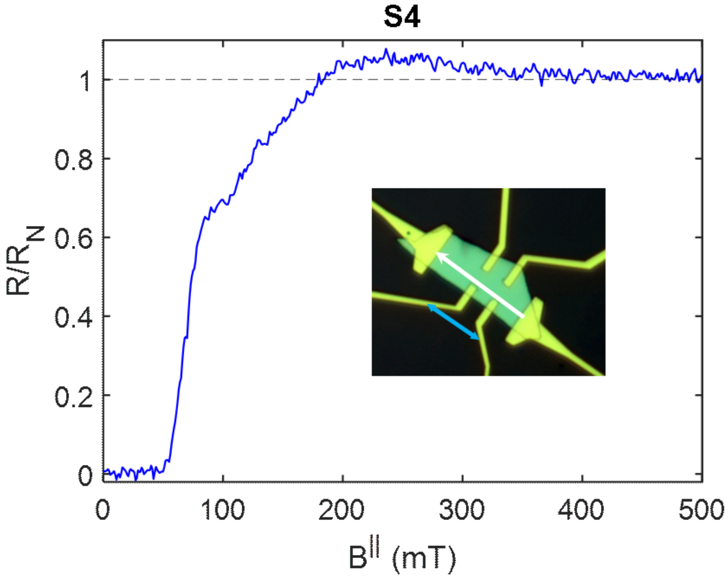

Figure C.9: Reduced resistance of sample S4 in an in-plane magnetic field.

Acknowledgments

I want to end this manuscript by thanking the people who have made this work possible, and those who have provided me with support and numerous pleasant memories.

I would like to thank Prof. Dr. Büchner for giving me the opportunity, and the funds, to do my doctorate in his institute, and for the the trust he put in me for designing and building the encapsulation transfer station. My thanks also extend to Kerstin Höllerer, Rita Taubert and Aline Leue for always helping me with administrative issues during the PhD.

Thank you to Joseph for supervising and helping me with my projects, and thanks to Louis for his very important help during the entire PhD, and especially regarding the design of the transfer station. Thank you to Jorge, Steffen, Jeroen and Carmine for their theoretical help, and for the very insightful conversations we had.

I would like to Patrizia for her friendship, support and help during and since our difficult PhD representative tenure. These times were stressful and uncertain, but together we managed to do what needed to be done, and even have some fun in the process!

I would like to thank Michaela for the nice discussions and long walks we shared, as well as for feeling less alone in being a short climber in the land of giants.

Thank you to all from the bouldering/climbing group for the nice sessions in the gym, as well as the outdoor excursions around Dresden. Thank you to Titouan, Burak, Kirill and Vira, my office-mates, colleagues and friends for the support and help, inside and outside the lab.

Keeping the most important for last, I would like to thank Teresa for making the office and the lab a place I wanted to come to every day. I couldn't have wished for a better colleague and office-mate! Outside the lab, thank you and Daniel for making me discover the joy of biking, re-discover my passion for bouldering and

climbing, and giving many opportunities to enjoy them!

Bibliography

S. L. Adler. Axial-Vector Vertex in Spinor Electrodynamics. *Physical Review*, 177 (5):2426–2438, jan 1969. ISSN 0031-899X.

M. N. Ali, J. Xiong, S. Flynn, J. Tao, Q. D. Gibson, L. M. Schoop, T. Liang, N. Haldolaarachchige, M. Hirschberger, N. P. Ong, and R. J. Cava. Large, non-saturating magnetoresistance in WTe2. *Nature*, 514(7521):205–208, oct 2014. ISSN 0028-0836.

N. P. Armitage, E. J. Mele, and A. Vishwanath. Weyl and Dirac semimetals in three-dimensional solids. *Reviews of Modern Physics*, 90(1):15001, 2018. ISSN 15390756.

J. Bardeen, L. N. Cooper, and J. R. Schrieffer. Theory of Superconductivity. *Physical Review*, 108(5):1175–1204, dec 1957. ISSN 0031-899X.

R. Battilomo, N. Scopigno, and C. Ortix. Anomalous planar Hall effect in two-dimensional trigonal crystals. *Physical Review Research*, 3(1):1–6, 2021. ISSN 2643-1564.

J. S. Bell and R. Jackiw. A PCAC puzzle: $\pi 0 \rightarrow \gamma\gamma$ in the σ-model. *Il Nuovo Cimento A*, 60(1):47–61, 1969. ISSN 0369-3546.

L. Benfatto, C. Castellani, and T. Giamarchi. Broadening of the Berezinskii-Kosterlitz-Thouless superconducting transition by inhomogeneity and finite-size effects. *Physical Review B - Condensed Matter and Materials Physics*, 80(21): 1–11, 2009. ISSN 10980121.

V. L. Berezinsky. Destruction of long range order in one-dimensional and two-dimensional systems having a continuous symmetry group. I. Classical systems. *Sov. Phys. JETP*, 32:493–500, 1971.

B. A. Bernevig, T. L. Hughes, and S.-C. Zhang. Quantum Spin Hall Effect and Topological Phase Transition in HgTe Quantum Wells. *Science*, 314(5806):1757–1761, dec 2006. ISSN 0036-8075.

M. Bowen, K.-J. Friedland, J. Herfort, H.-P. Schönherr, and K. H. Ploog. Order-driven contribution to the planar Hall effect in Fe3Si thin films. *Physical Review B*, 71(17):172401, may 2005. ISSN 1098-0121.

A. A. Burkov. Chiral anomaly and transport in Weyl metals. *Journal of Physics Condensed Matter*, 27(11), 2015. ISSN 1361648X.

A. A. Burkov. Giant planar Hall effect in topological metals. *Physical Review B*, 96(4):041110, jul 2017. ISSN 2469-9950.

Y. Cao, V. Fatemi, S. Fang, K. Watanabe, T. Taniguchi, E. Kaxiras, and P. Jarillo-Herrero. Unconventional superconductivity in magic-angle graphene superlattices. *Nature*, 556(7699):43–50, 2018. ISSN 14764687.

G. Chang, S. Y. Xu, H. Zheng, C. C. Lee, S. M. Huang, I. Belopolski, D. S. Sanchez, G. Bian, N. Alidoust, T. R. Chang, C. H. Hsu, H. T. Jeng, A. Bansil, H. Lin, and M. Z. Hasan. Signatures of Fermi Arcs in the Quasiparticle Interferences of the Weyl Semimetals TaAs and NbP. *Physical Review Letters*, 116(6):1–6, 2016. ISSN 10797114.

X. Chen, D. Shao, C. Gu, Y. Zhou, C. An, Y. Zhou, X. Zhu, T. Chen, M. Tian, J. Sun, and Z. Yang. Pressure-induced multiband superconductivity in pyrite PtB i2 with perfect electron-hole compensation. *Physical Review Materials*, 2 (5):1–8, 2018. ISSN 24759953.

L. N. Cooper. Bound Electron Pairs in a Degenerate Fermi Gas. *Physical Review*, 104(4):1189–1190, nov 1956. ISSN 0031-899X.

W. S. Corak, B. B. Goodman, C. B. Satterthwaite, and A. Wexler. Exponential Temperature Dependence of the Electronic Specific Heat of Superconducting Vanadium. *Physical Review*, 96(5):1442–1444, dec 1954. ISSN 0031-899X.

A. T. De Waele. Basic operation of cryocoolers and related thermal machines. *Journal of Low Temperature Physics*, 164(5-6):179–236, 2011. ISSN 00222291.

A. Devarakonda, H. Inoue, S. Fang, C. Ozsoy-Keskinbora, T. Suzuki, M. Kriener, L. Fu, E. Kaxiras, D. C. Bell, and J. G. Checkelsky. Clean 2D superconductivity in a bulk van der waals superlattice. *Science*, 370(6513):231–237, 2020. ISSN 10959203.

P. Dirac. The quantum theory of the electron. *Proceedings of the Royal Society of London. Series A, Containing Papers of a Mathematical and Physical Character*, 117(778):610–624, feb 1928. ISSN 0950-1207.

J. Dufouleur, E. Xypakis, B. Büchner, R. Giraud, and J. H. Bardarson. Suppression of scattering in quantum confined 2D helical Dirac systems. *Physical Review B*, 97(7):075401, feb 2018. ISSN 2469-9950.

V. Fatemi, S. Wu, Y. Cao, L. Bretheau, Q. D. Gibson, K. Watanabe, T. Taniguchi, R. J. Cava, and P. Jarillo-Herrero. Electrically tunable low-density superconductivity in a monolayer topological insulator. *Science*, 362(6417):926–929, 2018. ISSN 10959203.

J. Feng, Y. Pang, D. Wu, Z. Wang, H. Weng, J. Li, X. Dai, Z. Fang, Y. Shi, and L. Lu. Large linear magnetoresistance in Dirac semimetal Cd3As2 with Fermi surfaces close to the Dirac points. *Physical Review B - Condensed Matter and Materials Physics*, 92(8):1–5, 2015. ISSN 1550235X.

Y. Feng, Q. Jiang, B. Feng, M. Yang, T. Xu, W. Liu, X. Yang, M. Arita, E. F. Schwier, K. Shimada, H. O. Jeschke, R. Thomale, Y. Shi, X. Wu, S. Xiao, S. Qiao, and S. He. Rashba-like spin splitting along three momentum directions in trigonal layered PtBi2. *Nature Communications*, 10(1):1–8, 2019. ISSN 20411723.

S. M. Frolov, M. J. Manfra, and J. D. Sau. Topological superconductivity in hybrid devices. *Nature Physics*, 16(7):718–724, 2020. ISSN 17452481.

L. Fu, C. L. Kane, and E. J. Mele. Topological insulators in three dimensions. *Physical Review Letters*, 98(10), 2007. ISSN 00319007.

P. Fulde and R. A. Ferrell. Superconductivity in a strong spin-exchange field. *Physical Review*, 135(3A), 1964. ISSN 0031899X.

W. Gao, N. Hao, F. W. Zheng, W. Ning, M. Wu, X. Zhu, G. Zheng, J. Zhang, J. Lu, H. Zhang, C. Xi, J. Yang, H. Du, P. Zhang, Y. Zhang, and M. Tian. Extremely Large Magnetoresistance in a Topological Semimetal Candidate Pyrite PtBi2. *Physical Review Letters*, 118(25):1–5, 2017. ISSN 10797114.

W. Gao, X. Zhu, F. Zheng, M. Wu, J. Zhang, C. Xi, P. Zhang, Y. Zhang, N. Hao, W. Ning, and M. Tian. A possible candidate for triply degenerate point fermions in trigonal layered PtBi2. *Nature Communications*, 9(1):1–8, 2018. ISSN 20411723.

Q. D. Gibson, L. M. Schoop, L. Muechler, L. S. Xie, M. Hirschberger, N. P. Ong, R. Car, and R. J. Cava. Three-dimensional Dirac semimetals: Design principles and predictions of new materials. *Physical Review B - Condensed Matter and Materials Physics*, 91(20):1–11, 2015. ISSN 1550235X.

J. G. Gluschke, J. Seidl, H. H. Tan, C. Jagadish, P. Caroff, and A. P. Micolich. Impact of invasive metal probes on Hall measurements in semiconductor nanostructures. *Nanoscale*, 12(39):20317–20325, 2020. ISSN 20403372.

L. P. Gor'kov. Microscopic derivation of the Ginzburg–Landau equations in the theory of superconductivity. *Sov. Phys. - JETP (Engl. Transl.); (United States)*, 1959.

B. I. Halperin and D. R. Nelson. Resistive transition in superconducting films. *Journal of Low Temperature Physics*, 36(5-6):599–616, sep 1979. ISSN 0022-2291.

M. Z. Hasan and C. L. Kane. Colloquium: Topological insulators. *Reviews of Modern Physics*, 82(4):3045–3067, 2010. ISSN 00346861.

X. Huang, L. Zhao, Y. Long, P. Wang, D. Chen, Z. Yang, H. Liang, M. Xue, H. Weng, Z. Fang, X. Dai, and G. Chen. Observation of the chiral-anomaly-induced negative magnetoresistance: In 3D Weyl semimetal TaAs. *Physical Review X*, 5(3):1–9, 2015. ISSN 21603308.

W. Jiang, F. Zhu, P. Li, Y. Li, G. Wang, Q. Jing, W. Gao, M. Tian, J. Ma, W. Zhang, W. Luo, and D. Qian. Electronic structure of non-centrosymmetric PtBi 2 studied by angle-resolved photoemission spectroscopy. *Journal of Applied Physics*, 128(13):135103, oct 2020. ISSN 0021-8979.

C. L. Kane and E. J. Mele. Quantum Spin hall effect in graphene. *Physical Review Letters*, 95(22):1–4, 2005. ISSN 00319007.

M. Kargarian, M. Randeria, and Y. M. Lu. Are the surface Fermi arcs in Dirac semimetals topologically protected? *Proceedings of the National Academy of Sciences of the United States of America*, 113(31):8648–8652, 2016. ISSN 10916490.

K. v. Klitzing, G. Dorda, and M. Pepper. New Method for High-Accuracy Determination of the Fine-Structure Constant Based on Quantized Hall Resistance. *Physical Review Letters*, 45(6):494–497, aug 1980. ISSN 0031-9007.

M. Konig, S. Wiedmann, C. Brune, A. Roth, H. Buhmann, L. W. Molenkamp, X.-l. Qi, and S.-c. Zhang. Quantum Spin Hall Insulator State in HgTe Quantum Wells. *Science*, 318(5851):766–770, nov 2007. ISSN 0036-8075.

J. M. Kosterlitz and D. J. Thouless. Long range order and metastability in two dimensional solids and superfluids. (Application of dislocation theory). *Journal of Physics C: Solid State Physics*, 5(11), 1972. ISSN 00223719.

J. M. Kosterlitz and D. J. Thouless. Ordering, metastability and phase transitions in two-dimensional systems. *Journal of Physics C: Solid State Physics*, 6(7): 1181–1203, 1973. ISSN 00223719.

N. Kumar, S. N. Guin, C. Felser, and C. Shekhar. Planar Hall effect in the Weyl semimetal GdPtBi. *Physical Review B*, 98(4):1–4, 2018. ISSN 24699969.

S. K. Kushwaha, J. W. Krizan, B. E. Feldman, A. Gyenis, M. T. Randeria, J. Xiong, S. Y. Xu, N. Alidoust, I. Belopolski, T. Liang, M. Zahid Hasan, N. P. Ong, A. Yazdani, and R. J. Cava. Bulk crystal growth and electronic characterization of the 3D Dirac semimetal Na3Bi. *APL Materials*, 3(4), 2015. ISSN 2166532X.

V. Labracherie. *PhD: Electrical transport in nanostructures of the Weyl semimetal WTe 2*. PhD thesis, 2021.

L. D. Landau and V. L. Ginzburg. On the theory of superconductivity. *Zh. Eksp. Teor. Fiz.*, 20:1064, 1950.

A. I. Larkin and Y. N. Ovchinnikov. Nonuniform state of superconductors. *Zh. Eksp. Teor. Fiz.*, 47:1136–1146, 1964.

H. Li, J. Wu, X. Huang, G. Lu, J. Yang, X. Lu, Q. Xiong, and H. Zhang. Rapid and reliable thickness identification of two-dimensional nanosheets using optical microscopy. *ACS Nano*, 7(11):10344–10353, 2013. ISSN 19360851.

P. Li, C. Zhang, Y. Wen, L. Cheng, G. Nichols, D. G. Cory, G.-X. Miao, and X.-X. Zhang. Anisotropic planar Hall effect in the type-II topological Weyl semimetal WTe2. *Physical Review B*, 100(20):205128, nov 2019. ISSN 2469-9950.

P. Lindqvist, A. Nordström, and Ö. Rapp. New resistance anomaly in the superconducting fluctuation region of disordered Cu-Zr alloys with dilute magnetic impurities. *Physical Review Letters*, 64(24):2941–2944, 1990. ISSN 00319007.

Y. Liu, C. Zeng, J. Zhong, J. Ding, Z. M. Wang, and Z. Liu. Spintronics in Two-Dimensional Materials. *Nano-Micro Letters*, 12(1), 2020. ISSN 21505551.

Z. K. Liu, L. X. Yang, Y. Sun, T. Zhang, H. Peng, H. F. Yang, C. Chen, Y. Zhang, Y. F. Guo, D. Prabhakaran, M. Schmidt, Z. Hussain, S. K. Mo, C. Felser, B. Yan, and Y. L. Chen. Evolution of the Fermi surface of Weyl semimetals in the transition metal pnictide family. *Nature Materials*, 15(1):27–31, 2016. ISSN 14764660.

F. London and H. London. The electromagnetic equations of the supraconductor. *Proceedings of the Royal Society of London. Series A - Mathematical and Physical Sciences*, 149(866):71–88, mar 1935. ISSN 0080-4630.

B. Q. Lv, H. M. Weng, B. B. Fu, X. P. Wang, H. Miao, J. Ma, P. Richard, X. C. Huang, L. X. Zhao, G. F. Chen, Z. Fang, X. Dai, T. Qian, and H. Ding. Experimental discovery of weyl semimetal TaAs. *Physical Review X*, 5(3):1–8, 2015. ISSN 21603308.

I. Maccari, L. Benfatto, and C. Castellani. Broadening of the Berezinskii-Kosterlitz-Thouless transition by correlated disorder. *Physical Review B*, 96 (6):1–5, 2017. ISSN 24699969.

E. Majorana and L. Maiani. A symmetric theory of electrons and positrons. In *Ettore Majorana Scientific Papers*, pages 201–233. Springer Berlin Heidelberg, Berlin, Heidelberg, 1937. ISBN 3540480919.

S. Matsuura, P. Y. Chang, A. P. Schnyder, and S. Ryu. Protected boundary states in gapless topological phases. *New Journal of Physics*, 15, 2013. ISSN 13672630.

T. S. Menon, S. Mishra, V. C. Antony, K. Dixit, S. Kakkar, T. Ahmed, S. Islam, A. Jayaraman, K. Hsieh, P. Karnatak, and A. Ghosh. Optimising graphene visibility in van der Waals heterostructures. *Nanotechnology*, 30(39):395704, sep 2019. ISSN 0957-4484.

N. D. Mermin and H. Wagner. Absence of ferromagnetism or antiferromagnetism in one- or two-dimensional isotropic Heisenberg models. *Physical Review Letters*, 17(22):1133–1136, 1966. ISSN 00319007.

M. Mondal, S. Kumar, M. Chand, A. Kamlapure, G. Saraswat, G. Seibold, L. Benfatto, and P. Raychaudhuri. Role of the vortex-core energy on the Berezinskii-Kosterlitz-Thouless transition in thin films of NbN. *Physical Review Letters*, 107(21):1–5, 2011. ISSN 00319007.

S. Murakami. Phase transition between the quantum spin Hall and insulator phases in 3D: Emergence of a topological gapless phase. *New Journal of Physics*, 9, 2007. ISSN 13672630.

Y. Naidyuk, O. Kvitnitskaya, D. Bashlakov, S. Aswartham, I. Morozov, I. Chernyavskii, G. Fuchs, S. L. Drechsler, R. Hühne, K. Nielsch, B. Büchner, and D. Efremov. Surface superconductivity in the Weyl semimetal MoTe2 detected by point contact spectroscopy. *2D Materials*, 5(4), 2018. ISSN 20531583.

S. Nandy, G. Sharma, A. Taraphder, and S. Tewari. Chiral Anomaly as the Origin of the Planar Hall Effect in Weyl Semimetals. *Physical Review Letters*, 119(17): 1–6, 2017. ISSN 10797114.

A. M. Nazmul, H. T. Lin, S. N. Tran, S. Ohya, and M. Tanaka. Planar Hall effect and uniaxial in-plane magnetic anisotropy in Mn δ -doped GaAs p-AlGaAs heterostructures. *Physical Review B - Condensed Matter and Materials Physics*, 77(15):1–8, 2008. ISSN 10980121.

H. B. Nielsen and M. Ninomiya. The Adler-Bell-Jackiw anomaly and Weyl fermions in a crystal. *Physics Letters B*, 130(6):389–396, 1983. ISSN 03702693.

A. Nordström and Ö. Rapp. Resistance-peak anomaly in metallic glasses: Dependence on currents and contact arrangement. *Physical Review B*, 45(21): 12577–12579, jun 1992. ISSN 0163-1829.

K. S. Novoselov, A. K. Geim, S. V. Morozov, D. Jiang, M. I. Katsnelson, I. V. Grigorieva, S. V. Dubonos, and A. A. Firsov. Two-dimensional gas of massless Dirac fermions in graphene. *Nature*, 438(7065):197–200, 2005. ISSN 00280836.

K. Onnes. Further experiments with liquid helium. C. On the change of electric resistance of pure metals at very low temperatures etc. IV. The resistance of pure mercury at helium temperatures. *Leiden Comm.*, 120b, 122b:1479–1481, 1911.

A. Pippard. An experimental and theoretical study of the relation between magnetic field and current in a superconductor. *Proceedings of the Royal Society of London. Series A. Mathematical and Physical Sciences*, 216(1127):547–568, feb 1953. ISSN 0080-4630.

A. B. Pippard. *Magnetoresistance in metals*, volume 2. Cambridge university press, 1989. ISBN 0521326605.

A. C. Potter, I. Kimchi, and A. Vishwanath. Quantum oscillations from surface Fermi arcs in Weyl and Dirac semimetals. *Nature Communications*, 5(May), 2014. ISSN 20411723.

X.-L. Qi and S.-C. Zhang. Topological insulators and superconductors. *Reviews of Modern Physics*, 83(4):1057–1110, oct 2011. ISSN 0034-6861.

N. Reyren, S. Thiel, A. D. Caviglia, L. Fitting Kourkoutis, G. Hammerl, C. Richter, C. W. Schneider, T. Kopp, A. S. Rüetschi, D. Jaccard, M. Gabay, D. A. Muller, J. M. Triscone, and J. Mannhart. Superconducting interfaces between insulating oxides. *Science*, 317(5842):1196–1199, 2007. ISSN 00368075.

M. Sato. Non-Abelian statistics of axion strings. *Physics Letters, Section B: Nuclear, Elementary Particle and High-Energy Physics*, 575(1-2):126–130, 2003. ISSN 03702693.

M. Sato and Y. Ando. Topological superconductors: A review. *Reports on Progress in Physics*, 80(7), 2017. ISSN 00344885.

C. Shekhar, A. K. Nayak, Y. Sun, M. Schmidt, M. Nicklas, I. Leermakers, U. Zeitler, Y. Skourski, J. Wosnitza, Z. Liu, Y. Chen, W. Schnelle, H. Borrmann, Y. Grin, C. Felser, and B. Yan. Extremely large magnetoresistance and ultrahigh mobility in the topological Weyl semimetal candidate NbP. *Nature Physics*, 11(8):645–649, 2015. ISSN 17452481.

G. Shipunov, I. Kovalchuk, B. R. Piening, V. Labracherie, A. Veyrat, D. Wolf, A. Lubk, S. Subakti, R. Giraud, J. Dufouleur, S. Shokri, F. Caglieris, C. Hess, D. V. Efremov, B. Büchner, and S. Aswartham. Polymorphic PtBi2: Growth, structure, and superconducting properties. *Physical Review Materials*, 4(12): 124202, 2020. ISSN 24759953.

D. Shoenberg. *Magnetic Oscillations in Metals*. Cambridge Monographs on Physics. Cambridge University Press, 1984. ISBN 9780521224802.

R. Singha, S. Roy, A. Pariari, B. Satpati, and P. Mandal. Planar Hall effect in the type-II Dirac semimetal VAl3. *Physical Review B*, 98(8):081103, aug 2018. ISSN 2469-9950.

D. T. Son and B. Z. Spivak. Chiral anomaly and classical negative magnetoresistance of Weyl metals. *Physical Review B - Condensed Matter and Materials Physics*, 88(10):1–4, 2013. ISSN 10980121.

F. Tang, P. Wang, P. Wang, Y. Gan, G. D. Gu, W. Zhang, M. He, and L. Zhang. Quasi-2D superconductivity in FeTe 0.55 Se 0.45 ultrathin film. *Journal of Physics: Condensed Matter*, 31(26):265702, jul 2019. ISSN 0953-8984.

S. Thirupathaiah, Y. Kushnirenko, K. Koepernik, B. R. Piening, B. Büchner, S. Aswartham, J. van den Brink, S. Borisenko, and I. C. Fulga. Sixfold fermion near the Fermi level in cubic PtBi2. *SciPost Physics*, 10(1):1–14, 2021. ISSN 25424653.

D. J. Thouless, M. Kohmoto, M. P. Nightingale, and M. den Nijs. Quantized Hall Conductance in a Two-Dimensional Periodic Potential. *Physical Review Letters*, 49(6):405–408, aug 1982. ISSN 0031-9007.

M. Tinkham. Effect of Fluxoid Quantization on Transitions of Superconducting Films. *Physical Review*, 129(6):2413–2422, mar 1963. ISSN 0031-899X.

M. Tinkham. *Introduction to Superconductivity*. Dover Publications, 2 edition, jun 2004. ISBN 0486435032.

R. Vaglio, C. Attanasio, L. Maritato, and A. Ruosi. Explanation of the resistance-peak anomaly in nonhomogeneous superconductors. *Physical Review B*, 47(22): 15302–15303, jun 1993. ISSN 0163-1829.

A. Veyrat, V. Labracherie, R. Acharya, D. L. Bashlakov, F. Caglieris, J. I. Facio, G. Shipunov, L. Graf, J. Schoop, Y. Naidyuk, R. Giraud, J. van den Brink, B. Büchner, C. Hess, S. Aswartham, and J. Dufouleur. Bereziskii-Kosterlitz-Thouless transition in the Weyl system PtBi2. *arXiv:2101.01620*, jan 2021.

X. Wan, A. M. Turner, A. Vishwanath, and S. Y. Savrasov. Topological semimetal and Fermi-arc surface states in the electronic structure of pyrochlore iridates. *Physical Review B - Condensed Matter and Materials Physics*, 83(20):1–9, 2011. ISSN 10980121.

D. Wang, L. Kong, P. Fan, H. Chen, S. Zhu, W. Liu, L. Cao, Y. Sun, S. Du, J. Schneeloch, R. Zhong, G. Gu, L. Fu, H. Ding, and H. J. Gao. Evidence for Majorana bound states in an iron-based superconductor. *Science*, 362(6412): 333–335, 2018. ISSN 10959203.

J. Wang, X. Chen, Y. Zhou, C. An, Y. Zhou, C. Gu, M. Tian, and Z. Yang. Pressure-induced superconductivity in trigonal layered PtBi2 with triply degenerate point fermions. *Physical Review B*, 103(1):1–6, 2021. ISSN 24699969.

B. Wu, V. Barrena, H. Suderow, and I. Guillamón. Huge linear magnetoresistance due to open orbits in PtBi2. *Physical Review Research*, 2(2):022042, may 2020. ISSN 2643-1564.

Y. Wu, N. H. Jo, L. L. Wang, C. A. Schmidt, K. M. Neilson, B. Schrunk, P. Swatek, A. Eaton, S. L. Bud'ko, P. C. Canfield, and A. Kaminski. Fragility of Fermi arcs in Dirac semimetals. *Physical Review B*, 99(16):2–7, 2019. ISSN 24699969.

L. Xing, R. Chapai, R. Nepal, and R. Jin. Topological behavior and Zeeman splitting in trigonal PtBi2-x single crystals. *npj Quantum Materials*, 5(1), 2020. ISSN 23974648.

S. Y. Xu, I. Belopolski, N. Alidoust, M. Neupane, G. Bian, C. Zhang, R. Sankar, G. Chang, Z. Yuan, C. C. Lee, S. M. Huang, H. Zheng, J. Ma, D. S. Sanchez, B. K. Wang, A. Bansil, F. Chou, P. P. Shibayev, H. Lin, S. Jia, and M. Z. Hasan.

Discovery of a Weyl fermion semimetal and topological Fermi arcs. *Science*, 349 (6248):613–617, 2015. ISSN 10959203.

J. Zeng, E. Liu, Y. Fu, Z. Chen, C. Pan, C. Wang, M. Wang, Y. Wang, K. Xu, S. Cai, X. Yan, Y. Wang, X. Liu, P. Wang, S.-J. Liang, Y. Cui, H. Y. Hwang, H. Yuan, and F. Miao. Gate-Induced Interfacial Superconductivity in 1T-SnSe 2. *Nano Letters*, 18(2):1410–1415, feb 2018. ISSN 1530-6984.

L. Zhao, L. Xu, H. Zuo, X. Wu, G. Gao, and Z. Zhu. Fermi surface and carrier compensation of pyrite-type PtBi2 revealed by quantum oscillations. *Physical Review B*, 98(8):1–6, 2018. ISSN 24699969.

J. Ziman. *Electrons and Phonons: The Theory of Transport Phenomena in Solids.* Oxford University Press, feb 2001. ISBN 9780198507796.

K. Zimmermann. *Quantum point contact in high mobility graphene.* Theses, Université Grenoble Alpes, jun 2017. URL https://tel.archives-ouvertes.fr/tel-01369319.

Selbstständigkeitserklärung

Hiermit versichere ich, dass ich die vorliegende Arbeit ohne unzulässige Hilfe Dritter und ohne Benutzung anderer als der angegebenen Hilfsmittel angefertigt habe. Die aus fremden Quellen direkt oder indirekt übernommenen Gedanken sind als solche kenntlich gemacht. Die Arbeit wurde bisher weder im Inland noch im Ausland in gleicher oder ähnlicher Form einer anderen Prüfungsbehörde vorgelegt.

Diese Arbeit wurde unter Betreuung von Prof. Büchner am Institut für Festkörperforschung (IFF) des Institutes für Festkörper- und Werkstoffforschung Dresden e.V. (IFW Dresden) angefertigt. Es haben keine früheren erfolglosen Promotionsverfahren stattgefunden.

Ich erkenne hiermit die Promotionsordnung der Fakultät Mathematik und Naturwissenschaften der Technischen Universität Dresden vom 23.02.2011 an.

Dresden, den 10.März 2022

Arthur Veyrat